From the Institute of Biochemistry
University of Lübeck
Director: Prof. Dr. Dr. h.c. Rolf Hilgenfeld

# Crystallographic Investigations of the Stringent Factor from Eubacteria

Dissertation in Fulfillment of the Requirements
for the Doctoral Degree of the University of Lübeck
from the Department of Natural Sciences

Submitted by

Raspudin Saleem Batcha
from Devakottai, India

Lübeck, 2014

**Intelligence is the ability to adapt to change.**

*- Stephen Hawking*

# Chapter 1. Introduction

**1.1 Prelude**

Economic management of growth and division in response to environmental conditions is important for all cellular organisms. To surveil and adapt to their environment, they depend on sensory systems to govern complex physiological pathways. Bacteria sense stress; in response they adapt to manage their growth by unstochastically switching their metabolic pathways to limited gene expression using versatile strategies.

*"It is not the strongest of the species that survives, nor the most intelligent that survives. It is the one that is the most adaptable to change."*

*- Charles Robert Darwin* (according to "Origin of species", 1872)

**1.2 Review of literature**

**1.2.1 Stringent control and the discovery of the magic spots**

In bacteria, the exponential phase of growth is a pattern of balanced growth wherein all the cells are dividing and growing by geometric progression. An imbalance in the growth causes perturbation and one such perturbation that has been widely studied is an imbalance in tRNA-charging during protein synthesis. Cashel and Gallant [1969] dissected a regulatory mechanism of stringent control in *E. coli* that apparently serves to coordinate protein synthetic activity with that of a variety of other cellular metabolic activities. This stringent control is a large sum of adjustments that bacterial cells make when confronted by such an imbalance. The regulatory role of this mechanism is mediated by the secondary messengers guanosine 5'-diphosphate, 3'-diphosphate (ppGpp) and the analogous pyrophosphorylated derivative of GTP (pppGpp). Cashel and Gallant first identified ppGpp and pppGpp by performing two-dimensional thin-layer chromatography of radiolabeled nucleotides from aminoacid-starved *Escherichia coli* cells and correlated their appearance with the cessation of rRNA synthesis [Cashel and Gallant, 1969]. These compounds were named magic spots, MS I (ppGpp) and MS II (pppGpp) before their chemical identities were studied.

### 1.2.2 Bacterial stringent response to the environmental stimuli

The stringent response is an adaptive mechanism of bacteria to survive under constricted environmental stress conditions. In other words, it is a pleiotropic physiological process comprising changes in metabolism and gene expression tailing the decline of aminoacyl-tRNA pools to maintain the requirements of protein biosynthesis. Due to its role in growth and control of gene expression, the bacterial stringent control and the response mechanism are still remaining a subject of active interest since the late 1960s. The initiation of the stringent response is mediated by the synthesis of the magic spots, (p)ppGpp. These molecules of the stringent response control several events in the life cycle of a bacterium depending upon the environment in which the bacteria grow, including sporulation, biofilm-formation, symbiosis and virulence [reviewed in Chatterji and Ojha, 2001; Magnusson et al., 2005; Jain et al., 2006b; Potrykus and Cashel, 2008; Dalebroux et al., 2010]. In general, the stringent response modulates the physiology of the bacteria to a level that allows survival during the different environmental stages in their lifecycle.

The stringent response in bacteria is mainly triggered by amino-acid deprivation or carbon, nitrogen or phosphate limitation. The characteristic rate and rhythm of accumulating (p)ppGpp, which is commonly referred to as an "alarmone" molecule evokes the response mechanism, in which a conditional decrease in ribosome synthesis, results in a general hindrance of protein synthesis and growth arrest. The eminent and conserved consequence of the emergence of these nucleotides is the repression of ribosomal RNA synthesis [Wolz et al., 2010]. In addition, ppGpp binds directly to the bacterial RNA polymerase and alters transcriptional activity [Artsimovitch et al., 2004], clampdowns genes associated with the translational apparatus [Srivatsan and Wang, 2008]; simultaneously upregulating genes encoding metabolic enzymes involved in amino-acid biosynthesis [Paul et al., 2005], proteolysis [Voellmy and Goldberg, 1980] and coding for the σ factors [Jishage et al., 2002] (Figure 1.2.1).
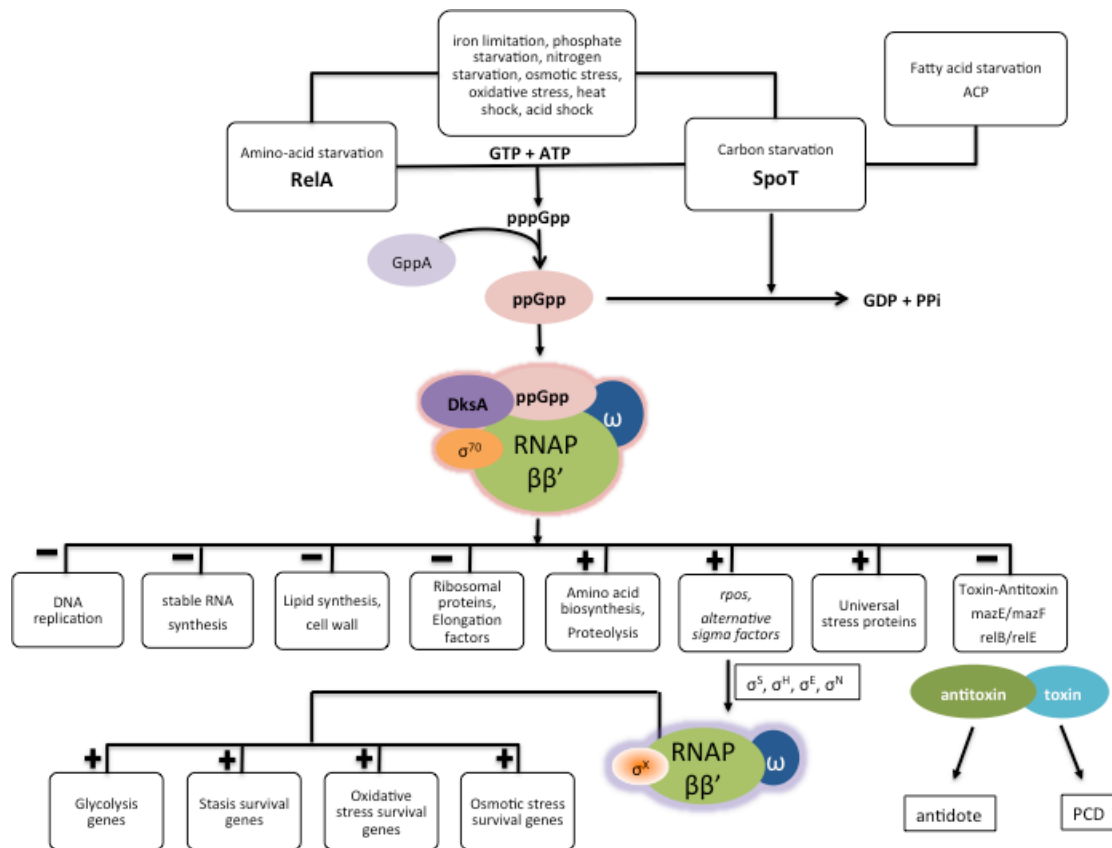
**Figure 1.2.1**: A schematic illustration of stringent response metabolism: pppGpp is synthesized from GTP and ATP by two pathways in response to starvation and stress and is hydrolyzed to ppGpp. ppGpp binds to RNAP and alters the transcription pathway from growth-related genes to genes involved in resistance and survival.

### 1.2.3 Bacterial stringent factors and their organization

In bacteria, the levels of (p)ppGpp are mainly controlled by two classes of enzymes:

- Monofunctional (p)ppGpp synthetase-only enzymes and
- Bifunctional (p)ppGpp synthetase/(p)ppGpp hydrolase enzymes.

Monofunctional (p)ppGpp hydrolase-only enymes have so far not been reported in bacteria, but have been identified in metazoa (Mesh1) [Sun et al., 2010; Atkinson et al., 2011]. RSH stands for **R**elA/**S**poT **H**omolog. In addition to synthesis, the bifunctional enzyme catalyzes the hydrolysis of ppGpp to GDP and PP$_i$, and of pppGpp to GTP and PP$_i$. The Gram-negative gammaproteobacteria such as *E. coli*, *Legionella, Pseudomonas* and *Salmonella* encode both RelA and SpoT [Dalebroux et al., 2010]. Under conditions other than amino-acid starvation, a basal level of ppGpp accumulates and SpoT enzyme responds to stress and nutrient limitations [Gong et al.,

2002]. In absence of SpoT, Gram-negative bacteria cannot degrade RelA-derived ppGpp, as the accumulation of the nucleotide disrupts cell-cycle control. The *E. coli* RelA protein has only the ppGpp-synthetase activity [Gentry and Cashel, 1996]. Critical amino-acid residues in the hydrolase active site histidine and aspartate are exchanged by phenylalanine and proline, respectively; which suggests that the hydrolase domain is inactive but still retains its native structure in *E. coli* RelA [Aravind and Koonin, 1998]. Enzymes of few pathogenic Gram-positive bacteria such as *Mycobacterium*, alphaproteobacterial *Brucella spp.*, and epsilonproteobacteria were annotated as Rel, RSH, and SpoT, respectively. They encode ppGpp-synthetase and -hydrolase pathways as a distinct single bifunctional enzyme, differing from the two-enzyme archetype [Dalebroux et al., 2010; Mittenhuber, 2001]. Several Gram-positive bacetria such as *Bacillus*, *Listeria*, *Streptococcus* and *Enterococcus* encode not only a single bifunctional RSH protein but also other small RelA-like synthetases (RelP/RelQ) [Lemos et al., 2008]. Similar small RelA-like synthetases (RelV) have been identified in *Vibrio cholera* [Das et al., 2009] (Figure 1.2.2). A comprehensive sequence and phylogenetic analysis classifies RSHs into 30 RSH subgroups "across the tree of life". These include previously unknown RSHs in archaea, fungi, eukaryotes, and dictyostelid amoebae in addition to new bacterial RSHs with unusual domain structures [Atkinson et al., 2011].
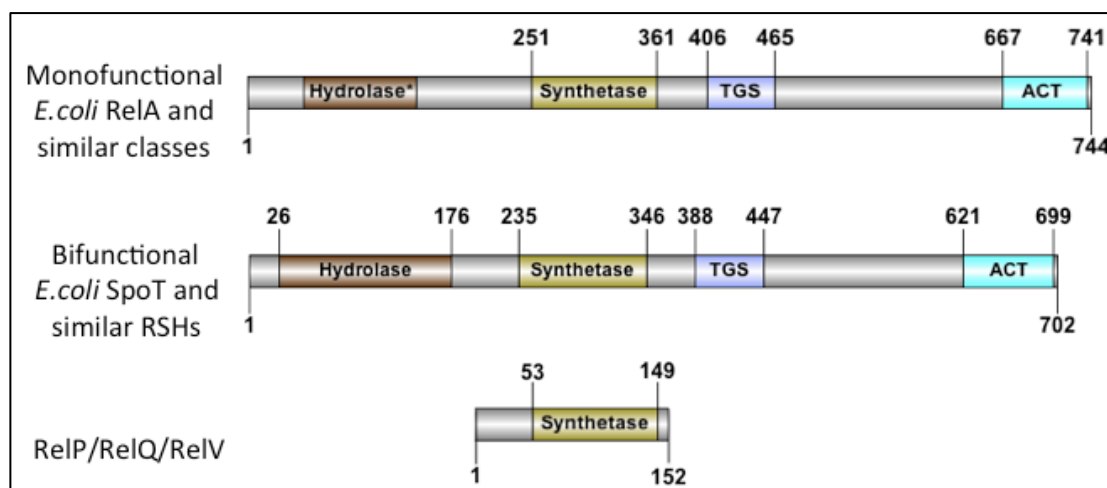


**Figure 1.2.2**: Domain organization of the enzymes that control the bacterial affluence of ppGpp in *E. coli* and other bacteria (residues numbered in accordance to Pfam annotation). * represents inactivity of corresponding domain due to exchange of the amino-acid residues. The length of the protein (RSH) varies between different bacteria.

4

### 1.2.3.1 Organization of the N-terminal catalytic domains

In bifunctional RelA/SpoT enzymes, the hydrolase (HD) and the synthetase domains are the two catalytic domains located in the N-terminal half of the Rel class of proteins (Figure 1.2.3) [Hogg et al., 2004; Avarbock et al., 2005]. A typical example for a characterized catalytic N-terminal fragment is *Streptococcus dysgalactiae subsp. equisimilis* Rel 1-385 (Rel$_{Seq}$385) [Mechold et al., 2002; Hogg et al., 2004]. The HD domain is a metal-dependent phosphohydrolase domain (Pfam accession number: PF01966) [Aravind and Koonin, 1998]. The metal-dependent phosphohydrolase domain comprises a highly conserved doublet of the catalytic residues histidine (H) and aspartate (D) known as HD motif. The HD motif defines a superfamily of metal-dependent phosphohydrolases that includes a diversity of uncharacterized proteins and domains associated with nucleotidyltransferases and helicases from bacteria, archaea, and eukaryotes [Aravind & Koonin, 1998; Yakunin et al., 2004]. This domain is involved in the hydrolysis of (p)ppGpp and the reaction requires the presence of $Mn^{2+}$. Structural interpretations revealed that the hydrolase domain is prevalently α-helical, comprising a 4-helix bundle, an extended loop, and a β-hairpin [Hogg et al., 2004]. The synthetase domain (Pfam accession number: PF04607) is involved in the synthesis of (p)ppGpp. It comprises a 5-stranded mixed β-sheet surrounded by five α-helices in a sandwich-like fashion. A central 3-helix bundle (C3HB) connects synthetase and hydrolase domains. The synthesis activity requires the presence of $Mg^{2+}$.
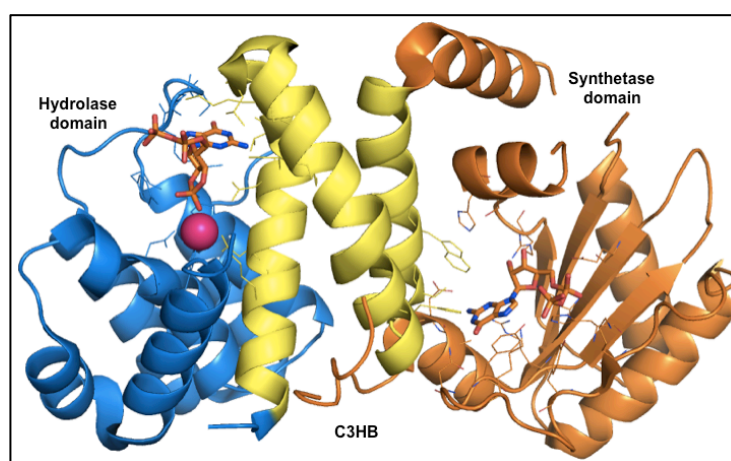


**Figure 1.2.3**: Crystal structure of the N-terminal catalytic domain of Rel protein (hydrolase-ON/synthetase-OFF conformer) from *Streptococcus dysgalactiae subsp.*

**1.2.3.2 Organization of the C-terminal regulatory domains**

TGS and ACT are two conserved regulatory domains present in the C-terminal region of Rel proteins. TGS is a small domain that consists of ~50 amino-acid residues and is predicted to possess a predominantly β-sheet structure (Pfam accession number: PF02824). The TGS domain occurs in two types of regulatory proteins, the GTPases and guanosine polyphosphate phosphohydrolases/synthetases. This domain is named after its identification in a number of enzymes such as **T**hrRS (Threonyl-tRNA synthetase), **G**TPase (Obg-family GTPases), and **S**poT [Sankaranarayanan et al., 1999; Wolf et al., 1999; Aravind and Koonin, 1998]. Its presence in the above-mentioned regulatory proteins suggests a nucleotide-binding property. A study in *E.coli* suggests that the TGS domain of SpoT interacts with the acyl carrier protein (ACP). The holo-ACP acts as a cofactor in lipid metabolism by carrying intermediates through successive enzymatic reactions of the fatty acid biosynthesis elongation cycle. [Battesti and Bouveret, 2006].

ACT domains (Pfam accession number: PF01842) are linked to a wide range of metabolic enzymes that are regulated by amino-acid concentration. They have a conserved regulatory binding fold with approximately 70 – 80 amino-acid residues. The archetypical ACT domain is often a C-terminal regulatory domain that exhibits a ferredoxin-like βαββαβ topology [Chipman and Shaanan, 2001]. Pairs of ACT domains bind specifically to a particular amino acid leading to regulation of the linked enzyme that functions in the control of metabolism, solute transport, and signal transduction [Aravind and Koonin, 1998; Schuller et al., 1995; Chipman and Shaanan, 2001; Liberles et al., 2005; Grant, 2006]. Aravind and Koonin coined the name 'ACT domain', after three of the allosterically regulated enzymes in which this domain was initially found: **A**spartate kinase, **C**horismate mutase, and **T**yrA (Prephenate dehydrogenase) [Aravind and Koonin, 1998]. Upon fusing with other proteins, ACT domains make them prone to regulation by small molecules [Grant, 2006]. TGS and

ACT domains in RelA and RSHs are linked by a varying stretch of approximately 150-200 amino-acid residues including conserved cysteine residues.

## 1.2.4 SpoT-dependent (p)ppGpp regulation in Gram-negative bacteria

Apart from amino-acid starvation, (p)ppGpp can be induced by other stress conditions such as deprivation of phosphorus, iron limitation, carbon-source or fatty-acids limitation. Under these conditions, SpoT regulates the accumulation of the (p)ppGpp [Spira et al., 1995; Battesti and Bouvret, 2006; Vinella et al., 2005]. The interaction acyl carrier protein (ACP) with SpoT in *E. coli* is required for the accumulation of (p)ppGpp in response to fatty-acid starvation by adjusting the balance between the synthetic and hydrolytic activities of SpoT. The studies also suggest the interesting possibility that this pathway might also transmit the cell's carbon levels to SpoT [Battesti and Bouvret, 2006; 2009]. In fact, carbon deprivation would affect glycolysis thereby leading to fatty-acid starvation. The flexibility of the structure of ACP enables it to bind multiple partners within the territory of fatty acid biosynthesis [Srivatsan and Wang, 2008]. Another study provided evidence for SpoT physically interacting with the ribosome-associated GTPase CgtA and regulating the (p)ppGpp degradation activity on the ribosome. The study also suggests that the absence of CgtA is necessary for (p)ppGpp accumulation under nutrient deprivations [Jiang et al., 2007]. The conserved G protein, CgtA, acts as a repressor of the stringent response by regulating SpoT activity to maintain low ppGpp levels in nutrient-rich environment [Raskin et al., 2007]. Observations such as interaction of G-proteins [Jiang et al., 2007; Raskin et al., 2007] and of ACP with SpoT [Battesti et al., 2006] suggest the interesting postulation that SpoT is a "vigil" that monitors the physiological state of *E. coli* cells and adjusts the levels of (p)ppGpp independent of RelA.

## 1.2.5 Metabolic cycle of (p)ppGpp.

The first (p)ppGpp synthetase to be discovered was the ribosome associated RelA protein from *E. coli*, where the gene that encodes *rel*A was identified in the RC gene locus [Cashel and Gallant, 1969]. Amino-acid starvation causes the binding of uncharged tRNAs to the ribosomal A-site and stalls protein synthesis. As an effect, RelA is able to recognize such stalled ribosomes and to bind to them, resulting in the synthesis of (p)ppGpp using ATP [Cashel et al., 1996]. Despite the low abundance of

RelA, millimolar concentrations of (p)ppGpp are produced rapidly, i.e. approximately 1 molecule per 200 ribosomes. Since the (p)ppGpp synthesis causes dissociation of RelA from the ribosome, RelA shuttles to another stalled ribosome and repeats the reaction [Wendrich et al., 2002]. The RelA enzyme, which is also called ATP:GTP 3'-diphosphotransferase, catalyzes the transfer of the β,γ-pyrophosphate of ATP to the 3' position of GTP in presence of magnesium. Kinetic studies revealed that RelA could both catalyze the conversion of GTP to pppGpp, and of GDP to ppGpp [Justesen et al., 1986]. The first and foremost product of the stringent response to amino-acid starvation is pppGpp that is rapidly converted to the more stable compound ppGpp by pppGpp 5'-phosphohydrolase (GPP) [Keasling et al., 1993; Kristensen et al., 2002; Dennis et al., 2004]. Accumulation of ppGpp is known to affect the level of exopolyphosphatase (PPX) activity in many bacteria [Kristensen et al., 2002]. In *E. coli*, ppGpp inhibits the degradation of polyphosphates by GPP and its homolog PPX [Kristensen et al., 2004]. The elevated level of polyphosphates in *E. coli* associates with the Lon protease to control degradation of free ribosomal protein and increases RecA and RpoS levels in turn activating the SOS response and increasing the general stress resistance of bacteria [Kuroda et al., 1997; Kristensen et al., 2008]. The crystal structure of GppA from *Aquifex aeolicus* in complex with ppGpp revealed the structural basis for its phosphatase activity in greater detail. In the active site, the observed ample space between the side-chain of Gln119 and the 5′-β-phosphate of the bound ppGpp suggest that the pppGpp substrate undergoes hydrolytic attack by Gln119 either directly or possibly through activating a catalytic water molecule [Kristensen et al., 2008].

Earlier studies provided evidence that the product of the *spoT* gene is a $Mn^{2+}$ -dependent (p)ppGpp 5'- pyrophosphohydrolase later a weak synthetase activity was observed [Weyer et al., 1976; Kari et al., 1977; Hernandez and Bremer, 1991]. The GDP resulting from the ppGpp hydrolysis reaction can be converted to GTP by nucleoside 5'-diphosphatekinase (Ndk) [Ginther and Ingraham, 1974]. GDP and GTP serve equally well as substrates for RelA *in vitro*. pppGpp, and not ppGpp, is the initial product of the stringent response *in vivo*, because the physiological level of GDP is significantly lower than that of GTP [Pedersen and Kjeldgaard, 1977; Justesen et al., 1986]. A generalized metabolic cycle of ppGpp is presented in Figure 1.2.4**.**
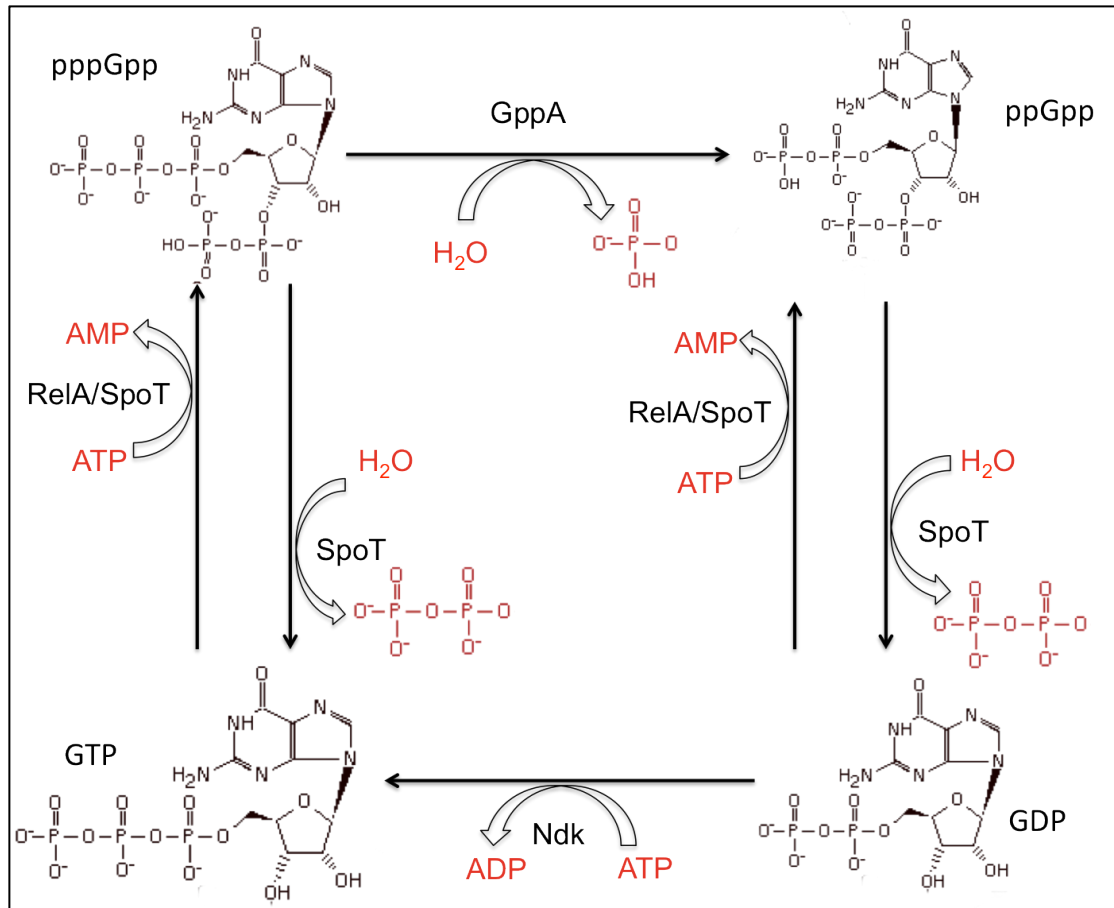
**Figure 1.2.4:** Generalized biosynthetic pathway of ppGpp.

### 1.2.6 An overview of pyrophosphate transfer reactions

Among the biochemical pathways, two different modes are known by which pyrophosphate is transferred from ATP.

One mode of transfer occurs in PRPP (5-phosphoribosyl-1-pyrophosphate) synthesis, an intermediary reaction in the *de-novo* synthesis of purine nucleotides. In the synthesis of PRPP from ribose-5-phosphate and ATP, PRPP synthetase catalyzes the pyrophosphate transfer from ATP to ribose 5-phosphate to form the 5-phosphoribosyl-1-pyrophosphate in a single step [Khorana et al., 1958] (Figure 1.2.5).
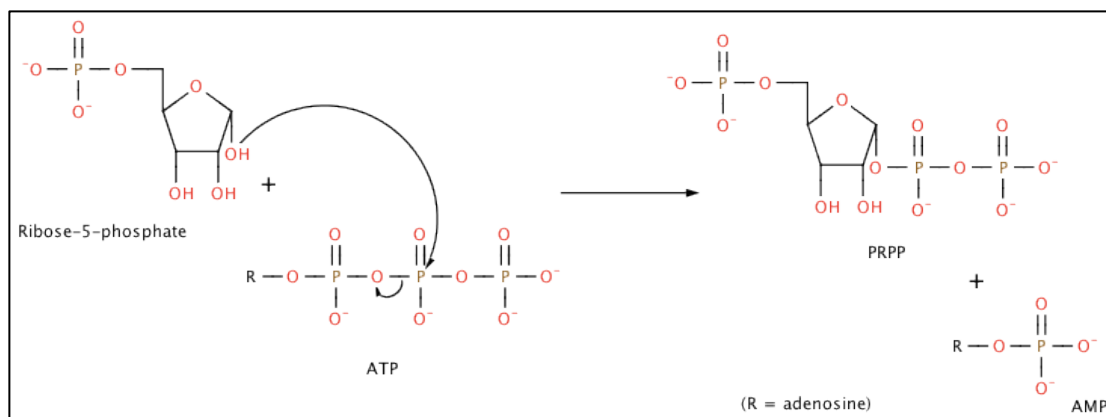
**Figure 1.2.5:** Ribose-5-phosphate conversion to PRPP. The Pβ-Pγ group of ATP is transferred with the Pβ ending up attached to C1 on the ribose.

Another mode of pyrophosphate ester generation occurs in the synthesis of mevalonyl pyrophosphate, an intermediary in steroid biosynthesis. In this case, phosphate transfer occurs in two steps, first yielding a mevalonyl-5-monophosphate (Figure 1.2.6 A) through transfer of γ-phosphate from an ATP molecule. In the second step, mevalonyl-5-monophosphate is phosphorylated by transfer of the γ-phosphate of another molecule of ATP (Figure 1.2.6 A).
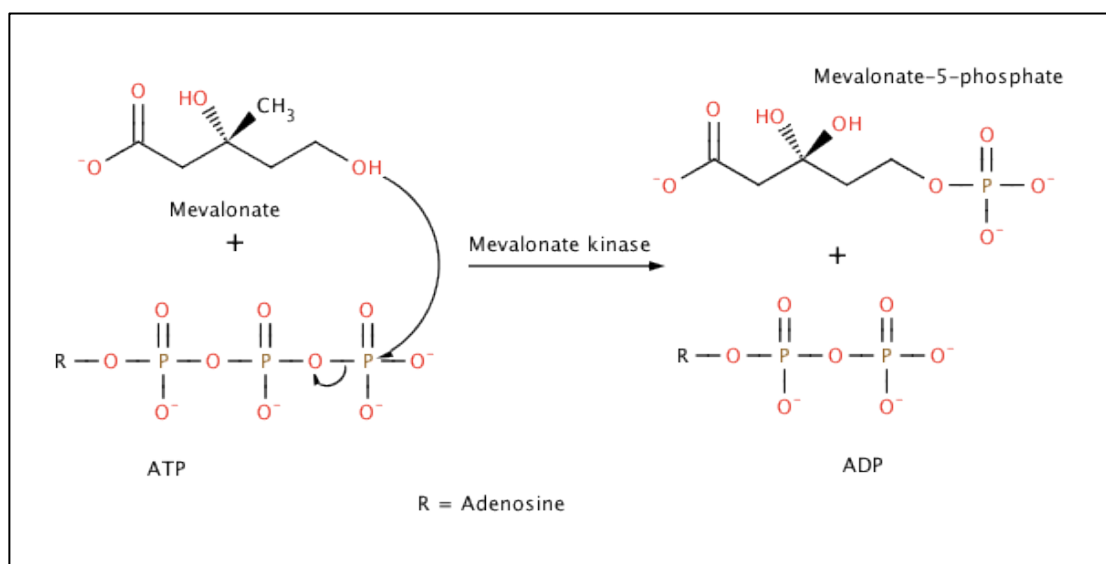


**Figure 1.2.6 A:** Step 1: Conversion of mevalonate to mevalonate-5-phosphate

10
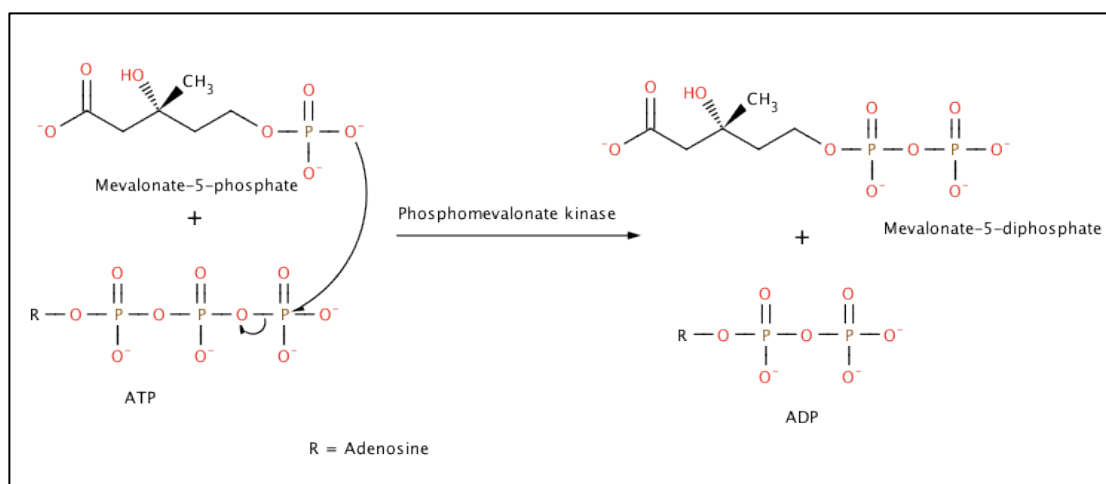
**Figure 1.2.6 B:** Step 2: Conversion of mevalonate-5-phosphate to mevalonate-5-diphosphate.

### 1.2.7 The crystal structure and the reaction mechanisms of Rel

The crystal structure of the catalytic N-terminal fragment of *Streptococcus dysgalactiae subsp. equisimilis* Rel 1-385, in short $Rel_{Seq}385$ [Hogg et al., 2004] revealed two monomers, each locked in a different state (hydrolase-ON/synthetase-OFF and hydrolase-OFF/synthetase-ON). The two catalytic sites are separated by more than 30 Å in each monomer. Based on the structural and mutagenesis data, modeling of the catalytic activities exposed a conformational change induced by ligand binding, which regulates the antagonistic active sites. As a result, futile recycling between (p)ppGpp synthesis and hydrolysis is avoided by a complex regulatory mechanism that involves subtle conformational changes in the protein [Hogg et al., 2004] (Figure 1.2.7).

### 1.2.7.1 (p)ppGpp synthesis

The crystal structure also suggested a (p)ppGpp synthetase mechanism for the attack of the 3'-OH group of GDP (or GTP) onto the β-phosphorus atom of ATP. Most likely, Glu323 of $Rel_{Seq}385$ activates the hydroxyl group by proton abstraction. Support for a critical role of Glu323 in the synthetase mechanism derives from a follow-up mutational study in which a $Rel_{Seq}385$ mutant bearing a Glu323Gln substitution exhibited severely defective synthetase activity [Hogg et al., 2004]. In the synthetase-ON state, the carboxylate group of Asp264, which is presumed to coordinate $Mg^{2+}$ upon ATP binding, is located within the (p)ppGpp-synthetase active

11

site forming an "IN" conformation by pointing towards Glu323. In the synthetase-OFF state, the (p)ppGpp-synthetase active site configuration is radically altered as Asp264 is removed from the synthetase pocket forming an "OUT" conformation, indicating an inactive state for $Mg^{2+}$-ATP binding for synthetase reaction [Hogg et al., 2004]. It has been suggested that a charge reversal in a conserved motif in the synthetase domain differentiates (p)ppGpp synthesis by monofunctional (E*X*DD motif) and bifunctional (R*X*KD motif) Rel proteins. Higher $Mg^{2+}$ concentration inhibit (p)ppGpp synthesis in bifunctional Rel but not in monofunctional Rel. Further, the study proposed that in R*X*KD-containing bifunctional proteins, a loop-to-helix transition of the α13-β4 loop induced by $Mg^{2+}$ closes the substrate binding pocket, thereby preventing (p)ppGpp synthesis. In contrast, E*X*DD-containing proteins are not affected by (p)ppGpp synthesis as $Mg^{2+}$ is unable to induce a similar structural change [Sajish et al., 2007].

**1.2.7.2 Substrate specificities of the Rel$_{Seq}$385 synthetase**

Mechold et al. [2002] showed that the specific acceptor of the Rel$_{Seq}$385-catalyzed synthesis reaction is, according to preference, GTP>IDP>GDP. The nucleotide tested were [γ-$^{32}$P] ATP as pyrophosphate donor and GTP, GDP, GMP, dGDP, ITP, IDP, and XTP as acceptors. In contrast, RelA$_{Ec}$ prefers acceptors in the order GTP=GDP> ITP. Using [α-$^{32}$P] GTP as donor and several nucleotide candidates as accceptors, the specificities for pyrophosphate donors were limited to ATP and dATP [Heinemeyer and Richter, 1978; Mechold et al., 2002].

**1.2.7.3 (p)ppGpp hydrolysis**

The hydrolase domain is predominantly α-helical, forming a 4-helix bundle, an extended loop and a β-hairpin. A detailed comparative analysis of Rel$_{Seq}$385 hydrolase domain with the catalytic domain of human PDE4 revealed that both HD superfamily members share a common fold for cleaving the nucleotide 3'-phosphoester bonds of their substrates (p)ppGpp and cNMP, respectively [Xu et al., 2000; Hogg et al., 2004]. The crystal structure of Rel$_{Seq}$385 displayed a nucleotide intermediate, guanosine 5'-diphosphate-2':3'-cyclic monophosphate (ppG2':3'p) in the hydrolysis site of one monomer. The 2':3'-cyclic phosphate projects into the hydrolase pocket containing the essential hexacoordinated $Mn^{2+}$ cofactor in a distorted octahedral mode. Modeling of the ligand suggests a mechanism for ppGpp

12

hydrolysis. In the conformational rearrangement from the ppG2':3'p-bound monomer (hydrolysis-ON) to the ligand-free monomer (hydrolysis-OFF) (Figure 1.2.7), Arg44 releases its inter-domain contacts with Asn148 and Thr151 of the central 3-helix bundle (C3HB) and forms an intra-domain salt-bridge with Asp78. As a result of the salt-bridge formation, the newly formed ion pair removes the carboxylate group of Asp78 from the $Mn^{2+}$-coordination, thereby altering the ligation to a pentacoordinated state. This cascade of events was named a "clutch-and-release" mechanism, triggered by ligand binding. At elevated levels of (p)ppGpp, a clutching motion between the hydrolase domain and the C3HB occurs to entrap the nucleotide within the hydrolase active site. Upon ligand release, the salt-bridge between Asp78 and Arg44 disrupts, and Asp78 joins the coordination sphere of the $Mn^{2+}$ ion, thus activating the hydrolysis reaction [Hogg et al., 2004].
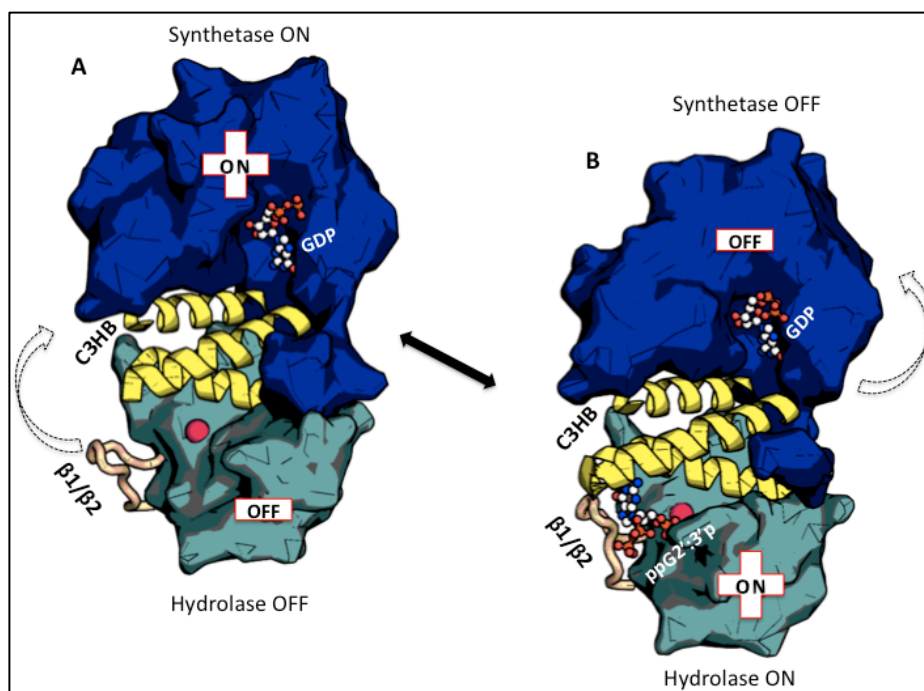


**Figure 1.2.7**: Conformational states of $Rel_{Seq}385$: Surface/cartoon representations of $Rel_{Seq}385$ in the hydrolase-OFF/synthetase-ON (**A**) and hydrolase-ON/synthetase-OFF (**B**) conformations. Domain coloring: hydrolase - green; C3HB – yellow helices; synthetase – blue. The curved arrows depict domain movements upon ligand binding to the hydrolase site. Translational and rotational components of the C3HB domain and synthetase domain movements are represented as curved arrows.

**1.2.7.4 Functional aspects of the C-terminal regulatory domains of the stringent factor**

The C-terminal domain is involved in RelA-RelA interactions in *E.coli* and specific residues participating in the interaction were narrowed down to C638, C612, and D637 [Gropp et al., 2001]. The results from genetic experiments (CyaA complementation) using bacterial two-hybrid system experiments suggests that RelA homooligomerization through its C-terminal domain is involved in the activation of (p)ppGpp synthesis [Gropp et al., 2001]. Another study in *E.coli* suggested that two regions, amino-acid residues 455 to 538 and 550 to 682, are involved in dimerization [Yang and Ishiguro, 2001a]. A study in *Mycobacteria smegmatis* also showed that the bifunctional Rel$_{Msm}$ protein oligomerizes *in vitro*, but that the monomer is active in pppGpp synthesis [Jain et al., 2006a]. A follow-up multiple cysteine mutagenesis study revealed that the mutations rendered the protein monomeric and the bifunctional property of the enzyme changed as a function of the mutation of cysteines [Jain et al., 2007]. More specifically, it was suggested that Rel$_{Msm}$ C692S makes the synthesis activity of the full-length protein nonresponsive to tRNA. Further, the study proposed that upon uncharged tRNA binding to Rel protein, a conformational change abolishes the interaction between C692 and active-site [Jain et al., 2007]. Earlier studies with *Mycobacterium tuberculosis* Rel$_{Mtb}$ showed that the synthetic activity in the presence of uncharged tRNA increases further upon the addition of ribosome and poly(U) RNA to the system [Avarbock et al., 2000]. Regulation of (p)ppGpp degradation could involve an interaction between the extreme C-terminus and the hydrolase domain in the N-terminal half [Mechold et al., 2002]. In addition, there is also evidence for RelA that addition of several amino-acid residues to the C-terminus of RelA by suppression of an amber codon inactivates (p)ppGpp synthetase activity [Breeden and Yarus, 1982]. Based on the observations of oligomerization studies, the monomer could be the species able to bind to ribosomes and undergo to conformational change to activate (p)ppGpp synthesis. If so, then the dimer or higher-order oligomer species could possibly be involved in the (p)ppGpp-degradation activity. It is interesting to study the exact parameters controlling the efficiency of the C-terminal domain of Rel proteins.

In an intriguing structural study on the *Bacillus subtilis* Obg GTPase, ppGpp (copurified from bacterial lysates) was trapped within the active-site P-loop

suggesting that bacterial Obg proteins may interact with this molecule *in vivo*. No direct interactions were observed between the ppGpp 3'-diphosphate and the C-terminal TGS domain of Obg/CgtA (Figure 1.2.8). Conservation of the C-terminal TGS domain, in combination with structural and biochemical observations, suggests that the *B. subtilis* Obg protein may have evolved to recognize ppGpp or pppGpp in response to changes in the cellular environment [Buglino et al., 2002].
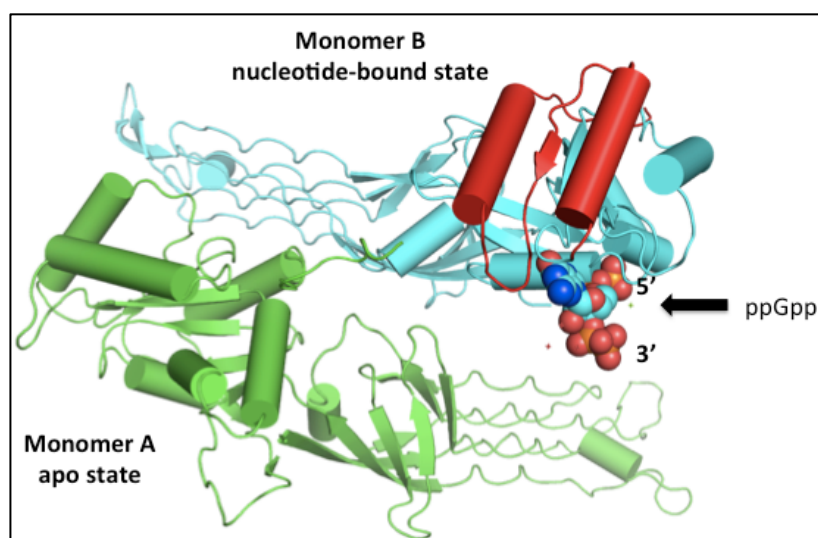


**Figure 1.2.8**: Crystal structure of the Obg GTPase from *Bacills subtilis* (PDB ID: 1LNZ; Buglino et al., 2002) showing two monomers in different states. Green – monomer A in ligand-free state, cyan/red – monomer B in ppGpp-bound state. ppGpp is represented as spheres. Red colour represents the C-terminal TGS domain.

The TGS domain of SpoT physically interacts with the central cofactor of fatty-acid biosynthesis, acyl-carrier protein (ACP). ACP is involved in sensing the starvation cues in lipid metabolism and triggering SpoT-dependent (p)ppGpp accumulation [Battesti and Bouveret, 2006]. Point mutations within the C-terminal TGS domain of SpoT disrupt the interaction with ACP and consequently favour the activity of ppGpp synthesis over hydrolysis [Battesti and Bouveret, 2009].

A study on arthrofactin regulation in *Pseudomonas sp.* MIS38 found that a C-terminal fragment of SpoT, including the ACT domain but not the TGS domain, is involved in the accumulation of ppGpp and abolishment of arthrofactin production. Arthrofactin is a cyclic lipopeptide, which acts as biosurfactant. It is synthesized by multimodular nonribosomal peptide synthetases (NRPS). An impairment in the arthrofactin production results in biofilm formation. This study indicates that a forced expression

of the C-terminal region of *spoT* that contains the ACT domain under the *relA*[+] background resulted in the accumulation of (p)ppGpp, which further influences the biofilm formation i.e. an adaptive survival phase among bacteria [Washio et al., 2011].

**1.2.8 ppGpp, DksA, and the RNA polymerase**

The ppGpp binds to the β and the β' subunits of RNA polymerase, altering the transcription mechanics and in turn mediating the stringent response. The crystal structure of the *Thermus thermophilus* RNA polymerase (RNAP) holoenzyme in complex with ppGpp unveils the binding mode of ppGpp near the active center of RNAP [Artsimovitch et al., 2004]. The response of RNA polymerase to ppGpp requires an important nontemplate-DNA binding protein, DksA. Based on the crystal structure, Artsimovitch and colleagues proposed a few modes of transcription regulation by ppGpp using the RNAP:ppGpp complex together with a modeled non-template DNA (NT-DNA). In one of the modes, a modeled RNAP:ppGpp:NT-DNA complex suggests that the base pairing of guanosine from ppGpp with cytosines of the modeled NT-DNA results in reduction of the open complex blocking transcription (Figure 1.2.9). The models further explained the differences in the level of inhibition from the two rRNA promoters, *rrnB* and *rrnD* [Artsimovitch et al., 2004].



**Base pairing of Cytosine with Guanosine of ppGpp**
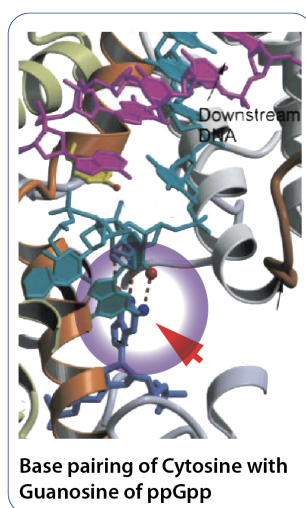
**Figure 1.2.9:** Enlarged view of the open complex in the vicinity of the active and ppGpp-binding sites. ppGpp (blue) in the 3'-orientation forms a putative base pair (red dashes, pointed and encircled in bubble) with the NT cytosine (cyan) (adapted from Artsimovitch et al., 2004).

Evidence from *in-vitro* mutagenesis and biochemical studies in *E.coli* RNA polymerase did not support rRNA transcription regulation by the crystallographically defined binding site for ppGpp in *T. thermophilus* RNA polymerase [Vrentas et al., 2008]. Results suggest that the ppGpp-binding pocket identified in the crystal is not responsible in the regulation of *E. coli*-based rRNA transcription initiation. Further, the study emphasizes the necessity of including the ω subunit in bacterial RNAP preparations. Also, *T. thermophilus* genome analysis showed that *dksA* homologs are not apparent in their genome sequences. Altogether, the results indicate that *E. coli* RNAP and *T. thermophilus* RNAP respond differently to ppGpp and are not appropriate for comparison with each other [Vrentas et al., 2008].

For balancing the translational capacity, ppGpp prompts downregulation of transcription from $\sigma^{70}$- promoters [Cashel et al., 1996]. Being a global transcriptional regulator, DksA directly interacts with RNA polymerase (RNAP) and, in cooperation with ppGpp, modulates transcription initiation at target promoters. Most of the characterized DksA proteins hold a canonical $Cys_4$ Zn-finger motif proposed as necessary for proper folding and function. Extensive characterizations have shown that DksA along with the ω subunit of RNAP plays a major role *in vivo* [Chatterji et al., 2007] and *in vitro* [Vrentas et al., 2005; Mathew and Chatterji, 2006] for eliciting the stringent response. A study using the DksA:ppGpp:RNAP complex model suggested that DksA mediates the effect of ppGpp in transcription inhibition [Perederina et al., 2004]. An *in-vitro* experiment demonstrated that DksA amplifies the ppGpp-mediated inhibition of rRNA promoters besides activating transcription from the promoters involved in amino-acid biosynthesis [Paul et al., 2004; 2005]. Recently, a transcriptional regulation study identified a Zn-independent secondary DksA (DksA2) [Blaby-Haas et al., 2011]. DksA2, a paralog in *Pseudomonas aeruginosa* lacks the canonical Zn finger motif. The result suggests that DksA2 plays a role in Zn homeostasis by serving as a copy of the canonical Zn-dependent DksA in Zn-poor environments. This study also manifests that DksA2 destabilizes the open promoter complex at *rrnB* P1 promoters, thus inhibiting transcription in the presence of ppGpp [Blaby-Haas et al., 2011].

**1.2.9 A brief overview on the 70S ribosome in prokaryotes.**

Ribosomes are the molecular machines that harmonize the interaction of tRNAs, mRNA, and proteins that leads to biosynthesis of proteins. After the primordial work by Ada Yonath, unlimited progress on the structure of the ribosome has been made by X-ray crystallographic methods. In prokaryotes, the ribosomal assembly has a mass of ~2500 kDa and a sedimentation coefficient of 70S (S for Svedberg unit). The major constituents of a 70S ribosome can be disassembled into a large subunit (50S) and a small subunit (30S). These subunits can be further dissociated into their constituent proteins and RNAs. The complete 70S ribosome complex [Selmer et al., 2006] as well as the individual structures of the 30S [Schluenzen et al., 2000] and the 50S [Hansen et al., 2003] subunits have been determined close to atomic resolution (Figure 1.2.10).

The 50S subunit contains 34 different proteins (L1 to L34) and two RNA molecules, a 23S rRNA and a 5S rRNA species. The 30S subunit contains 21 different proteins (S1 to S21) and a 16S rRNA molecule. The prokaryotic ribosome consists of one copy of 16S, 23S and 5S rRNA, two copies each of L7 and L12 proteins, and one copy each of all other subunit proteins. The stringent response is initiated by the binding of stringent factor RelA to stalled ribosomes that have an uncharged tRNA species in the ribosomal A-site [Haseltine & Block, 1973; Wendrich et al., 2002]. The 50S subunit protein L11 is involved in the stringent response since ribosomes lacking L11 are defective in (p)ppGpp synthesis. However, RelA can interact with L11-depleted 70S ribosomes stoichiometrically in the presence of ATP and GTP. [Friesen et al., 1974; Wendrich et al., 2002]. L11 is a part of the ribosomal GTPase-associated region (GAR). The GAR is involved in the GTPase activity of initiation, elongation, and termination factors during protein synthesis. The C-terminal domain of L11 interacts with nucleotides 1051–1108 in domain II of 23S rRNA (also called the L11-binding domain, L11BD) [Schmidt et al., 1981; Thompson et al., 1993]. The N-terminal domain of L11 has a highly conserved and proline-rich helix. A single-site mutation at proline 22 in the N-terminal domain of L11 reduced the ribosome-dependent RelA activity. However, upon wild-type L11 reconstitution, the activity was restored [Yang & Ishiguro, 2001b; Jenvert & Schiavone, 2007].

18
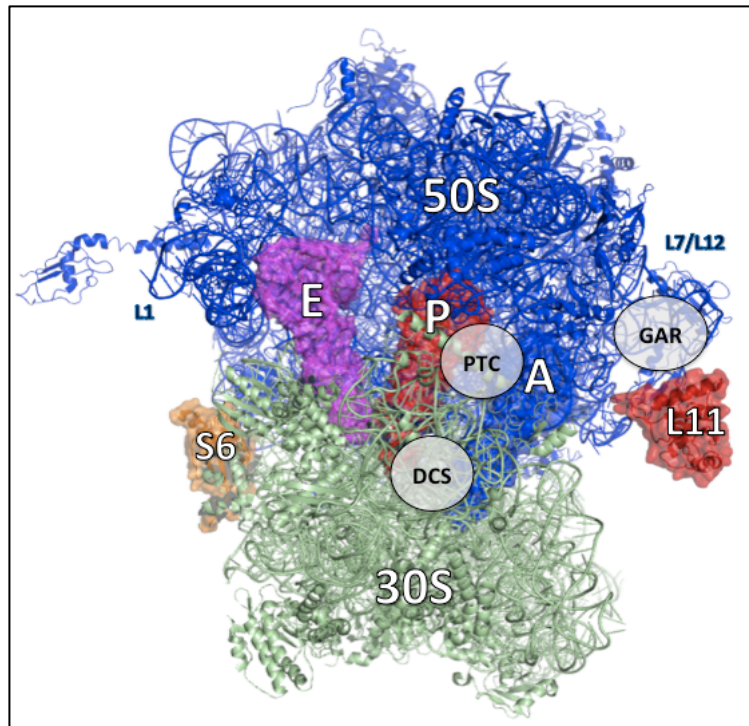
**Figure 1.2.10:** Crystal structure of the 70S ribosome in complex with tRNA from *Thermus thermophilus* HB8 at 2.8Å resolution (PDB IDs: 2J00 and 2J01; Selmer et al., 2006), showing the locations of the 30S, the 50S, A-, P-, and E-site tRNAs, the L1 stalk, the L7/L12 stalk, the L11, the S6, the peptidyl transfer centre (encircled PTC), the decoding site (encircled DCS), and the factor binding site (encircled GAR).

### 1.2.10 (p)ppGpp and translational factors

In bacteria, the translational regulation by (p)ppGpp comprises the repression of the transcription of the protein synthesis machinery such as rRNA, tRNA and ribosomal proteins, and interaction with the GTPases such as initiation factor (IF2) and elongation factors (EF-Tu and EF-G) [Cashel et al., 1996; Milon et al., 2006]. Addition of ppGpp to IF2 completely abolishes the binding of initiator fMet-tRNA$^{fMet}$ to the 30S preinitiation complex [Yoshida et al., 1972]. Earlier studies on the interaction of ppGpp with EF-Tu indicate that ppGpp binds to form a complex EF-Tu:ppGpp [Arai et al., 1972]. The study also showed that ppGpp inhibits the exchange of EF-Tu:GDP both in the presence and absence of EF-Ts. *In-vitro* studies on a starved translation system to understand the effect of (p)ppGpp on the translational accuracy showed that ppGpp decreases missense error by preferentially inhibiting EF-Tu [Wagner et al., 1982]. Extensive biochemical studies suggested that under certain kinetic conditions, the EF-Tu:ppGpp complex can increase the

"proofreading flow" over the ribosome by binding to a ribosome:mRNA:aatRNA complex and thereby increasing fidelity of protein synthesis [Pingoud et al., 1983; Rojas et al., 1984]. Another view suggested that ppGpp guards the cell against errors in translation originating from amino-acid starvation by forming EF-Tu:ppGpp and improving proofreading [Dix and Thompson, 1986]. A study on the interaction between ppGpp and IF2 demonstrated that ppGpp inhibits translation by selectively targeting IF2 activities. Data from this study also suggested that IF2 has the properties of a cellular metabolic sensor and regulator that switches between an active GTP-bound form and an inactive ppGpp-bound form [Milon et al., 2006]. A thermodynamic study demonstrated that apart from GDP and GTP, IF2 and EF-G interact with ppGpp leading to GTPase inhibition [Mitkevich et al., 2010].

## 1.2.11 (p)ppGpp and DNA replication

In order to maintain genome integrity, DNA replication is inhibited at the outset of starvation stresses. The DNA replication machinery is subject to stringent control in *Escherichia coli*, *Bacillus subtilis,* and other bacterial species [Levine et al., 1991; Wegrzyn, 1999; Wegrzyn and Wegrzyn, 2002]. (p)ppGpp wields an effect on DNA replication. Earlier studies have suggested that in *E.coli*, (p)ppGpp inhibits DNA replication by decreasing the transcription of *dnaA* that encodes the replication initiation protein [Zyskind and Smith, 1992]. SpoT regulates the affluence of (p)ppGpp and cues the carbon starvation relays to the primary cellular factors to direct DnaA proteolysis, thereby halting DNA replication [Lesley and Shapiro, 2008]. However, recent investigations demonstrate that in *E. coli* and *B. subtilis*, the DnaG primase-catalyzed reaction is inhibited by (p)ppGpp *in vitro* during the replication elongation step [Wang et al., 2007; Maciag et al., 2010]. Binding of (p)ppGpp to the primases at the replication forks disables the recruitment of RecA. As an effect, the replication machinery is suspended until favourable conditions are restored [Wang et al., 2007]. The effects of (p)ppGpp on the formation of primers by the DnaG–DnaB (helicase) complex and on DnaG have been described to be significantly stronger for ppGpp than for pppGpp [Maciag et al., 2010].

## 1.2.12 Programmed cell death: Toxin-antitoxin module and stringent factor

In *E.coli* and other bacteria including archaeae, chromosomal programmed cell death (PCD) systems have been reported [Aizenman et al., 1996; Engelberg-Kulka et al.,

2006; Wilson and Nierhaus, 2005] and are activated by stress conditions, such as nutrient stress and antibiotics. PCD is one of the instances where bacteria behave like multicellular organisms. One of the most studied forms of PCD in bacteria is resolved through specific genetic modules called ''addiction modules'' or "suicide modules" or "toxin–antitoxin (TA) systems" [reviewed in Gerdes et al., 2005; Engelberg-Kulka et al., 2006]. These modules are mostly found in extrachromosomal elements such as plasmid and prophages of bacteria. However, TA loci were also reported in the chromosomes of many bacteria. TA systems consist of a lethal toxin and a neutralizing antitoxin. The toxin is usually long-lived and stable, whereas the antitoxin is labile and forms a tight complex with the toxin. The cells are addicted to the labile product, as its *de-novo* synthesis is essential for cell survival. The TA complex binds to one or more operators in the TA promoter region and represses transcription of the TA operon [Overgaard et al., 2009]. *E. coli* has several pairs of such genes, including *mazEF*, *relBE*, *dinJ-yafQ* and so forth. The most extensively studied systems, MazEF and RelBE, are activated during amino-acid starvation [Christensen et al., 2001].

Earlier studies showed that the *mazE* and *mazF* genes, which are located downstream of the *relA* gene, are a part of the *E.coli rel* operon. MazE is a labile protein degraded by the ClpA•ClpP ATP-dependent serine protease complex; it protects the cells from the stable MazF. The cellular levels of ppGpp regulate the expression of MazEF. *In toto*, the MazEF system serves as a mechanism for altruistic cell death [Aizenmann et al., 1996]. Although for a single bacterium, PCD is non-prolific, it becomes productive through simultaneous action of a group of cells [Engelberg-Kulka et al., 2006]. As a consequence, in nutrient-depleted environment, the starved cells undergo lysis through the MazEF system, permitting the survival of the rest of the cell population. Crystal structure determination of *E.coli* MazEF revealed the binding mode between the two, MazE antidote and MazF toxin. The complex is a 2:4 heterohexamer (Figure 1.2.11 A), comprising three alternating homodimers ($MazF_2MazE_2MazF_2$) [Kamada et al., 2003]. The structure also suggested a universal mechanism for toxin-antitoxin complex formation common to evolutionarily related addiction modules. Being an mRNA interferase, MazF inhibits protein synthesis through its endoribonucleolytic effect on mRNAs [Muñoz-Gómez et al., 2004]. The MazF endoribonuclease preferentially cleaves single-stranded mRNAs at ACA

sequences [Zhang et al., 2003]. However, alternative views suggested that the TA systems are involved in checking cellular processes such as translation and replication, which are downregulated in a growth-arrested cell [Nyström, 1998; Gerdes, 2000]. This alternative view contemplates that rather than inducing PCD, chromosomal TA systems induce a state of reversible bacteriostasis. The chromosomal *relBE* locus in *E. coli* encodes the RelE toxin and the RelB antitoxin, which form a non-toxic complex [Gotfredsen and Gerdes, 1998]. RelE is a ribosome-dependent RNase that cleaves mRNA positioned at the ribosomal A-site *in vitro* [Pedersen et al., 2002] and *in vivo* [Christensen and Gerdes, 2003]. Cleavage occurs at ribosome-bound mRNAs at the second position of the stop codons and of few sense codons such as CAG or UCG [Pedersen et al., 2002]. Takagi and co-workers have identified the homologous RelBE TA system in the hyperthermophilic archaeon *Pyrococcus horikoshii*. Their crystal structure of the archaeon RelE-RelB complex reveals that the complex is dimeric (aRelB-aRelE)$_2$, (Figure 1.2.11. B). aRelE folds into an α/β structure, whereas the aRelB lacking a hydrophobic core extensively wraps around the molecular surface of aRelE [Takagi et al., 2005]. The structure of RelBE is distinct from that of MazEF. Also, the lack of obvious sequence similarities classifies RelBE and MazEF as separate protein families. Recently, the crystal structures of the ribosome-dependent endonuclease, RelE, and its complex with the ribosome in both pre- and postcleavage states were determined. The structure revealed that the cleavage of mRNA on the ribosome is carried out by RelE and not by the ribosome itself [Neubauer et al., 2009].
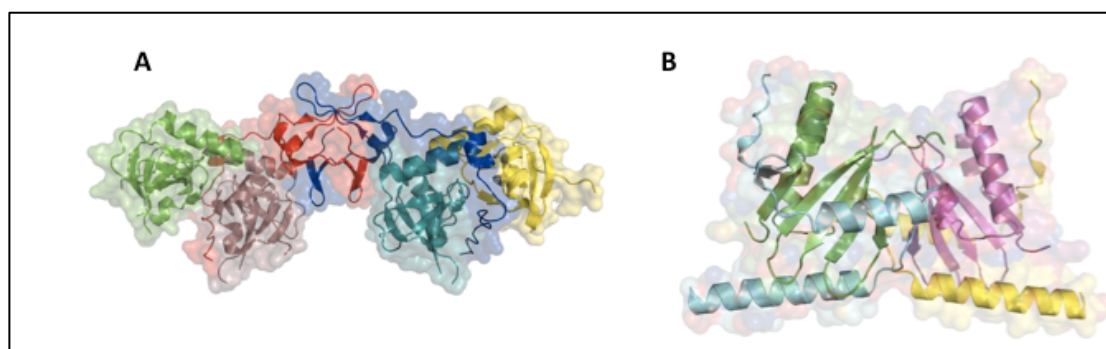


**Figure 1.2.11:** Crystal structures of toxin-antitoxin modules. (**A**) 2:4 heterohexamer of MazEF (PDB id: 1UB4; Kamada et al., 2003). (**B**) RelBE complex heterodimers (PDB id: 1WMI; Takagi et al., 2005).

In conclusion, the stalling of protein synthesis by RelA prevents the synthesis of nascent RelB, and existing RelB level inside the cells are diminished by the ATP-dependent Lon protease [Overgaard et al., 2009]. Consequently, toxin RelE binds to the stalled ribosomes and mediates cleavage of mRNA codons positioned at the ribosomal A-site. The RelE-mediated endonucleolytic cleavage of the mRNA codon at the A site acts a substrate for a tmRNA (tRNA–mRNA hybrid) based rescue system i.e. a system in which, tmRNA mitigates RelE toxicity by rescuing ribosomes stalled on damaged mRNAs [Christensen and Gerdes, 2003; Wilson and Nierhaus, 2005]. The tmRNA bind to the A site of ribosomes containing a truncated mRNA, and tag the congruent nascent polypeptide chains with a cue allowing normal termination of translation [Karzai et al., 2000]. Thus, the stringent pathway including the cooperation of RelBE and tmRNA increases degradation of nascent polypeptide chains on stalled ribosomes and permits the cell to improve the survival rate with resulting free amino acids [Wilson and Nierhaus, 2005].

**1.2.13 Impacts of the stringent factor on virulence regulation**

For bacteria, the availability of nutrients is a major factor that decides the developmental and the physiological traits for survival. The blueprint of the stringent response allows bacteria to coordinate enormous factors that act in concert. Many pathogenic bacteria rely on the stringent factor to direct complex pathogenic trait. Extensive studies in complex systems has unveiled that physiological adaptations to different growth conditions are subtly and indirectly linked to the resilience and virulence of bacterial pathogens.

(1) *Escherichia coli*

The virulent trait of Enterohemorrhagic *Escherichia coli* (EHEC) is the cell adherence, colonization and "attaching and effacing" lesions on intestinal epithelial cells [Nataro and Kaper, 1998] and the encoding pathogenicity island (PI) is the locus of enterocyte effacement (LEE). The nutrient-limited lower intestine stimulates an increase in surface colonization and minimal replication by bacteria. Upon nutrient deprivation, the elevated levels of ppGpp together with DksA activate LEE expression and increase bacterial adherence [Nakanishi et al., 2006]. Apart from horizontally acquired genetic elements such as the LEE and genes carried by cryptic prophages, EHEC is identical to the nonpathogenic laboratory strain *E. coli* K-12 [Mellies et al.,

2007]. Uropathogenic *Escherichia coli* (UPEC) causes acute urinary tract infection that leads to recurrent infections by the same bacterial strain defying antibiotic treatment. In order to persist in efforts to prolong inside the bladder epithelial cells, UPEC needs regulation of type-I adhesive fimbriae. UPEC depends on ppGpp and DksA to direct the *fim* operon for the regulation of fimbriae [Aberg et al., 2009]. Like the *E. coli* K-12 strain, UPEC and EHEC encode a monofunctional RelA enzyme and a bifunctional SpoT enzyme [Dalebroux et al., 2010].

(2) *Salmonella typhimurium*

Serovars of *Salmonella enterica* are highly pathogenic to humans and are known to cause infections such as typhoid fever and gastroenteritis, collectively called salmonellosis. *Salmonella enterica serovar typhimurium* (*S. typhimurium*) colonizes in the small intestine, where environmental signals activate the Type-III secretion system (T3SS). *S. typhimurium* RelA shows 96% sequence identity to *E. coli* K-12 and a bifunctional SpoT of 98% sequence identity to its counterpart in *E. coli* K-12. In *S. typhimurium*, *Salmonella* pathogenicity island 1 (SPI1) and *Salmonella* pathogenicity island 2 (SPI2) are two major virulence factors that are mediated through ppGpp. SPI1 and SPI2 expression involves a complex cascade of pathways with numerous transcriptional regulators located inside and outside the pathogenicity islands (PI) [Dieye et al., 2009]. On close encounters with intestinal epithelial M cells (M for microfold), SPI1 T3SS secretes effector molecules that cause cell ruffling and transcytosis. In the intestinal lumen, carbon and oxygen limitation cause ppGpp-dependent activation of a transcription regulator HilA. Together with the InvF transcriptional regulator and other factors, HilA coordinates SPI1 expression. Trespassing the epithelium, salmonellae are taken up by macrophages and trafficked to a combative, acidic phagosome called the *Salmonella*-containing vacuole. Inside the vacuole environment, SPI2 T3SS secretes the effectors that transform the vacuole into a cell-proliferating station. The vacuole compartment has elevated levels of cationic antimicrobial peptides, where salmonellae encounter an acidic and magnesium-limited environment. A two-component system, PhoP/PhoQ, gets activated in this environment where it represses SPI1 and activates SPI2. Upon repression of SPI1, the factors associated with bacterial uptake and increased antimicrobial resistance diminish, following an exchange of vacuole to a replicating compartment. PhoP enacts a feed-forward loop with SlyA, another transcriptional

regulator of SPI2. ppGpp promotes the SlyA activity whereas the environmental composition activates the PhoQ sensor kinase. Consequently, macrophage-guarded salmonellae enter the lymphatic system, where they get distributed into spleen and liver, causing typhoid fever [Haraga et al., 2008].

(3) *Streptococcus dysgalactiae subsp. equisimilis*

*Streptococcus dysgalactiae subsp. equisimilis* (*S. equisimilis*) is a Gram-positive, large colony-forming (Lancefeld groups C (GCS) and G (GGS) β-hemolytic streptococci) bacterium that infects humans through indirect pathways [McDonald et al., 2007; Rantala et al., 2010]. *S. equisimilis* is increasingly recognized as the etiological agent of exudative pharyngitis and pyoderma in many countries [Chowdhury et al., 1997]. M protein (encoded by *emm*) is a typical virulence determinant for the group A streptococci (GAS) by its potential to allow bacteria to defy phagocytosis [Fischetti, 1989]. Downstream of *emm*, there are multigene regulator-like regions bordered by *rel*. A genomic study showed that both types of multigene regulator-like regions in GCS and GGS are linked via *rel* [Geyer and Schmidt, 2000].

**1.2.14 Role of the stringent factor in persistence and long-term survival**

Bacterial persistence is the ability of bacteria to overcome host-immune defense mechanisms and to tolerate lethal concentrations of bactericidal antibiotics. Persister as in antibiotic-tolerant bacteria is different from antibiotic-resistant mutants, in which the tolerance is inheritable and reversible [Jayaraman, 2008a]. An appealing genetic study proposed that elevated levels of (p)ppGpp push the cells into the persistent state [Korch et al., 2003]. Another study has shown that persisters exist in cells before antibiotic stress is inflicted [Balaban et al., 2004]. Many pathogenic bacteria have reached an equilibrium state of defiance to co-evolve with their host, as exemplified by the persistent infections of *Mycobacterium spp., Helicobacter pylori, Brucella spp.,* and so forth. *Mycobacterium tuberculosis*, the etiological agent of tuberculosis (TB), resides within the nutrient-starved environment of caseous lung granulomas during latent infection in humans [Klinkenberg et al., 2010]. A salient feature of *M. tuberculosis* is its intensive host-immune response defense mechanism by entering dormancy until favorable conditions are reached. Lethal concentrations of antibacterial agent such as rifampicin cannot affect such dormant-state mycobacteria.

In order to establish dormancy and latent infection *M. tuberculosis* recruits its stringent factor, Rel$_{Mtb}$. In response to carbon limitation, *M. tuberculosis* and non-pathogenic *M. smegmatis* accumulates polyphosphate. In mycobacteria, ppGpp acts downstream to anionic polyphosphate and is involved in the activation of *rel*, conversely polyphosphates act downstream to ppGpp in *E. coli*. The transcriptional activation of *rel* in mycobacteria involves the MprA/MprB two-component system, polyphosphate, and the alternative sigma factor σE. Polyphosphate donates phosphates to MprA and MprB, in turn activates σE. And σE prompts a positive-feedback loop and activates *mprA mprB* locus, as a consequence *rel* gets activated [Dalebroux et al., 2010].

## 1.2.15 Role of the stringent factor in quorum sensing

Intra-species or inter-species communication between bacteria requires the production of certain small signaling molecules. A major level of gene regulation is involved in such cell-cell communication. Many signal molecules that have been identified in bacteria are involved in a form of regulation related to cell density or population known as quorum sensing (QS). In some aspects the communications are simply signals produced at different stages of growth such as indole signaling in stationary phase *E. coli* [Jayaraman and Wood, 2008b]. The QS signals are collectively known as auotinducers. The autoinducer-mediated communication proceeds in a concentration-dependent manner. Many of the *Pseudomonas* species produce autoinducer molecules such as N-acylhomoserine lactones (AHLs) that control important functions, mainly pathogenicity. The human pathogen *Pseudomonas aeruginosa* has two quorum-sensing systems, *las* (*lasR-lasI*) and rhl (*rhlR-rhlI*). LasR and RhlR are the two transcription regulators activated by AHLs such as 3-oxo-C$_{12}$-HSL (N-(3-oxododecanoyl)-L-homoserine lactone) and C$_4$-HSL (N-butanoyl-L-homoserine lactone), respectively. At high cell density, these AHLs reach a threshold concentration and activate their cognate regulator. It has been demonstrated that the over-expression of *relA* leads to the expression of *lasR* and *rhlR* and activates quorum sensing in *P. aeruginosa* [van Delden et al., 2001]. In an intriguing study on *P. aeruginosa*, deletion of the *lptA* encoding lysophosphatidic acid acyltransferase, which is involved in the phospholipid biosynthesis pathway, resulted in an premature production of autoinducers such as C$_4$-HSL and C$_6$-HSL (N-hexanoyl-L-homoserine lactone) and increased the level of (p)ppGpp in the cell [Baysse et al. 2005]. The

study suggests that changes in cellular envelope properties act as a trigger for the stringent response. In *Streptococcus mutans*, deletion of the *relA* gene led to the overexpression of the *luxS* gene, indicating a communion between quorum sensing and stringent response [Lemos et al. 2004].

**1.2.16 Role of the stringent factor in biofilm formation**

Biofilms are structurally and functionally complex biological systems, in which passive assemblages of cells are found associated with abiotic surfaces. These microbial communities known as biofilms are composed of bacteria that are entangled within an exopolysaccharide matrix. The spatial arrangement of bacteria in such polysaccharide matrices exists as ordered structures that enable carriage of nutrients and waste in and out of the biofilm. Biofilms are tolerant and highly resistant to bactericidal antimicrobials when compared to logarithmic-phase planktonic cells. Various studies suggest that slow growth [Adams and McLean, 1999] and starvation survival [Balzer and McLean, 2002] are important for biofilm growth in *E. coli*. Another study on the biofilm-forming pathogen *Streptococcus mutans* shows that the RelA-deficient strains had an impaired capacity to form biofilms [Lemos et al., 2004]. A follow-up study in *S. mutans* by the same group reported that basal levels of (p)ppGpp produced by RelP and RelQ also play a pivotal role in cellular homeostasis associated to biofilm formation, and that these effects are influenced to some extent through CodY, a global nutritional repressor protein [Lemos et al., 2008].

Adherence is a primary step in the development of a biofilm. Taylor and colleagues have demonstrated that the ability to mount a stringent response is important in the growth of *Listeria monocytogenes* after adhesion and its subsequent virulence in mice [Taylor et al., 2002]. In *E. coli*, upregulation of the polysaccharide adhesin poly-β-1,6-N-acetyl-glucosamine (poly-GlcNAc) [Branda et al., 2005] and two-component systems PgaA/PgaD [Itoh et al., 2008] are involved in biofilm induction. Boehm and colleagues identified that ppGpp and bis-(3'-5')-cyclic di-GMP [c-di-GMP] are the main components that regulate poly-GlcNAc. Treatment of *E. coli* K-12 *csrA*::*Tn*5 mutant strain (*E. coli* K-12 forms biofilms under laboratory conditions) with translation inhibitors causes a SpoT-mediated decrease in ppGpp levels, resulting in specific derepression of PgaA. However, high expression of PgaD and poly-GlcNAc synthesis needs the accumulation of c-di-GMP by diguanylate cyclase YdeH. This

study reveals an important synergism of ppGpp and c-di-GMP in biofilm induction. However, specific cellular receptors that bind these second messengers remain to be discovered. Further, this finding suggests that blocking the second-messenger signaling act as an effective measure to avoid biofilms proceeding to chronic infections [Boehm et al., 2009].

**1.2.17 Role of the stringent factor in sporulation**

The sporulation is a drastic adaptive phase in the life cycle of certain bacteria, in which bacterial cell differentiates and morphogenetically responds to confront diverse environments. *Bacillus, Myxococcus*, and *Streptomyces* species are the most studied sporulating bacterial pathogens. Earlier studies suggested that *Bacillus subtilis* sporulation is induced by the stringent response to partial amino-acid deprivation [Ochi et al., 1981] and is caused by the decrease in GTP or GDP [Ochi et al., 1982]. Various studies in *B. subtilis* have suggested that sporulation initiation is a consequence of the accumulated ppGpp in the stationary phase, derepressing the GTP pool and relieving the repression of *spo0A* by CodY [Ratnayake-Lecamwasam et al., 2001; Inaoka and Ochi, 2002]. Spo0A is a transcription factor involved in developmental pathways such as sporulation, cannibalism, biofilm formation and genetic competence [Mirouze et al., 2011]. In *Myxococus xanthus*, (p)ppGpp synthesized in response to amino-acid limitation is responsible for initiating development of the fruiting body and myxospores [Harris et al., 1998].

**1.2.18 Interrelationship between bacterial acid stress and the stringent response**

*Escherichia coli* induces a number of amino-acid decarboxylases in response to acidic pH; their action results in the increase of pH of the growth medium [Gale and Epps, 1942]. The *E. coli* inducible lysine decarboxylase, LdcI (also called CadA), and CadB, the inner-membrane lysine-cadaverine antiporter, interact and provide cells with protection against mild acidic conditions. The catalytic role of LdcI is the proton-dependent decarboxylation of L-lysine to synthesize the polyamine cadaverine and $CO_2$ [Sabo et al., 1974]. Kanjee and co-workers have reported novel interactions between ppGpp and LdcI, which unveil the unknown connection between acid stress and stringent response. Their crystal structure of LdcI revealed that the protein is an

oligomer of five dimers that associate to form a decamer. LdcI was found to co-purify and co-crystallize with the stringent response effector ppGpp, with 10 ppGpp molecules in the decamer (Figure 1.2.12. A & B). ppGpp strongly inhibits LdcI enzymatic activity both *in vitro* and *in vivo*. This inhibition is important for modulating the consumption of lysine in cells during acid stress under nutrient-limiting conditions [Kanjee et al., 2011].
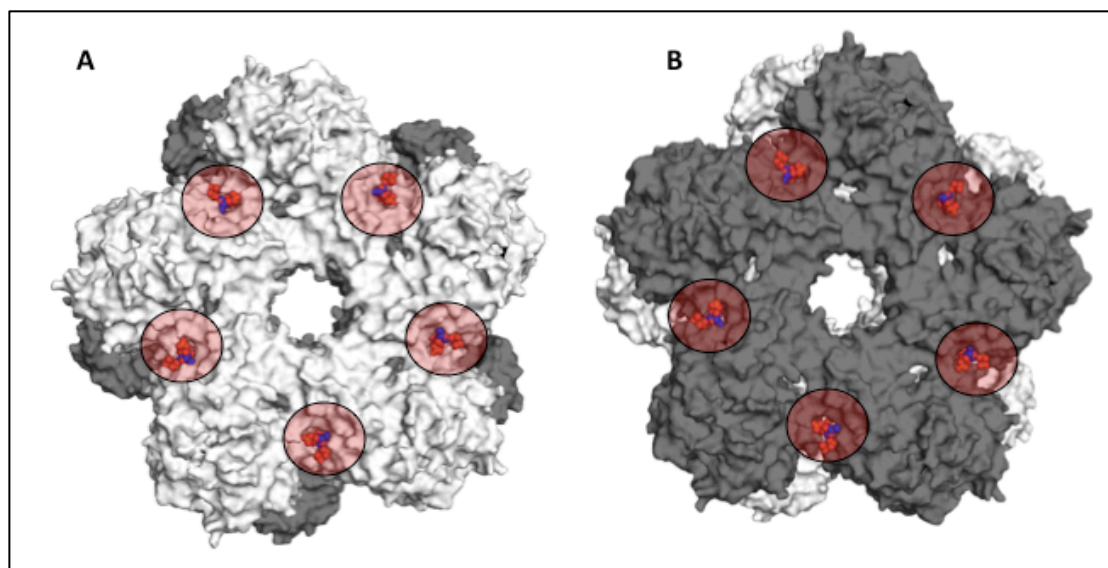


**Figure 1.2.12**: Surface representations of the crystal structure of the LdcI (PDB ID: 3N75; Kanjee et al., 2011) with 10 molecules of ppGpp (ppGpp in semi-transparent red circles). The assembly is an oligomer of five dimers that associate to form a decamer. (**A**) Front view of the LdcI decamer showing 5 ppGpp molecules. (**B**) Rear view of the LdcI decamer the showing remaining 5 ppGpp molecules.

# Chapter 2. Objectives of this study

Antibacterial drugs administered to treat various bacterial infections are primarily aimed to target processes such as protein synthesis, nucleic-acid synthesis, cell-wall synthesis, or folate synthesis [Walsh, 2003]. However, examination of the metabolic processes in bacteria revealed that targeting the stringent metabolic pathway has potential to lead to the development of a novel class of antibacterial agents [Wexselblatt et al., 2010; Wexselblatt et al. 2012]. Many pathogenic bacteria rely on stringent factors (Rel proteins) to control complex pathogenic trait. The stringent response mechanism in eubacteria has been investigated for decades through genetic and biochemical methods, with many unanswered questions remaining. The main objective of this thesis is to study the eubacterial stringent factors in order to understand and elaborate the essential mechanisms behind (p)ppGpp catalysis and regulation. Investigating stringent factors from various eubacteria, those that infect humans will accelerate the discovery and development of antibacterial drugs against the stringent response. With the help of the crystal structure of the N-terminal catalytic fragment of *Streptococcus dysgalatiae subsp. equisimilis* Rel [Hogg et al. 2004], a group of ppGpp analogs were synthesized and tested as candidate inhibitors [Wexselblatt et al., 2010]. Employing docking methods, a model for the interaction of one of the best ppGpp analogs was predicted [Wexselblatt et al., 2010]. Recently, a ppGpp analog, Relacin, has been established as a novel antibacterial agent targeting the stringent response [Wexselblatt et al. 2012].

In work presented here, an X-ray crystallographic approach was undertaken to determine the three-dimensional structures of the N-terminal catalytic fragment of *Streptococcus dysgalatiae subsp equisimilis* Rel ($Rel_{Seq}385$) in complex with GTP, ppGpp and their analogs. This study reports the complex structures of $Rel_{Seq}385$ that contribute to a molecular understanding of the essential mechanisms behind the biosynthesis of (p)ppGpp, the activity states of the Rel enzyme, and also serve as templates for the development of a novel class of antibiotics. The $Rel_{Seq}385$ can adopt two conformational stages, hydrolase-OFF/synthetase-ON and hydrolase-ON/synthetase-OFF. How do the substrates or the products influence the conformation of $Rel_{Seq}385$ is important for understanding (p)ppGpp catalysis, in this light a comparative structural analysis of the $Rel_{Seq}385$ complexes with an insight into

the regulating mechanism between its two catalytic domains [(p)ppGpp-synthetase and –hydrolase domains] is elucidated. Various substrate- and product-analogs were used as a means to probe and stabilize the induced states of $Rel_{Seq}385$. Additionally, it is intriguing to re-evaluate the identity of the metal ion involved in the chemical mechanism of (p)ppGpp hydrolysis in the hydrolase active site of $Rel_{Seq}385$.

In order to understand the regulatory role and structure of the C-terminal domain of Rel, various constructs expressing different fragments of Rel proteins (full-length domain and N-terminal region deleted versions) from several eubacteria such as *Escherichia coli* K-12, *Salmonella typhimurium*, *Thermus thermophilus* HB8 were revived or generated. Their construction and tentative characterizations towards crystallization are described in chapter 3. In this respect, an additional goal was the structural elucidation of the C-terminal domain of $RelA_{Ec}$ (*E. coli* RelA), although the efforts resulted in the determination of the structure of the ACT domain of $RelA_{Ec}$.

The results generated here in this thesis are aimed towards illuminating key aspects of the bacterial stringent response, which may facilitate the development of novel antibacterials.

# Chapter 3. Materials and Methods

**3.1 Materials**

**3.1.1 Equipments and devices**

| Materials | Manufacturer |
|---|---|
| - 80°C storage unit | REVCO – Kendro |
| - 20°C/ 4°C storage unit | LIEBHERR/Siemens |
| 4°C Cold-room cabin | eco – coils & coolers |
| 12°C Cold-room cabin | Viessmann |
| AF20 Ice-machine | Scotsman |
| Äkta Plus/Prime FPLC | Amersham Biosciences |
| Analytical Balance - BP 210 D | Sartorius |
| Avanti J-26xP centrifuge | Beckman Coulter |
| Concentrator 5301 | Eppendorf |
| Cryostream Cooler | Oxford Cryosystems |
| Excella E10 Platform Shaker | New Brunswick Scientific |
| French Pressure Cell | SLM Instruments |
| GeneAmp PCR System 9700 | PE Applied Biosystems |
| Hot air oven | Thermo Scientific |
| Ice-box | neoLab |
| Innova 4230 Refrigerated Incubator Shaker | New Brunswick Scientific |
| Laminar Flow Chamber | Heraeus/GELAIRE |
| Laser Spectroscatter 201 (Dynamic Light | RiNA |

| | |
|---|---|
| Scattering) | |
| MBA 2000 Spectrophotometer | Perkin Elmer |
| Membrane-Vacuum Pump | Vacuubrand |
| Mighty Small SE 245 Dual Gel Caster | Hoefer |
| Mighty Small II SE 250 Electrophoresis Chamber | Hoefer |
| Microscope SZX 12 | Olympus |
| Mini-Sub Cell For Agarose Gel Electrophoresis | Biorad |
| MR-2002 Magnetic Stirrer | Heidolph |
| Optima$^{TM}$ L-90K Ultracentrifuge | Beckman-Coulter |
| Petridishes | Greiner bio-one |
| pH 211 Microprocessor pH | HANNA Instruments |
| pH Meter/Titrator TR156 | Schott |
| Phoenix Crystallization Robot | Art-Robbins Instruments |
| Pipettes | Eppendorf |
| Power PAC 300 Voltage Adaptor | Biorad |
| Power Pack EPS 3501 XL | Amersham Biosciences |
| ProteomeLab PF2D$^{TM}$ (HPLC) | Beckman-Coulter |
| RC-5B Plus Centrifuge | DuPont Sorvall |
| Sonificator | Branson |
| Spectrophotometer - Cary 50 UV/Vis | Varian |
| Table-top Centrifuge | Heraeus Instruments |
| Thermal Cycler T-gradient | Biometra |

| | |
|---|---|
| Thermomixer Comfort | Eppendorf |
| Universal Balance | Sartorius |
| V 150 Autoclave | Systec |
| Xcalibur PX Ultra X-radiation Diffractometer | Oxford Diffraction |

**3.1.2 Consumables**

| Material | Manufacturer |
|---|---|
| Amicon-Ultra centrifuge filter | Millipore |
| C18 Column | Waters |
| PVDF Blot Membrane | Roche |
| DEAE Sepharose Fast Flow | GE-Healthcare |
| Dialysis Tubes Spectra/Por | Spectrum Laboratories |
| DNA Mini Kit | Qiagen |
| EasyXtal DG-Crystal Support X-Seal | Qiagen |
| Electroporation Cuvettes | Biorad |
| Erlenmeyer Flasks | Schott Duran |
| Filter Membranes (0.45 μm/0.22 μm) | Millipore |
| GST Trap High Performance | GE-Healthcare |
| Screw-capped Glass Bottles | Schott Duran |
| His-Trap High Performance/Fast Flow | GE-Healthcare |
| Hi Load Superdex 75 16/60 pg | GE-Healthcare |
| Hi Load Superdex 200 16/60 pg | GE-Healthcare |

| Partisil 10 SAX Column | Bischoff |
|---|---|
| Plasmid Miniprep Kit | Fermentas |
| QuickChange® II Site-directed Mutagenesis Kit | Stratagene |
| Tips and Tubes | Sarstedt |
| UV cuvettes (Plastic/Quartz) | Sarstedt |

### 3.1.3 Media, chemicals, and enzymes

All chemicals and reagents were purchased from Fluka, Merck, Roth, Roche, and Sigma–Aldrich, and used without further purification. HPLC solvents were acquired from Merck Ltd. The bacterial growth media was 2X Tryptone–Yeast (TY) [1.6% tryptone (w/v), 1% yeast extract (w/v), 0.5% NaCl (w/v)] or Luria-Bertani (LB) media [1% tryptone (w/v), 0.5% yeast extract (w/v), 0.5% NaCl (w/v), pH adjusted to 7.0 with NaOH]. Antibiotics used for selections were added at the following final concentrations: 100 μg of ampicillin/ml, 25 μg of kanamycin/ml, 35 μg of chloramphenicol/ml, and 25 μg tetracycline/ml. All restriction enzymes were purchased from New England Biolabs or Fermentas. All PCR enzymes and other necessary DNA isolation and PCR purification kits were purchased from Invitrogen, Roche, Fermentas, or Promega.

### 3.1.4 Vector and expression hosts

| Vectors | Manufacturer |
|---|---|
| pQE-30 and pQE-60 | Qiagen |
| pGEX-6P-1 | GE-Healthcare |
| pET-Duet-1 and pET-Blue-2 | Novagen |
| pGEM-T Easy | Promega |

| Cloning host strains | |
|---|---|
| *E. coli* DH5α | Invitrogen |
| *E. coli* XL-1 Blue | Novagen |
| **Expression host strains** | |
| *E. coli* BL21 (DE3) | Novagen |
| *E. coli* B834[DE3] | Novagen |
| *E. coli* M15[pREP4] | Qiagen |

### 3.1.5 Cryo-tools and crystallization materials

| Material | Manufacturer |
|---|---|
| Intelli-Plate-96-well | Art-Robbins Instruments |
| Magnetic Base Crystal Caps | Hampton Research |
| Nylon Cryo-loops | Hampton Research |
| Vaseline | Hampton Research |
| Crystal Storage Vials | Hampton Research |
| Cryo-canes | Hampton Research |
| Magnetic Crystal Wand | Hampton Research |
| Micro Tools | Hampton Research |
| Cryschem Plate | Hampton Research |
| Crystal Clear Sealing Tape | Henkel |
| Cryoloops (Litho) | MiTeGen |

## 3.2 Methods

### 3.2.1 Catalytic N-terminal Rel fragments from *Streptococcus dysgalactiae subsp. equisimilis* (1-385; 1-340)

#### 3.2.1.1 Rel$_{Seq}$1-385 (Rel$_{Seq}$385)

The functional domains in Rel$_{Seq}$385 are (p)ppGpp-synthetase and -hydrolase. For further characterization of this protein fragment in particular with drug design in mind, a methodology has been implemented for analysis using a series of substrate nucleotides and non-hydrolyzable substrate and product analogs. Hence, the Rel$_{Seq}$385-encoding plasmid pENH385 was transformed in *E. coli* BL21 (DE3) for overproduction of protein.

#### 3.2.1.1.1 Recombinant protein production

A starter-culture volume with 50 ml of 2X TY medium was inoculated with the *E. coli* BL21 (DE3) pENH385 transformant and grown overnight at 37°C with shaking. The next day, the starter volume was subcultured in 4000 ml 2X TY media containing ampicillin at 37°C until the cells reached an optical density of 0.8 at 600 nm. Recombinant gene expression was induced by addition of 1 mM IPTG to the liquid culture and the cells were grown further for 4 h at 37°C. The cells were then harvested by centrifugation at 5000 x*g* for 30 min at 4°C. The resulting pellet was suspended in 100 ml of lysis buffer *RelSeq385-A* (see below). Lysozyme was added to a final concentration of 1 mg/ml together with a tablet of protease-inhibitor cocktail [complete, EDTA-free (Roche)] and the cells were then subjected to 2X French press treatment (1200 psi) in order to break their outer membrane. The lysate was centrifuged at 15000 xg (Ultracentrifuge, Beckman-Coulter) at 4°C for 90 minutes to remove the broken membrane and the cell debris. The supernatant was filtered and loaded onto 5 -ml His-Trap column (GE-Healthcare) at 4°C. The column was washed with 1000 ml of washing buffer *RelSeq385-B* (see below). Elution of the bound protein was achieved by the gradient addition of 200 ml of elution buffer *RelSeq385-C* (see below). The eluted fractions were analyzed on a 12% SDS-polyacrylamide gel and the fractions containing the highest amount of protein were loaded onto a cellulose tubular membrane, molecular mass cut off 12000-14000 Da, and dialyzed overnight in buffer *RelSeq385-D* (see below) at 4°C. After dialysis, the protein was

concentrated by using an Amicon concentrator and quantified spectrophotometrically by measuring the UV absorbance at 280 nm or by the Bradford assay.

Buffer solutions:

*RelSeq385-A:* 20 mM Tris-HCl, pH 8.0 (25°C); 500 mM NaCl; 10 mM imidazole.

*RelSeq385-B:* 20 mM Tris-HCl, pH 8.0 (25°C); 500 mM NaCl; 20 mM imidazole.

*RelSeq385-C:* 20 mM Tris-HCl, pH 8.0 (25°C); 500 mM NaCl; 20 mM imidazole.

*RelSeq385-D:* 20 mM Tris–HCl, pH 7.0 (25°C); 1000 mM NaCl; 10% glycerol (v/v).

## 3.2.1.1.2 Formation of crystalline complexes between Rel$_{Seq}$385 and nucleotides or nucleotide analogs

Rel$_{Seq}$385 (10 mg/ml) in *Relseq385-D* (see above) was mixed with an equal volume buffer solution listed in Table 3.1.

**Table 3.1:** List of complexes crystallized and their respective substrate and/or analog crystallization mixture

| Complexes | Crystallization mixture |
|---|---|
| Complex I (co-crystallized) | 5 mM GTP<br>5 mM MgCl2<br>25 mM Bis-Tris propane-HCl pH 9.0<br>12.5 mM compound (10) |
| Complex II (soaked) | 5 mM GppNHp<br>5 mM MgCl$_2$<br>25 mM Bis-Tris propane-HCl pH 9.0<br>5 mM compound (15) |
| Complex III (co-crystallized) | 9 mM GppNHp<br>3 mM ApCH$_2$pp<br>5 mM MgCl$_2$<br>25 mM Bis-Tris propane-HCl pH 9.0 |
| Complex IV (co-crystallized) | 9 mM GppNHp<br>5 mM MgCl$_2$<br>25 mM Bis-Tris Propane-HCl pH 9.0 |

Well-diffracting polygonally shaped crystals were obtained within 4 - 7 days in hanging drops by mixing 2 µl protein-substrate-analog solution with an equal volume

of reservoir solution containing 23% PEG 8000, 650 mM NaCl, and 100 mM Tris-HCl, pH 8.4 (25°C).

### 3.2.1.1.3 Data acquisition for complex I

Rel$_{Seq}$385-compound (10) co-crystals of approximate dimensions $0.4 \times 0.3 \times 0.3$ mm$^3$ were individually fished from hanging drops with nylon loops of diameter 0.4 - 0.5 mm. Each crystal was immediately transferred into the cryobuffer (26% PEG 8000, 100 mM Tris-HCl pH 8.5 at 25°C) and subsequently flash-cooled to 100 K in a cold nitrogen-gas stream. A complete dataset was obtained from one cryo-cooled crystal at synchrotron beamline I911-3 ($\lambda = 1.0$ Å) at MAX-Lab, Lund, Sweden. The crystal was maintained at a constant temperature (100 K) and a total of 360 images ($\Delta\varphi = 0.5°$/image) were recorded on a Mar image-plate detector with data extending to 2.70 Å resolution.

### 3.2.1.1.4 Crystal soaking and data acquisition for complex II

Crystals were individually fished from hanging-drops with nylon loops of diameter 0.3 - 0.4 mm and subjected to two consecutive washing steps in buffer containing 24% PEG 8000, 500 mM NaCl, and 100 mM Tris-HCl pH 8.5 at 25°C. Subsequently, the crystals were soaked with compound (15) for various lengths of time prior to cryocooling and data collection. A successful crystal was obtained by the addition of 5 mM compound (15) to hanging drops containing GppNHp co-crystals followed by 12 hours of soaking. The crystal was transferred into the cryobuffer (26% PEG 8000, 100 mM Tris-HCl pH 8.5 at 25°C) and subsequently flash-cooled to 100 K in a cold nitrogen-gas stream. A complete dataset was obtained from the crystal at synchrotron beamline 14.1 ($\lambda = 0.91841$ Å) at BESSY, Berlin, Germany. The crystal was retained at a constant temperature (100 K) in the cryostream. A total of 360 images ($\Delta\varphi = 0.5°$/image) were recorded using an MX 225 - CCD detector with data extending to 2.47 Å resolution.

### 3.2.1.1.5 Data acquisition for complexes III and IV

Crystals of approximate dimensions $0.5 \times 0.4 \times 0.4$ mm$^3$ were flash-cooled as described in section 3.2.1.1.3. Two datasets from two different Rel$_{Seq}$385 crystals

(complex III and complex IV; Table 3.1) were obtained separately using synchrotron beamline 14.1 ($\lambda$ = 0.91841 Å) at BESSY, Berlin, Germany. The complex III crystal diffracted synchrotron X-rays to 2.55 Å resolution, whereas the complex IV diffracted synchrotron X-rays to 2.15 Å.

**3.2.1.1.6 Data processing, scaling, and structure solutions of complexes I to IV**

All datasets were processed with MOSFLM [Leslie, 1992] and scaled and merged using SCALA [Evans, 2006]. Isomorphism of the complexes with the $Rel_{Seq}385$ [Hogg et al., 2004; PDB ID: 1VJ7] crystals allowed initial phases to be derived directly from the monomeric $Rel_{Seq}385$ [poly (Ala/Gly/Ser) search model] coordinates by molecular replacement using PHASER [McCoy et al., 2007]. In order to improve the electron density especially at the active sites, protein-backbone conformations were remodeled. Restraint libraries for compound (10) and (15) were constructed utilizing bond-length and angle parameters obtained from standard GDP and ppGpp (G4P) libraries from the Hetero-compound Information Center (HIC-Up server; http://xray.bmc.uu.se/hicup) [Kleywegt and Jones, 1998]. To ensure that stereochemical restraints imposed on the nucleotide moieties during the refinement process had not biased the geometry of the resulting models in the active site, restraints were removed from the nucleotides or nucleotide analogs and a subsequent round of simulated annealing refinement was carried out in PHENIX [Adams et al., 2010]. Coordinates for the GTP, GppNHp, other nucleotide analogs, $Mn^{2+}$, and water molecules were refined until no further $|F_o|-|F_c|$ difference density peaks appeared in the iterative process. Significant improvements were obtained by application of TLS refinement [Painter & Merritt, 2006] as implemented in PHENIX [Adams et al., 2010] in the final stages of model building and refinement. A total of three TLS groups per monomer [TLS group1: (p)ppGpp hydrolase; TLS group2: central 3-helix bundle (C3HB); and TLS group3: (p)ppGpp-synthetase domains] were selected to model rigid atomic displacements. The final step of maximum-likelihood-based refinement was performed using REFMAC [Murshudov et al., 1997]. Inspection of electron density maps and model building were conducted with the graphics program COOT [Emsley and Cowtan, 2004]. All root-mean-square deviations were calculated using the least-squares fit algorithm LSQMAN [Kabsch, 1976]. Final model stereochemistry was monitored with PROCHECK [Laskowski et al., 1993]. Nucleotides, nucleotide analogs, and their interaction schemes were plotted using

LIGPLOT [Wallace et al., 1995]. Molecular images were created with PyMOL [Schrödinger] and/or Chimera [Pettersen et al., 2004].

### 3.2.1.2 Rel$_{Seq}$385: Metal ion analysis for the hydrolase domain

It was to be determined whether the metal ion involved in the hydrolase domain of Rel$_{Seq}$385 is manganese or zinc. Hence, Rel$_{Seq}$385 was overexpressed, purified, and crystallized, for further analyses as described in section 3.2.1.1.

### 3.2.1.2.1 Absorption edge scans and X-ray data collection

Rel$_{Seq}$385 crystals were transferred to a cryobuffer solution (26% PEG 8000, Tris-HCl pH 8.5 at 25°C), and flash-cooled to 100 K using an Oxford Cryostream. Individual fluorescence scans were recorded at the Zn-K- and the Mn-K- edges to check for the presence of the metal ions, and to ascertain the precise energies of the absorption edges. The absorption edge scans for Rel$_{Seq}$385 crystals were performed using the automated edge-scan functions at the 14.2 beamline, BESSY, Berlin, Germany. Complete X-ray anomalous datasets, consisting of 180 x 1° oscillations, were collected at the Zn-K (9879.55 eV), and Mn-K (6553.86 eV) edges from a single Rel$_{Seq}$385 crystal to 3.5 Å resolution. The datasets were processed and scaled using MOSFLM [Leslie, 1992] and SCALA [Evans, 2006], respectively.

### 3.2.1.2.2 Structure determination and anomalous scattering analysis

The structures of Rel$_{Seq}$385 from the anomalous diffraction datasets were determined by molecular replacement using the program PHASER [McCoy et al., 2007] with a metal-free Rel$_{Seq}$385 [Hogg et al., 2004; PDB ID: 1VJ7] as a search model. The position of metal ions at each hydrolase site was located using anomalous difference Fourier map ($\Delta F_{ano}$) by application of *phenix.maps* as implemented in PHENIX [Adams et al., 2010]. The intensities of the anomalous peaks at each metal site (e/Å$^3$) were determined using the program COOT [Emsley and Cowtan, 2004].

### 3.2.1.2.3 Atomic-absorption spectroscopy

Atomic-absorption spectroscopy (AAS) is one of the most effective methods for elemental analysis. Electro-thermal atomic-absorption spectroscopy (ETAAS) or graphite furnace atomic-absorption spectroscopy (GFAAS) is often used for the analysis of biological materials such as bacteria, proteins, and so forth. GFAAS has

major advantages such as high sensitivity and suitability for small samples [Levin et al., 2001]. As an example, it has been reported that metal preference in mouse hepatitis viral non-structural protein 10 (Nsp10) was evaluated using GFAAS. The report indicated that the Nsp10, which binds nucleic acids and metal ions, prefers zinc over iron and cobalt [Matthes et al., 2006].

The amounts of co-purified zinc and manganese ions were measured from purified $Rel_{Seq}385$ samples using a polarized Zeeman Atom Absorption Spectrometer 180-80 with tube cuvette (Hitachi) (Table 3.2). A dilution series was used for standard measurements with stock solutions of $Zn(NO_3)_2$ and $Mn(NO_3)_2$. The concentration of the standard solutions ranged from 0 to 1 µM for zinc and from 0 to 10 µM for manganese. Additionally, the metal-ion preference of $Rel_{Seq}385$ between zinc and manganese was determined by a competition assay. The co-purified metal ions from 100 µM $Rel_{Seq}385$ were chelated by addition of 50 mM EDTA. Following dialysis, the EDTA-free and metal-free $Rel_{Seq}385$ was treated with $MnCl_2$, $ZnCl_2$, and an equal molar ratio of both (Table 3.3) for analyzing the metal preference. Prior to measurement, the samples were dialyzed in 20 mM Tris-Hcl pH 7.0 (25°C), 500 mM NaCl, and 5 % (v/v) glycerol.

**Table 3.2** Materials and conditions used for GFAAS

| Hollow cathode lamp | Zinc | Manganese |
|---|---|---|
| Wavelength | 213.8 nm | 279.5 nm |
| Slit width | 1.3 nm | 0.4 nm |
| Working current | 3.5 mA | 7.5 mA |
| Cuvette | Tube | Tube |

**Table 3.3** Zinc versus manganese GFAAS analysis

| No. | Samples | $ZnCl_2$ | $MnCl_2$ |
|-----|---------|----------|----------|
| 1 | $Rel_{Seq}385$ (100 µM; post-EDTA treatment) | 100 µM | - |
| 2 | $Rel_{Seq}385$ (100 µM; post-EDTA treatment) | - | 100 µM |
| 3 | $Rel_{Seq}385$ (100 µM; post-EDTA treatment) | 100 µM | 100 µM |
| 4 | $Rel_{Seq}385$ (100 µM; post-EDTA treatment; negative control) | - | - |
| 5 | Dialysis buffer (negative control) | - | - |
| 6 | $Rel_{Seq}385$ (100 µM; pre-EDTA treatment; positive control) | - | - |

### 3.2.1.3 $Rel_{Seq}$1-340 ($Rel_{Seq}$340)

In the reported $Rel_{Seq}385$ crystal structure [Hogg et al., 2004], the polypeptide chain beyond residue 341 exhibited high flexibility, disorder, and very poor electron density. In order to study a structurally well-defined segment (residues 1-340) that can hydrolyze and synthesize (p)ppGpp, a construct was generated by deletion PCR with 45 amino-acid residues deleted from the C-terminus of $Rel_{Seq}385$.

#### 3.2.1.3.1 Molecular cloning and heterologous expression

The pET-pre01 and the pGEX-pre01 vectors are designed to produce proteins linked by a Prescission Protease™- cleavable N-terminal $His_6$-tag and N-terminal GST-tag, respectively. These vectors also share same restriction sites (NdeI/XhoI), which is ideal for parallel cloning. Two PCR steps were performed for generating a $Rel_{Seq}340$ construct.

*Step 1: In-vitro* mutagenesis PCR – silent mutation for histidine codon exchange.

A silent PCR mutagenesis was necessary, as the pENH385 plasmid holds an internal restriction site for NdeI (5'-CA'TATG-3') on $Rel_{Seq}385$ at H205, which is in conflict with the vectors. Using the "Quick Change-II-site-directed Mutagenesis" protocol

(Qiagen), the initial step was performed (H205H; CAT to CAC - histidine codon exchange). The primers used for site-directed mutagenesis were H205HF and H205HB (see below). The resultant plasmid pENH385a, was confirmed by sequencing.

*Step 2:* Truncation PCR – deletion of 45 residues from the C-terminus of Rel$_{Seq}$385

The Rel$_{Seq}$340 construct was PCR-amplified using primers NRS340F and XRS340R (Table 3.4, see below) with pENH385a as template. The PCR product was digested with NheI/XhoI and inserted into pET-pre01 and pGEX-pre01. The resultant plasmids pENH340 and pGNH340 were confirmed by sequencing. Further, pENH340 and pGNH340 were transformed in *E. coli* BL21 (DE3) for protein production.

**Table 3.4:** Oligonucleotide PCR primers for construction of the strain producing Rel$_{Seq}$340

| Primer | Sequence (5' - 3') | Restriction enzyme |
|---|---|---|
| H205H**F** | GAAACGGAGTTTTATAAGATTTCCCACATGATGAATG | * |
| H205H**B** | GCGACGTTTTTCATTCATCATGTGGGAAATC | * |
| NRS340**F** | CGCCATATGGCAAAAGAAATCAATTTAACAG | NdeI |
| XRS340**R** | CGCCTCGAGCTAAGCTACCCCGTACTCAGCCAC | XhoI |

* - Primers used for single-site mutagenesis; **F** (forward) - sense primer; **R** (reverse) or **B** (backward) – antisense primer.

### 3.2.1.3.2 Protein production and crystallization screening

The Rel$_{Seq}$340 protein, fused to a Prescission Protease™- cleavable GST tag, was overproduced by induction with 0.5 mM IPTG at 37°C until cells reached an optical density of 0.8 at 600 nm. Overexpressing cells were harvested from 2000 ml of 2X YT broth. Cells were resuspended in 3 - 5 volumes of lysis buffer *RelSeq340-A* (see below) and disrupted by 2 rounds in the french pressure cell (1200 psi). The cell debris was removed by ultra-centrifugation (1.5 h, 4°C, 25000 x*g*). The lysate was then subjected to filtration through a 0.2 μm filter followed by loading onto the GST-Trap column (GE Healthcare). Prior to use, the column was equilibrated with 5 bed-volumes of the binding buffer *RelSeq340-B* (see below). Further, the column was

washed with 10 bed-volumes of the wash buffer *RelSeq340-C* (see below). After the washing step, the column was subjected to equilibration with cleavage buffer *RelSeq340-D* (see below). One unit of Prescission Protease$^{TM}$ was loaded onto the column and incubated overnight at 4°C for the GST-tag cleavage. A follow-up elution with buffer *RelSeq340-C* resulted in the separation of GST-free Rel$_{Seq}$340 protein. GST separation was controlled by the buffer *RelSeq340-E* (see below). The eluted fractions were analyzed on a 12% SDS-polyacrylamide gel. Purified protein was concentrated upto 5 mg/ml. Preliminary crystallization screening was performed with the Sigma (basic and extension), Nextal pH clear, PACT premier™ (Molecular Dimensions Ltd.), and Hampton screens. Initial crystals of Rel$_{Seq}$340 were obtained using the Hampton Index screen with the conditions *H-340-A* and *H-340-B* (see below). The crystals were polygonally shaped, appeared after two days and grew within five days to a size of approximately 0.1 x 0.05 x 0.05 mm$^3$. These crystals did not diffract and could not be improved by additives or co-crystallization with GDP, GTP or the non-hydrolysable GTP analogs GppNHp and GppCH$_2$p. Since diffraction requires highly ordered molecules in all three dimensions, crystals with an internal disorder give no diffraction pattern. Most likely, the internal packing order of the crystals was limited.

Buffer solutions:

*RelSeq340-A:* 1 mg/ml lysozyme; 1 tablet protease inhibitor cocktail; 50 mM Tris-HCl, pH 7.5 (25°C); 250 mM NaCl; 10 % (v/v) glycerol.

*RelSeq340-B:* 50 mM Tris-HCl, pH 7.5 (25°C); 250 mM NaCl; 10 % (v/v) glycerol.

*RelSeq340-C:* 50 mM Tris-HCl, pH 7.5 (25°C); 500 mM NaCl; 10 % (v/v) glycerol.

*RelSeq340-D:* 2 mM DTT; 2 mM EDTA; 50 mM Tris-HCl, pH 7.5 (25°C); 500 mM NaCl; 10 % (v/v) glycerol.

*RelSeq340-E:* 50 mM Tris–HCl, pH 7.5 (25°C); 500 mM NaCl; 10% glycerol (v/v); 20 mM reduced glutathione

*H-340-A:* 10 mM GTP; 2 M ammonium sulphate; 100 mM Bis-Tris pH 6.5

*H-340-B:* 10 mM GppNHp; 2 M ammonium sulphate; 100 mM HEPES pH 7.5

### 3.2.1.4 *In-vitro* (p)ppGpp synthetase-activity assays

To check the (p)ppGpp synthetase activity of the purified enzymes, a reaction mixture *Syn-mix-A* (see below) was freshly prepared. 20 μM of $Rel_{Seq}385$ or $Rel_{Seq}340$ together with *Syn-mix-A* were mixed in a total volume of 20 μL. Synthetase reactions were performed at 37°C for a period of 30 min. The reactions were stopped by the addition of 2 μl of 15 M formic acid. Reaction products were analysed and separated by ion-exchange chromatography (Partisil 10 SAX column 4.6 X 250 mm; Bischoff) using the HPLC-HPRP module of the proteomeLab PF2D (Beckman-Coulter). Partisil SAX 10 is a strong anion exchanger based on quaternary ammonium groups. It has been reported in the literature for the separation of nucleotides [Viducic et al., 2006]. Before injection of the sample into the Partisil column, the stopped reaction mix was diluted 10-fold in *Syn-sep-A* (see below). Nucleotides were eluted at a flow rate of 1 ml/min using the gradient made of low (*Syn-sep-A buffer*) and high (*Syn-sep-B* buffer) ionic-strength buffers. The area under the peak corresponding to the separated nucleotides at 254 nm was determined in comparison to an internal standard of 5 mM cAMP.

Buffer solutions:

*cAMP stock:*    500 mM in water.

*Syn-mix-A:*    6 mM GTP; 8 mM ATP; 25 mM Bis-Tris propane - HCl , pH 9.0;

   10 mM $MgCl_2$

*Syn-sep-A:*    7 mM $KH_2PO_4$, pH 4.0 adjusted with $H_3PO_4$

*Syn-sep-B:*    500 mM $KH_2PO_4$, 500 mM $Na_2SO_4$, pH 5.6 adjusted with KOH.

### 3.2.2 RelA full-length (1-728) and RelA C-terminal domain (365-728) from *Thermus thermophilus* HB8  (RelA$_{Tth}$; and RelA$_{Tth}$365-728)

### 3.2.2.1 Genomic DNA-extraction from *T. thermophilus* HB8

*Thermus thermophilus* is a Gram-negative aerobic eubacteria that can grow at extreme temperatures ranging from 50°C to 82°C. The *Thermus thermophilus* HB8 strain as a dried culture was obtained from German Collection of Micro Organisms and Cell Cultures (Leibniz-Institute DSMZ), Braunschweig, Germany. Revival of the dried

culture under sterile conditions was performed by rehydration of dried cultures from the ampoule. The rehydrated culture was transferred into a sterile 1000-ml Erlenmeyer flask containing 250 ml of sterile LB-broth. Further, the cells were incubated in LB-broth at 65°C for 18 hours with constant shaking. Genomic DNA from *Thermus thermophilus* HB8 wild-type was extracted using a Qiagen DNA extraction kit.

**3.2.2.2 Molecular cloning and heterologous expression**

In parallel, the *T. thermophilus* HB8 *relA* gene (1 to 2184 nucleotides) coding for RelA$_{Tth}$ and C-terminal region of *relA* gene (1092 to 2184 nucleotides) coding for RelA$_{Tth}$ 364-728 were PCR-amplified from the *T. thermophilus* HB8 genomic DNA. The forward primers for *relA* (TTS-F) and the C-terminal region of *relA* (TTS-M), and a common reverse primer (TTS-B) are listed in Table 3.5 (see below). Both the forward primers were designed with the same restriction site overhangs, EcoRI. The reverse primer was designed with the restriction site overhang, EcoRV. Also, an optional TEV-protease cleavage-encoded sequence in the forward primers following the EcoRI site was introduced. The amplicons were digested with EcoRI and EcoRV and cloned into the pETDuet-1 vector system with a His$_6$-tag at the N – terminus of the multiple cloning site-1. The results were confirmed by sequencing. The resultant plasmids, pETDuet-1-TTF and pETDuet-1-TTC, were transformed in *E. coli* BL21 (DE3) for expression and production.

**Table 3.5:** Oligonucleotide primers used for construction of the strains producing RelA$_{Tth}$ and RelA$_{Tth}$ 365-728

| Primer | Sequence (5' - 3') | Restriction enzyme |
|---|---|---|
| TTS-**F** | GCGAATTCGGAGAACCTGTACTTCCAGTCGATGGTCCGCGCGGATCTC | EcoRI |
| TTS-**M** | GCGAATTCGGAGAACCTGTACTTCCAGTCGTGGCTCTATAAGGAGGGGCT | EcoRI |
| TTS-**B** | GCGATATCTCAGGCCCAGCGCGCCTC | EcoRV |

**F** (forward) / **M** (mid) – sense primer; **B** (backward) – antisense primer.

### 3.2.2.3 Protein production and crystallization screening

Both full-length and C-terminal half proteins were produced in the same manner and purified by Ni$^{2+}$-NTA-affinity chromatography. Cells were induced with 1 mM IPTG at 37°C after an optical density of 0.6 at 600nm had been reached. Overexpressing cells were harvested from 6000 ml of 2X YT-broth at 5000 x$g$ for 1 hour at 37°C. Pelleted cells were resuspended in 5 volumes (pellet) of lysis buffer *RATT-A* (see below) containing EDTA-free protease inhibitor cocktail and subjected to 3 rounds of french press cell treatment (1000 psi). The cell debris was removed by ultra-centrifugation at 50000 x$g$ for 90 minutes at 37°C. The lysate was then subjected to filtration through a 0.2 μm filter followed by heating at 70°C for 10 minutes. The lysate with non-specific protein precipitate was centrifuged by ultra-centrifugation at 50000 x$g$ for 30 minutes at 37°C. Prior to loading, the His-trap column was equilibrated with 5 bed-volumes of the binding buffer *RATT-B* (see below). Further, the column was washed with 10 bed-volumes of the wash buffer *RATT-C* (see below), followed by a linear-gradient addition with buffer *RATT-D* (see below). SDS-PAGE analysis from full length and C-terminal domain purification showed an unexpected band in Coomassie blue staining, with moderate amounts of proteolysis. However, the separated protein was desalted in storage buffer *RATT-E* (see below). Preliminary crystallization screening was performed with the Sigma (basic and extension), Nextal pH clear, PACT premier™ (Molecular Dimensions Ltd.), and Hampton screens. Initial attempts to crystallize both full-length and C-terminal domain were unsuccessful. Further, extensive biochemical characterization and crystallization trials on both full-length and C-terminal domain of RelA$_{Tth}$ were performed and reported by Manuela Gorgel [Gorgel, 2009].

Buffer solutions:

*RATT-A:*    50 mM Tris-HCl, pH 8.8 (25°C); 500 mM NaCl.

*RATT-B:*    50 mM Tris-HCl, pH 8.8 (25°C); 500 mM NaCl; 5 mM imidazole.

*RATT-C:*    50 mM Tris-HCl, pH 8.8 (25°C); 500 mM NaCl; 15 mM imidazole.

*RATT-D:*    50 mM Tris-HCl, pH 8.8 (25°C); 500 mM NaCl; 500 mM imidazole.

*RATT-E:*    50 mM Tris–HCl, pH 8.8 (25°C); 500 mM NaCl; 10% glycerol (v/v).

**3.2.3 RelA full-length (1-744) and SpoT full-length (1-702) from *Escherichia coli* K-12 (RelA$_{Ec}$; SpoT$_{Ec}$)**

In an attempt to elucidate the structure of the full-length proteins, a series of constructs expressing RelA and SpoT were generated using *E. coli* genomic DNA.

**3.2.3.1 PCR amplification and cloning of *relA* and *spoT* from *Escherichia coli* K-12 genomic DNA**

The wild-type *Escherichia coli* K12 strain was revived from in-house glycerol stocks and subcultured in a 1000-ml Erlenmeyer flask containing 200 ml LB broth at 37°C with constant shaking. After 16 hours of incubation, the cells were harvested by centrifugation at 4000 x*g* at 4°C. From the harvested cells, genomic DNA was extracted using a Qiagen DNA extraction kit protocol and quantified spectrometrically at 260 nm.

In parallel, the *E. coli relA* gene of 2235 bp coding for 744 amino-acid residues and the *E. coli spoT* gene of 2109 bp coding for 702 amino-acid residues were PCR-amplified from the extracted genomic DNA using a set of primers ERA_F/ERA_B and EST_F/EST_B, respectively (Table 3.6, see below). Both the primers for *relA* and *spoT* were designed with the same restriction-site overhangs (BamHI/EcoRI). The amplicons of *relA* and *spoT* were digested with BamHI and EcoRI and cloned into the plasmids pGEX-6P-1 (GST-tag) and pQE30-Prl (His$_6$-tag). The resultant plasmids, pGEX-6P-1-RelA, pQE30-Prl-RelA, pGEX-6P-1-SpoT, pQE30-Prl-SpoT were transformed in *E. coli* BL21 (DE3) for expression and purification.

**Table 3.6:** Oligonucleotide PCR primers used for construction of the strains producing RelA$_{Ec}$ and SpoT$_{Ec}$

| Primer | Sequence (5' - 3') | Restriction enzyme |
|--------|--------------------|--------------------|
| ERA_**F** | CCAAGGATCCATGGTTGCGGTAAGAAGTGC | BamHI |
| ERA_**B** | CGCCTCGAGCTAACTCCCGTGCAACCGAC | XhoI |
| EST_**F** | CGCGGATCCATGTATCTGTTTGAAAGCCTGAATC | BamHI |
| EST_**B** | GCGCTCGAGTTAATTTCGGTTTCGGGTGAC | XhoI |

**F** (forward) - sense primer; **R** (reverse) or **B** (backward) – antisense primer.

### 3.2.3.2 Purification, synthetase activity, and preliminary crystallization screening of RelA$_{Ec}$

The pQE30-Prl-RelA-transformed cells were grown in 2X TY-media to an optical density of 0.8 at 600 nm, induced with 1 mM IPTG, and further grown for 3 hours at 37°C with constant shaking. The cells were harvested by centrifugation at 5000 x$g$ for 10 min, lysed in lysis buffer *RAFE-A* (see below) by two rounds of sonication of 5 min on ice and the lysate was cleared by centrifugation at 20000 x$g$ for 15 min at 4°C. The supernatant was loaded onto a His-Trap column pre-equilibrated with the equilibration buffer *RAFE-B* (see below). The column was washed with 100 column volumes of wash buffer *RAFE-C* (see below) and the protein was eluted with the elution buffer *RAFE-D* (see below). The eluted protein was dialyzed against *RAFE-E* (see below) to remove imidazole and concentrated up to 3 mg/ml. Protein aliquots were flash-cooled in liquid nitrogen and stored at -80°C.

Preliminary crystallization screening was performed with the Sigma (basic and extension), Nextal pH clear, PACT premier™ (Molecular Dimensions Ltd.), and Hampton screens, deploying a crystal robot (Art-Robbins) with 250-nanoliter drop setup. Attempts to crystallize RelA$_{Ec}$ were unsuccessful. Since a diffraction quality crystal requires highly ordered molecules in all three dimensions, protein with an internal disorder gives no packing. There are several possible reasons explaining why a protein does not crystallize. In most cases the internal order of the protein is limited due to flexible regions being present. Prediction of intrinsically unfolded regions using FoldIndex [Prilusky et al., 2005] suggested that RelA$_{Ec}$ comprises seven disordered segments with a total of 156 disordered residues (see Appendix 6.2). The longest disordered segments were 211-249, 465-524, and 566-594.

*RAFE-A:*       1 mM phenylmethylsulphonyl fluoride, 1 mg/ml lysozyme; 50 mM Tris-HCl, pH 7.9 (25°C); 500 mM NaCl; 5 % (v/v) glycerol.

*RAFE-B:*       50 mM Tris-HCl, pH 7.9 (25°C); 500 mM NaCl; 5 % (v/v) glycerol; 5 mM imidazole.

*RAFE-C:*       50 mM Tris-HCl, pH 7.9 (25°C); 500 mM NaCl; 5 % (v/v) glycerol; 10 mM imidazole.

*RAFE-D:*       50 mM Tris-HCl, pH 7.9 (25°C); 500 mM NaCl; 5 % (v/v) glycerol; 500 mM imidazole.

*RAFE-E:*       50 mM Tris–HCl, pH 7.9 (25°C); 500 mM NaCl; 10% glycerol (v/v).

(p)ppGpp synthetase activity tests and nucleotide separation by HPLC were performed as described in section 3.2.1.4.

### 3.2.3.3 Heterologous expression and preliminary purification of SpoT$_{Ec}$

A transformant carrying pQE30-Prl-SpoT$_{Ec}$ (His$_6$-tag) was grown in 2X TY media, and induced with 1 mM IPTG at an optical density of 0.8 at 600 nm. Following overexpression for 3 hours at 37°C with constant shaking, cells were harvested by centrifugation at 5000 x*g* for 10 min. Purification trials were performed as described above in section 3.2.3.2. Purified protein was analyzed by SDS-PAGE, showing that overexpressed SpoT$_{Ec}$ has solubility and proteolysis issues. As an initial measure, pGEX-6P-1-SpoT$_{Ec}$ (GST-tagged) was analyzed for test expression. The overexpression of SpoT$_{Ec}$ with a GST-tag was assessed by SDS-PAGE. Purification of Prescission Protease$^{TM}$- cleavable GST-tagged SpoT$_{Ec}$ was performed as described earlier in section 3.2.1.3.2. Whereas the solubility problem was solved, the proteolytic degradation issue remained.

### 3.2.4 Regulatory C-terminal RelA fragments from *Salmonella typhimurium* (372-744) *and Escherichia coli* K12 (508-744; 526-744; 594-744; 564-744)

### 3.2.4.1 Heterologous expression, purification and crystallization screening of RelA$_{Sty}$372-744

An in-house glycerol stock of pQE30Xa-RelAStyCTD *E.coli* M15 (pREP4) cells that can express *Salmonella typhimurium* RelA CTD (372-744) was revived and tested for the extent of expression. The expression was fairly high. The purification steps were performed using the methods described below in section 3.2.4.3.1. After extensive optimization, a high-salt buffer comprising 50 mM Tris-Hcl pH 8.5, 1000 mM KCl and 20-40 % glycerol was found to be ideal for producing the protein in soluble fractions. Purified protein was analyzed by SDS-PAGE, showing that overexpressed RelA$_{Sty}$372-744 has proteolysis issues. The cleavage product was confirmed as a fragment from the N-terminus of the CTD, as judged by the western blot assay with anti-His antibodies (see Appendix 6.3).

### 3.2.4.2 C-terminal RelA$_{Ec}$ fragments (RelA$_{Ec}$508-744; RelA$_{Ec}$526-744; RelA$_{Ec}$594-744)

Due to solubility issues in the initial screening stages of purification and crystallization of RelA$_{Sty}$372-744 (section 3.2.4.1, see above) and RelA$_{Ec}$564-744 (section 3.2.4.3, see below), the amino-acid distribution in the *E.coli* RelA C-terminal region (residues 500-744) was analysed for a potentially stable fragment using protparam [Gasteiger et al., 2005], and fold-prediction using FoldIndex[®] [Prilusky et al., 2005]. Hence, for crystallization purposes and functional studies, the construction of a library of truncated C-terminal fragments of RelA$_{Ec}$ was initiated. At the outset, three constructs were generated using PCR-truncation mutations. The PCR-truncation mutations were performed in a single step. Different sets of oligonucleotide primers were designed for amplifying the C-terminal gene fragments of *relA* for cloning into the His$_6$-tagged pQE60 vector system. The primers used for cloning are listed in Table 3.7. Three different fragments were PCR-amplified using forward primers ECT_F1, ECT_F2 and ECT_F3 and a common reverse primer ECT_R1 with pGEX-6P-1RelA$_{Ec}$ (section 3.2.3.1) as template. Three constructs, varying in length, were cloned into the pQE60 vector (residues 508-744 as pQE60-RelA-CTD-1; residues 526-744 as pQE60-RelA-CTD-2; residues 594-744 as pQE60-RelA-CTD-3). The

constructs were expressed and one of the protein products was purified using conditions employed for RelA$_{Ec}$ 564-744 as described below in section 3.2.4.3.1. Preliminary crystallization screening was performed using the Sigma Basic and Extension screens, Nextal pH clear Screen, and Structure screen (Molecular Dimensions Ltd.). However, attempts to crystallize these protein fragments were unsuccessful.

**Table 3.7:** Oligonucleotide PCR primers for construction of the various strains producing RelA$_{Ec}$ C-terminal fragments.

| Primer | Sequence (5' - 3') | Restriction enzyme |
|---|---|---|
| ECT_**F**1 | GCCCATGGCTGGGCGGCAAATCCTTG | NcoI |
| ECT_**F**2 | GCCCATGGCAGAAAAACATCTGCTGCC | NcoI |
| ECT_**F**3 | GCCCATGGGTCGCGTGGTAGTCGAAG | NcoI |
| ECT_**R**1 | CGCTCGAGACTCCCGTGCAACCGACG | XhoI |
| ECT_**R**2 | CGAGATCTACTCCCGTGCAACCGACG | BglII |

**F** (forward) - sense primer; **R** (reverse) or **B** (backward) – antisense primer.

### 3.2.4.3 The ribosome-binding C-terminal RelA fragment from *Escherichia coli* K-12 (RelA$_{Ec}$564-744)

### 3.2.4.3.1 Recombinant protein production

The isolated plasmid, pQE30 *E.coli* RelA C-terminal fragment (amino-acid residues 564-744) from an in-house glycerol stock was transformed into *E.coli* M15 (pREP4) cells for expression. RelA$_{Ec}$564-744 was overproduced by induction with 1 mM IPTG at 37°C, after an optical density of 0.8 at 600 nm had been reached. Over-expressed cells were harvested from 6000 ml of 2X YT-broth. Cells were resuspended in 3 - 5 volumes (pellet) of lysis buffer *RACE-A* (see below) and by a combination of treatments with a dissolved EDTA-free protease inhibitor cocktail and 2 rounds of french press cell treatment (1000 psi). The cell debris was removed by ultra-centrifugation (90 min, 4°C, 50000 x*g*/TFT 45 rotor). The lysate was subjected to filtration through a 0.2 μm filter followed by loading onto His-Trap column (GE-Healthcare). Prior to use, the column was equilibrated with 5 bed-volumes of the

binding buffer *RACE-B* (see below). Further, the column was washed with 10 bed-volumes of the wash buffer *RACE-C* (see below)*,* followed by a linear gradient elution with elution buffer *RACE-D* (see below). Purification of the RelA$_{Ec}$564-744 protein to near homogeneity could be achieved by this procedure. Purified protein was judged by SDS-PAGE analysis and dialyzed or desalted in storage buffer *RACE-E* (see below).

Buffer solutions:

*RACE-A:*  50 mM Tris-HCl, pH 8.5 (25°C); 900 mM KCl; 20 % (v/v) glycerol;

*RACE-B:*  50 mM Tris-HCl, pH 8.5 (25°C); 900 mM KCl; 40 % (v/v) glycerol; 10 mM imidazole.

*RACE-C:*  50 mM Tris-HCl, pH 8.5 (25°C); 900 mM KCl; 40 % (v/v) glycerol; 25 mM imidazole.

*RACE-D:*  50 mM Tris-HCl, pH 8.5 (25°C); 900 mM KCl; 40 % (v/v) glycerol; 500 mM imidazole.

*RACE-E:*  50 mM Tris–HCl, pH 8.5 (25°C); 1000 mM KCl; 40% glycerol (v/v).

### 3.2.4.3.2 Crystallization

Preliminary crystallization screening was performed using the Sigma basic and extension screens, Nextal pH clear Screen, and Structure screen (Molecular Dimensions Ltd.). After extensive optimization, single plate-like crystals were obtained within 3 - 4 weeks at 22°C in hanging drops by mixing 1.5 μl of the protein solution with an equal volume of reservoir solution containing 1500 – 2000 mM ammonium sulphate, 800 – 1000 mM KCl, and 100 mM NaOAc, pH 4.6.

### 3.2.4.3.3 Cryopreservation, data acquisition and processing

Crystals were individually fished from hanging drops with nylon loops of 0.05 - 0.1 mm diameter and subjected to a washing step in buffer containing 2 M ammonium sulphate, 800 mM KCl, and 100 mM NaOAc, pH 4.6. Each crystal was transferred into the cryobuffer (20% ethylene glycol (v/v), 100 mM NaOAc pH 4.6) and subsequently flash-cooled to 100 K in a cold nitrogen-gas stream. Two complete datasets were obtained from the crystals at synchrotron beamline 14.1 ($\lambda = 0.91841$ Å;

λ = 1.40000 Å) at BESSY, Berlin, Germany. The crystals were maintained at a constant temperature (100 K) and a total of 360 images (Δφ = 0.5°/image) were recorded on a CCD detector (MX 225) with data extending upto 2.0 Å resolution. Further, the analysis of the protein crystals and elucidation of the crystal structure are described in section 4.3 (see below).

### 3.2.5 50S ribosomal protein L11 from *Escherichia coli K-12*

### 3.2.5.1 Genomic PCR and parallel cloning

Genomic DNA extracted from *E.coli* K12 (described in section 3.2.3.1) was used as template for PCR reactions to amplify the *rplK* (*relC*) gene, which encodes the 15.4-kDa ribosomal protein L11. pET-pre01 and pGEX-pre01 (see Appendix 6.4) were used for cloning with the primers *L11-F* and *L11-B* (Table 3.8). The cloning strategy was the same as described in section 3.2.1.3.1. Gene expression was tested in a series of *E. coli* host strains.

**Table 3.8:** Oligonucleotide PCR primers used for construction of the strains producing L11$_{Ec}$

| Primer | Sequence (5' - 3') | Restriction enzyme |
|---|---|---|
| L11-**F** | GGGAATTCCATATGGCTAAGAAAGTACAAGCCT ACCGCTCGAGTTAGTCCTCCACTACCAGGCCC | NdeI |
| L11-**B** | GTCCTCCACTACCAGGCCCATGGAACGTGCAGTA CCTTCGATGGAGCGAGTCATCGCTTCAATGT | XhoI |

F (forward) – sense primer; B (backward) – antisense primer.

### 3.2.5.2 Heterologous expression and purification

Expression of both His- and GST-tagged L11$_{Ec}$ in *E. coli* BL21 (DE3) host strains were successful. Test purifications indicated that the GST-tagged version was comparatively more pure than the His$_6$-tagged version. Hence, a large-scale purification was performed from 4000 ml cell culture overexpressing GST-tagged L11$_{Ec}$. For protein production, cells were harvested and suspended in 15 ml lysis buffer *L11-A* (see below) including a tablet of protease inhibitors (Roche). Cells were lysed using a French pressure cell treatment (1500 psi). After centrifugation (1.5 h, 4°C, 5000 x*g*), the supernatant was loaded onto a GST-Trap column (GE Healthcare).

After extensive washing with buffer *L11-A* (see below), the column was equilibrated with cleavage buffer *L11-C* (see below). Further, the affinity tag was removed by loading 1 unit of Prescission Protease$^{TM}$ (4°C, 16 h). Subsequently, highly pure $L11_{Ec}$ was eluted from the column using buffer *L11-A*. Protein homogeneity was judged by SDS-PAGE analysis (see Appendix 6.4).

Buffer solutions:

*L11-A*: 50 mM Tris-HCl, pH 8.0 (25°C); 500 mM KCl

*L11-B*: 2 mM EDTA; 2 mM DTT; 50 mM Tris-HCl, pH 8.0 (25°C); 500 mM KCl

*L11-C*: 50 mM Tris-HCl, pH 8.0 (25°C); 500 mM KCl

*L11-D*: 50 mM Tris-HCl, pH 8.0 (25°C); 20 mM reduced glutathione

### 3.2.5.3 Preliminary screening for complex formation with RelA$_{Ec}$564-744

In order to check if purified $L11_{Ec}$ and RelA$_{Ec}$564-744 interact with each other *in-vitro*, gel-filtration analysis was performed. The proteins were mixed at equal molar ratios and dialyzed overnight against stabilizing storage buffer (1 M KCl, 40% glycerol, 50 mM Tris-HCl, pH 8.4 (25°C)). As high glycerol concentrations are not suitable for gel-filtration analysis, the sample was re-dialyzed (1 M KCl, 50 mM Tris-HCl, pH 8.4 (25°C)). After removal of precipitated protein by centrifugation (50000 x*g*, 4°C, 1h), the supernatant was loaded onto a gel-filtration column (GE Healthcare, Superdex 200 16/60) for analysis. One of the preliminary results showed that the $L11_{Ec}$ / RelA$_{Ec}$564-744 sample contained a protein species with a significantly higher molecular mass than the individual proteins (see Appendix 6.4). This species might indicate the formation of a complex consisting of one RelA$_{Ec}$564-744 dimer and one $L11_{Ec}$ monomer. Several studies using *in-vitro* approaches failed to detect $L11_{Ec}$-RelA$_{Ec}$ interaction [Yang & Ishiguro, 2001b; Wendrich et al., 2002; Jenvert & Schiavone, 2007]. In general, to maintain a high turnover in some complex signal pathways, the interactions between the proteins involved occur transiently, resulting in formation of complexes with lifetimes on a millisecond scale. Therefore, careful analysis and experiments on $L11_{Ec}$-RelA$_{Ec}$ interaction might clarify whether they can directly interact with each other.

**Table 3.9: Overall list of proteins and expression strains used**

| Proteins | plasmid | Expression (E. coli) strain | Vector system | Antibiotic selection |
|---|---|---|---|---|
| $Rel_{Seq}$1-385 N-H | *pENH385 | BL21 (DE3) | pET21 (+) | ampicillin |
| $Rel_{Seq}$1-340 N-H | pENH340h | BL21 (DE3) | pET-pre01 | ampicillin |
| $Rel_{Seq}$1-340 N-G | pENH340g | BL21 (DE3) | pGEX-pre01 | ampicillin |
| $RelA_{Ec}$564-744 N-H | *pQE30REC1 | M15 (prep4) | pQE30 | ampicillin & kanamycin |
| $RelA_{Sty}$372-744 N-H | *pQE30xRSC1 | M15 (prep4) | pQE30-Xa | ampicillin & kanamycin |
| $RelA_{Ec}$ N-H | pQE30-Prl-RE | M15 (prep4) | pQE30 | ampicillin & kanamycin |
| $RelA_{Ec}$ N-G | pGEX-6P-1-RE | BL21 (DE3) | pGEX-6p-1 | ampicillin |
| $SpoT_{Ec}$ N-H | pQE30-Prl-SE | M15 (prep4) | pQE30 | ampicillin & kanamycin |
| $SpoT_{Ec}$ N-G | pGEX-6P-1-SE | BL21 (DE3) | pGEX-6p-1 | ampicillin |
| $RelA_{Ec}$508-744 N-H | pQE60REC2 | M15 (prep4) | pQE60 | kanamycin |
| $RelA_{Ec}$526-744 N-H | pQE60REC3 | M15 (prep4) | pQE60 | kanamycin |
| $RelA_{Ec}$594-744 N-H | pQE60REC4 | M15 (prep4) | pQE60 | kanamycin |
| $RelA_{Tth}$ N-H | pET-Duet-1-TTR | BL21 (DE3) | pET-Duet-1 | ampicillin |
| $RelA_{Tth}$365-728 N-H | pET-Duet-1-TTRC | BL21 (DE3) | pET-Duet-1 | ampicillin |
| $L11_{Ec}$ N-H | pET-pre01-EL | BL21 (DE3) | pET-pre01 | ampicillin |
| $L11_{Ec}$ N-G | pGEX-pre01-EL | BL21 (DE3) | pGEX-pre01 | ampicillin |

* Plasmids prepared from in-house glycerol stocks, transformed and directly used for expression in host strains. N-H refers to "N-terminal His$_6$-tag" and N-G refers to "N-terminal GST-tag".

# Chapter 4. Results and Discussion

## 4.1 Rel$_{Seq}$385: Crystal structure determination of the complexes
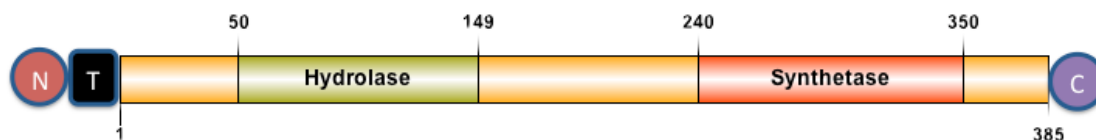


**Figure 4.1.1**: Domain organization of Rel$_{Seq}$385. Hydrolase- or HD- domain (Pfam reference: accession no. PF01966): residues 50-149; synthetase- or RelA_SpoT-domain (Pfam reference: accession no. PF04607): residues 240-350 (domains are defined according to Pfam database, Sanger Institute, UK). N refers to N–terminus, H refers to His$_6$-tag and C refers to C-terminus.

### 4.1.1 Recombinant Rel$_{Seq}$385 production

Purification protocol of Rel$_{Seq}$385 was established by Mechold et al. [2002] for activity assays and followed by Hogg et al. [2004] for crystallization experiments. In this study, the protocol is modified to enhance the stability and solubility of Rel$_{Seq}$385 during purification procedure, storage, and further analyses. Rel$_{Seq}$385 carried a His$_6$ tag at the N-terminus and was purified in two steps, Ni$^{2+}$-NTA affinity and gel-filtration chromatography. Rel$_{Seq}$385 was successfully produced under heterologous conditions, at about 15 mg of protein per liter expression culture. The protein exhibited an apparent molecular mass of about 44 kDa under denaturing conditions in SDS-PAGE (Figure 4.1.2 A). Purified protein fractions were pooled, concentrated to a final concentration of 10 mg/ml and used for crystallization studies. Analytical gel filtration and DLS experiments showed that Rel$_{Seq}$385 is predominantly a monomer. (p)ppGpp synthetase activity tests provided evidence that the fragment is synthetase-active (Figure 4.1.3; Table 4.1).
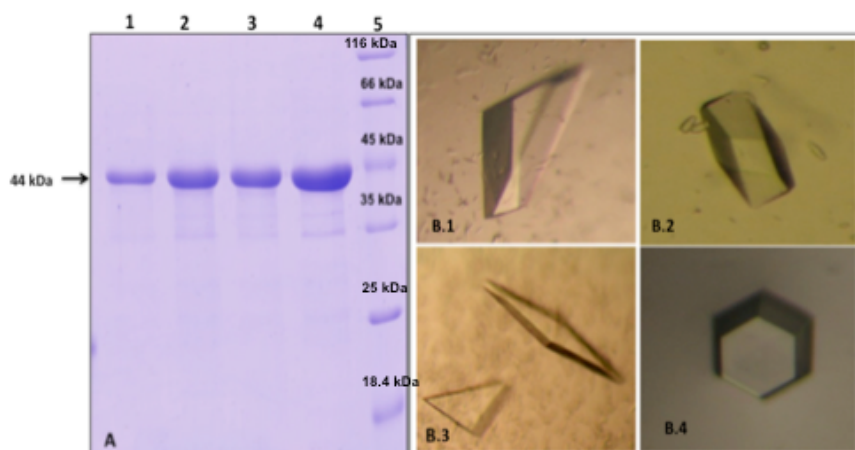
**Figure 4.1.2:** (A) SDS-PAGE of Rel$_{Seq}$385; Lane 1-3: Rel$_{Seq}$385 gel-filtered eluates Lane 4: Rel$_{Seq}$385 purified from Ni$^{2+}$-NTA chromatography (load for gel-filtration). Lane 5: Marker proteins with apparent molecular masses of 116 (most upper band), 66.2, 45, 35, 25, 18.4 kDa (lowest band). (B) Rel$_{Seq}$385 protein crystals grown with [1] GTP/compound (10), [2] GppNHp, [3] GppNHp – used for compound (15) soaking, [4] no substrate/product or analogs.
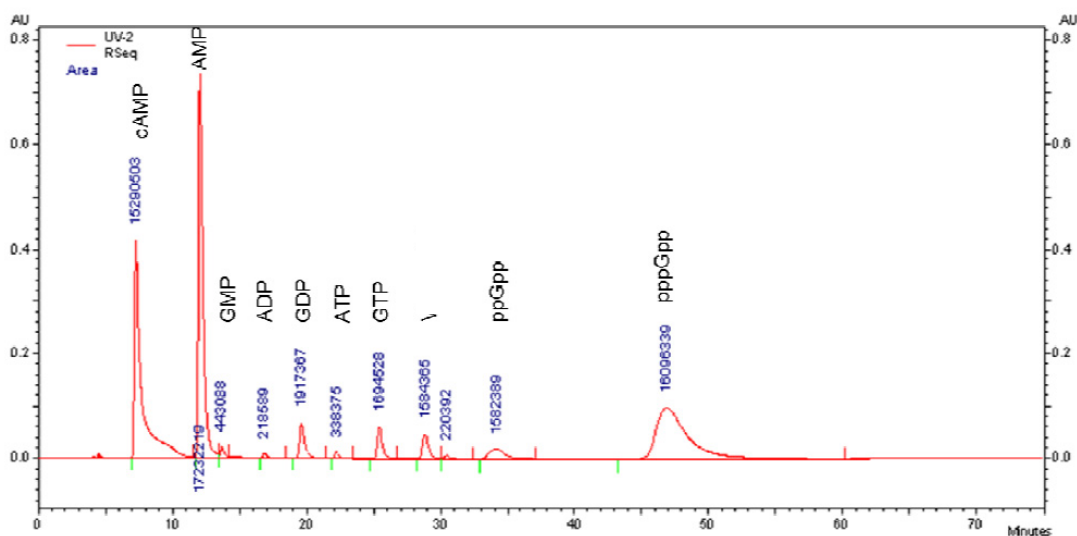


**Figure 4.1.3**: Representative chromatogram of reaction products of a Rel$_{Seq}$385 synthetase assay. Phosphorylated nucleotide substrates and products were separated by ion exchange chromatography after (p)ppGpp synthetase assay (X-axis : minutes; Y-axis shows UV absorbance at 254 nm in arbitrary units). Results (Table 4.1, see below) indicate that protein concentrations of 1 µg (12 µM) are sufficient to convert 42% of GTP in the reaction mix to pppGpp.

**Table 4.1:** Rel$_{Seq}$385 pppGpp synthetase assay

| Rel$_{Seq}$385 (μM) | pppGpp (μM) | GTP (μM) | ppGpp:GTP |
|---|---|---|---|
| 0 | 0 | 125 | 0 |
| 12 | 52.84 | 125 | 0.42 |
| 24 | 74.57 | 125 | 0.60 |
| 60 | 96.45 | 125 | 0.77 |

### 4.1.2 Crystallization of Rel$_{Seq}$385

To obtain well-diffracting crystals, the protein was mixed with an equal volume of 150 mM NaCl, 5-15 mM GTP or GppNHp, 5-15 mM ApCH$_2$pp, 5-15 mM MgCl$_2$, and 25 mM Bis-Tris propane, pH 9.0. Using the hanging-drop technique, crystals grew within 7-14 days with 22-24% PEG 8000, 500 - 800 mM NaCl, and 100 mM Tris pH 8.4 as reservoir solution at 20°C (Figure 4.1.2 B, see above). Additionally, crystals were grown or soaked in the presence of 5 to 15 mM compound (10) [Figure 4.1.9, see below] or (15) [Figure 4.1.13, see below]. The results were reproduced and optimized at the microliter-scale using sitting and hanging drop vapour-diffusion methods, with a drop composition of 2 μl protein solution and 2 μl reservoir solution, equilibrated against 1000 μl of reservoir solution in the well. The optimized crystallization condition was composed of 23% PEG 8000, 650 mM NaCl, and 100 mM Tris (pH 8.4) at 20°C, a condition similar to the published one [Hogg et al., 2004]. The crystals appeared after 7 days with dimensions ranging from approximately 400 × 300 × 300 μm$^3$ to 500 × 400 × 300 μm$^3$. Complete diffraction datasets for four different crystals grown were collected.

### 4.1.3 Structure determination and overall architecture of Rel$_{Seq}$385 complexes

Crystal structures of the bifunctional fragment of Rel$_{Seq}$385 in complex with GTP, guanosine 5'-(β,γ-imido)triphosphate (GppNHp), and with the inhibitory compounds (10) and (15) were determined by molecular replacement using the previously published structure of Rel$_{Seq}$385 (Hogg et al., 2004; PDB ID: 1VJ7) as a search model. Interestingly, crystals grown in the presence of GppNHp revealed two distinctive ligation states, which will be discussed below in detail. Crystals of all the complexes share monoclinic space group C2 with two Rel$_{Seq}$385 molecules per asymmetric unit. Data collection and refinement statistics are given in Table 4.2 (see

below). Superimposition of molecules with almost identical activity states from all available $Rel_{Seq}385$ structures confirmed that the global conformation is preserved with root-mean-square difference values for Cα atoms (Table 4.3, see below) of 0.22 - 0.41 Å (molecule 1 – Figure 4.1.4 A, see below) and 0.34 - 0.57 Å (molecule 2 – Figure 4.1.4 B, see below). The hydrolase site of molecule 1 is free of small-molecule ligands in all complexes but contains a well-defined metal ion pentacoordinated by His53, His77, Asp144, and two water molecules. In contrast, in molecule 2, the side chain of Asp78 also participates in metal ion binding, rendering it hexa-coordinated with a distorted octahedral geometry. Thus coordination of the metal ion is identical to the previously published $Rel_{Seq}385$ structure (Hogg et al., 2004) with the exception of local changes in the $Rel_{Seq}385•ppGpp/ Rel_{Seq}385•GppNHp$ complex (i.e. complex IV; Table 4.3, see below), which will be discussed below. In the literature, this metal ion has always been identified as $Mn^{2+}$, and this is how it has been described in Hogg et al. [2004]. However, experiments described later in this thesis suggest that the metal ion may actually be $Zn^{2+}$. Therefore, for the time being this metal ion is indicated as $M^{2+}$.

**Table 4.2**: Data collection and refinement statistics of Rel$_{Seq}$385 complexes.

| Rel$_{Seq}$385 complex structures | complex I | complex II | complex III | complex IV |
|---|---|---|---|---|
| **A. Data collection** | | | | |
| Beamline | I911-2, Max-lab | BL 14.2, BESSY | BL 14.2, BESSY | BL 14.2, BESSY |
| Wavelength (Å) | 1.04000 | 0.91841 | 0.91841 | 0.91841 |
| Resolution range (Å) | 36.94 - 2.70 | 42.64 - 2.47 | 35.17 - 2.55 | 31.94 - 2.15 |
| Space group | C2 | C2 | C2 | C2 |
| Unit-cell parameters | | | | |
| *a, b, c* (Å) | 173.37, 45.30, 127.75 | 173.31, 45.76, 127.29 | 174.53, 45.86, 128.19 | 174.10, 45.95, 127.58, |
| α, β, γ (°) | 90.00, 109.68, 90.00 | 90.00, 110.08, 90.00 | 90.00, 109.63, 90.00 | 90.00, 109.66, 90.00 |
| Solvent content (%, v/v) | 55 | 55 | 56 | 56 |
| Unique reflections | 24903 | 32633 | 26617 | 47212 |
| Multiplicity | 3.5 (3.4) | 4.1 (3.9) | 3.3 (3.2) | 2.0 (1.9) |
| Completeness (%) | 99.8 (99.7) | 93.5 (92.3) | 91.5 (93.5) | 95.4 (96.0) |
| $R_{merge}$[a] (%) | 6.1 (40.9) | 5.0 (52.5) | 6.1 (47.4) | 5.4 (49.3) |
| $R_{pim}$[b] (%) | 4.0 (35.3) | 3.1 (32.0) | 4.5 (30.3) | 4.2 (54.6) |
| I/σ(I) | 4.4 (2.2) | 13.2 (2.3) | 7.5 (2.0) | 7.3 (1.4) |
| **B. Refinement** | | | | |
| $R_{cryst}$[c] | 21.7 | 22.6 | 21.3 | 22.9 |
| $R_{free}$[c] | 27.8 | 28.2 | 28.2 | 28.5 |
| r.m.s.d. from ideal geometry | | | | |
| Bond lengths (Å) | 0.011 | 0.014 | 0.012 | 0.018 |
| Bond angles (°) | 1.507 | 1.647 | 1.671 | 1.834 |
| No. of refined atoms | 5321 | 5260 | 5313 | 5541 |
| Average B-factor (Å$^2$) | 62.49 | 56.02 | 65.09 | 48.59 |
| Ramachandran Plot | | | | |
| Most favored (%) | 94.0 | 95.8 | 94.0 | 96.2 |
| Additionally/generously allowed (%) | 5.5 | 4.0 | 5.5 | 3.6 |
| Disallowed (%) | 0.5 | 0.2 | 0.5 | 0.2 |

Values in parentheses correspond to the highest resolution shell.

[a]$R_{merge} = \Sigma_{hkl}\Sigma_i |I(hkl)_i - <I(hkl)>| / \Sigma_{hkl} \Sigma_i I(hkl)_i$, where $I(hkl)$ is the intensity of reflection *hkl* and $<I(hkl)>$ is the average intensity over all equivalent reflections.
[b]$R_{pim}$ is the precision-indicating merging *R* factor [Weiss and Hilgenfeld, 1997].
[c]$R_{cryst} = \Sigma_{hkl} |F_o(hkl) - F_c(hkl)| / \Sigma|F_o(hkl)|$. $R_{free}$ was calculated for a test set of reflections (5%) omitted from the refinement.

**Table 4.3:** The root-mean-square distances (Å) chart for Cα atoms between molecule 1 and molecule 2 of all Rel$_{Seq}$385 complexes

| | 1vj7 chA | Compound (10) •GTP 1 chA | Compound (15) chA | ppGpp• GppNHp chA | 3X-GppNHp chA | 1vj7 chB | Compound (10) •GTP 1 chB | Compound (15) chB | ppGpp• GppNHp chB | 3x-GppNHp chB |
|---|---|---|---|---|---|---|---|---|---|---|
| 1vj7 chainA | 0 | 0.409 | 0.262 | 0.298 | 0.22 | 1.335 | 1.296 | 1.305 | 1.314 | 1.29 |
| Compound (10) •GTP 1 chA | 0.409 | 0 | 0.365 | 0.398 | 0.369 | 1.222 | 1.18 | 1.214 | 1.237 | 1.190 |
| Compound (15) chA | 0.262 | 0.365 | 0 | 0.28 | 0.224 | 1.305 | 1.282 | 1.289 | 1.313 | 1.294 |
| ppGpp• GppNHp chA | 0.298 | 0.398 | 0.28 | 0 | 0.226 | 1.35 | 1.289 | 1.314 | 1.334 | 1.288 |
| 3X-GppNHp chA | 0.22 | 0.369 | 0.224 | 0.226 | 0 | 1.316 | 1.287 | 1.303 | 1.324 | 1.287 |
| 1vj7 chB | 1.335 | 1.222 | 1.305 | 1.350 | 1.316 | 0 | 0.572 | 0.511 | 0.511 | 0.447 |
| Compound (10) •GTP 1 chB | 1.296 | 1.18 | 1.282 | 1.289 | 1.287 | 0.572 | 0 | 0.542 | 0.444 | 0.431 |
| Compound (15) chA | 1.305 | 1.214 | 1.289 | 1.314 | 1.303 | 0.511 | 0.542 | 0 | 0.453 | 0.473 |
| ppGpp• GppNHp chB | 1.314 | 1.237 | 1.313 | 1.334 | 1.324 | 0.511 | 0.444 | 0.453 | 0 | 0.341 |
| 3x-GppNHp chB | 1.29 | 1.190 | 1.294 | 1.288 | 1.287 | 0.447 | 0.431 | 0.473 | 0.341 | 0 |

In all the complexes, well-defined electron densities that could not be accounted for by protein residues were found at the synthetase sites and/or hydrolase sites. Bound ligands could be unambiguously identified using $2F_o$-$F_c$ and simulated-annealing omit maps and were fitted into the respective electron densities. The structural data indicate that GppNHp preferably binds to the synthetase site, both in the ON and the OFF conformation (see below for Table 4.4 for an overview of all available Rel$_{Seq}$385 complexes and respective ligation states). However, at high concentrations, GppNHp can also bind to the hydrolase-ON site as indicated by a well-defined electron density in close proximity to the metal-coordination site in molecule 2 in one of the GppNHp complexes (complex IV). As expected from substrate competition and molecular docking experiments (Wexselblatt et al., 2010), compound (10) was found to occupy the synthetase-ON site, with a GTP molecule binding to the synthetase-OFF site. Likewise, compound (15) binds to the synthetase-ON site. Details of the binding mode of all ligands are described below.

**Table 4.4:** An overview of the ligands in Rel$_{Seq}$385 complexes

| Complex No. | Rel$_{Seq}$385 complexes | Molecule 1 | | Molecule 2 | |
|---|---|---|---|---|---|
| | | S –ON site | H-OFF site | S –OFF site | H-ON site |
| I | Rel$_{Seq}$385•compound (10) / Rel$_{Seq}$385•GTP | compound (10) | - | GTP | - |
| II | Rel$_{Seq}$385•compound (15) / Rel$_{Seq}$385•¥ | compound (15) | - | ¥[a] | - |
| III | Rel$_{Seq}$385•ppGpp/ Rel$_{Seq}$385•GppNHp | ppGpp | - | GppNHp | - |
| IV | Rel$_{Seq}$385•GppNHp/ Rel$_{Seq}$385•GppNHp•GppNHp (or 3x-GppNHp[b]) | GppNHp | - | GppNHp | GppNHp |
| V | 1VJ7 (or Rel$_{Seq}$385•GDP/ Rel$_{Seq}$385•GDP•ppG2':3'p) | GDP | - | GDP | ppG2':3'p |

[a] unmodeled ligand due to spurious density at the synthetase-OFF site of molecule 2 complex II.

[b] 3 molecules of GppNHp found in the asymmetric unit of Rel$_{Seq}$38(complex IV).
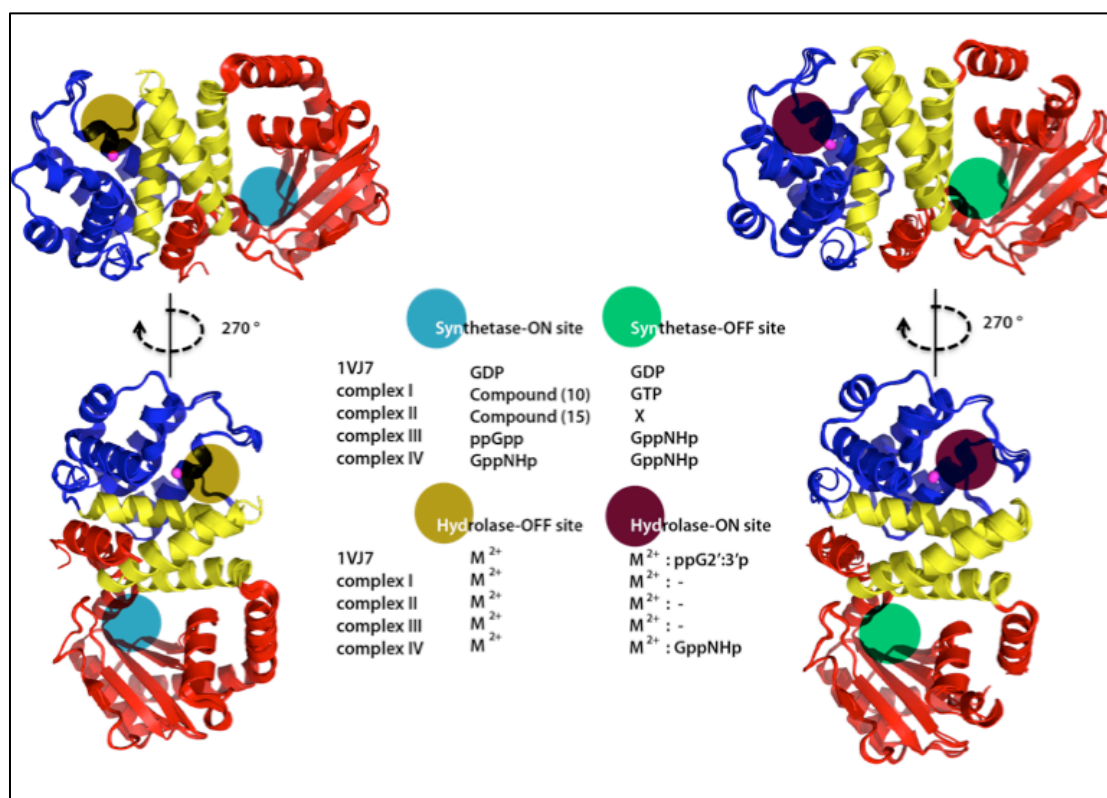
**Figure 4.1.4:** Crystal structures of $Rel_{Seq}385$ complexes superimposed onto 1VJ7. Synthetase domain (red), central 3-helix bundle [C3HB] (yellow), and hydrolase domain (blue), metal ions (pink sphere). Colored circles indicate the respective nucleotide- or analog-binding sites as listed. **(A)** Overall superimposition of molecule 1 showing synthetase-ON/hydrolase-OFF conformers of $Rel_{Seq}385$ complexes with 1VJ7 chain A. **(B)** Overall superimposition of molecule 2 synthetase-OFF/hydrolase-ON conformers of $Rel_{Seq}385$ complexes with 1VJ7 chain B.

### 4.1.4 Substrate-bound states of the $Rel_{Seq}385$ synthetase domain

The $Rel_{Seq}385$ complexes with GTP and GppNHp presented in this study display the enzyme in a substrate-bound state before pyrophosphate transfer to the 3'-OH group of GTP. GTP or GppNHp are binding to the synthetase-ON as well as to the synthetase-OFF state of $Rel_{Seq}385$. In all cases, the guanine moiety stacks against the phenolic ring of the highly conserved Tyr308 located at the bottom of a well-defined binding pocket (Site 1, see Figure 4.1.5). Apart from this $\pi$-$\pi$-interaction, guanine-base recognition involves hydrogen bonds with Ser181, Lys304, Asn306, and/or Ala335. The 2'-OH group of the ribose in GTP forms hydrogen bonds with the side-

chains of Gln325 and Arg269, whereas in complexes with GppNHp or GDP (Hogg et al., 2004), these interactions are missing. The 5' triphosphate or 5' (β,γ-imido) triphosphate moieties of GTP or GppNHp are oriented towards a strongly positively charged shallow interaction site (Site 3) open to bulk solvent. Slightly different conformations of the 5'-phosphates in the four complexes might reflect alternative binding modes of substrate molecules. Interestingly, the observed alternative binding modes do not correspond to different activation states of the Rel$_{Seq}$385 synthetase site. Multiple conformations of the tri-phosphate moieties are supported by the large interaction surface of Site 3 providing suitable protein side-chains to enable hydrogen bonds (Tyr299 and His312) and electrostatic interactions (Arg295, Lys297, and Lys304). Thus, in general the binding mode of GTP or GppNHp is similar to that of GDP (Hogg et al., 2004) with both 5'-di- and tri-phosphates being able to adopt multiple conformations within Site 3 (Figure 4.1.5, see below). This is acceptable as the 5'-moieties are not directly involved in pyrophosphate transfer to the 3'-OH of the substrate.
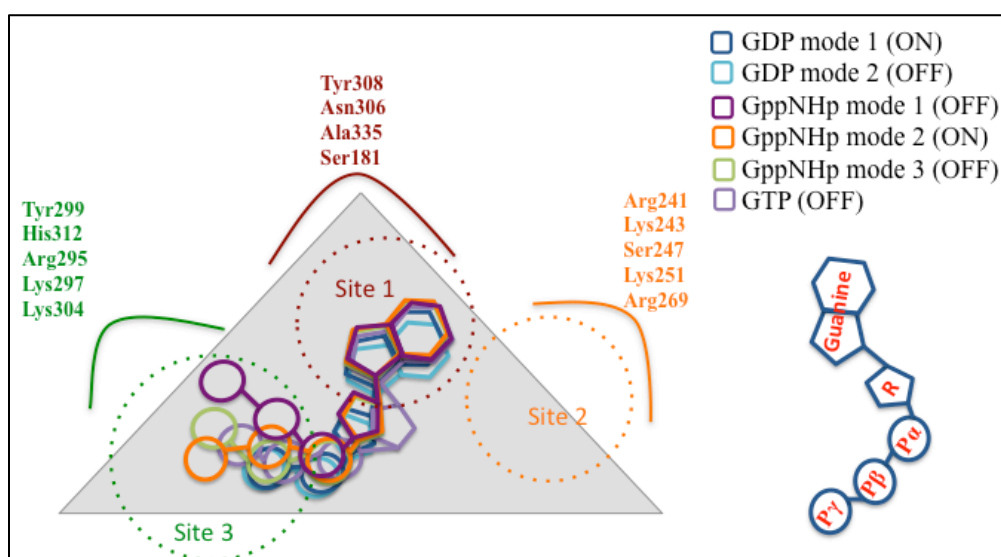


**Figure 4.1.5:** Schematic overview of preferred binding states for GDP, GTP, and GppNHp in the synthetase- ON and OFF sites of Rel$_{Seq}$385 (gray triangle), based on the binding modes observed in four different complexes. Site 1 (red circle) represents the site specific for the guanine moiety. Site 3 (green circle) – strongly positively charged shallow interaction site for the 5' diphosphate of GDP or the 5' (β,γ-imido) triphosphate of GppNHp or the 5' triphosphate of GTP. Site 2 (orange circle) - a deep, positively charged subsite next to Site 1. (R - ribose)

Thus, the structures of Rel$_{Seq}$385 in complex with triphosphate substrates reveal the alternative binding modes of the acceptor substrate of the reaction. The binding modes of the triphosphate substrates do not correlate with the activation states of Rel$_{Seq}$385.

**4.1.5 Product and their analogs in complex with the Rel$_{Seq}$385 synthetase**

**4.1.5.1 The ppGpp-bound Rel$_{Seq}$385 synthetase domain**

Surprisingly, one of the complexes (complex III) obtained from a co-crystallization experiment in the presence of GppNHp showed an unexpected, continuous electron density at the 3'-OH of the ribose moiety. This density was present in the synthetase-ON site but missing in the synthetase-OFF site of Rel$_{Seq}$385 as confirmed by simulated-annealing omit map calculations (Figure 4.1.7 A, see below). Subsequently, the bound ligand was unambiguously identified by analyzing dissolved crystals using matrix-assisted laser desorption/ionization (MALDI) and electrospray ionization (ESI) mass spectrometry (see Appendix - 6.5 & 6.6) [Potier et al., 2000]. The electron density corresponds very well to ppGpp (Fig. 4.1.6), the product of the reaction catalyzed by Rel$_{Seq}$. Indeed, a model of ppGpp could be easily fitted to the initial electron density, which further improved after a few additional rounds of crystallographic refinement. It can be assumed that ppGpp from *E. coli* was initially co-purified with Rel$_{Seq}$385 as no suitable pyrophosphate donor substrate (such as ATP) was present during purification or crystallization of the protein. For example, co-purified ppGpp was unexpectedly observed from the crystalline Obg GTPase [Buglino et al., 2002] and the acid shock-regulator enzyme lysine decarboxylase LdcI [Kanjee et al., 2011]. Also, the interrelationships of the afore-mentioned enzymes with the stringent response were deduced from the unexpected binding of ppGpp to the crystal structures. As expected for a reaction product in the synthetase, ppGpp was readily replaced during crystallization by ligands with higher affinity for the synthetase-ON site such as compound (10) or (15), (depending on the crystallization condition) or GppNHp. The binding mode of ppGpp closely resembles that of GDP with the additional 3'-diphosphate located in a deep, positively charged subsite (Site 2) next to Site 1 (Figure 4.1.7 B, see below). This interaction is stabilized by hydrogen-bonding and polar contacts between the 3'-phosphates and Arg241, Lys243, Ser247, Lys251, and Arg269, i.e. with the walls of Site 2. This strongly supports the

previous suggestion that these residues also act as initial interaction partners for the β- and γ-phosphate groups of the donor substrate ATP prior to pyrophosphate transfer (Hogg et al., 2004). However, in the absence of ATP or (p)ppGpp, Site 2 exhibits a certain degree of flexibility mainly due to conformational rearrangements among residues 240 - 244 of loop β3/α13. Arg241 shows differences in the position of its Cα atom of up to 1.5 Å when comparing different $Rel_{Seq}385$ structures. Interestingly, the observed conformations of loop β3/α13 of the synthetase domain do not concur with the ON or OFF state.
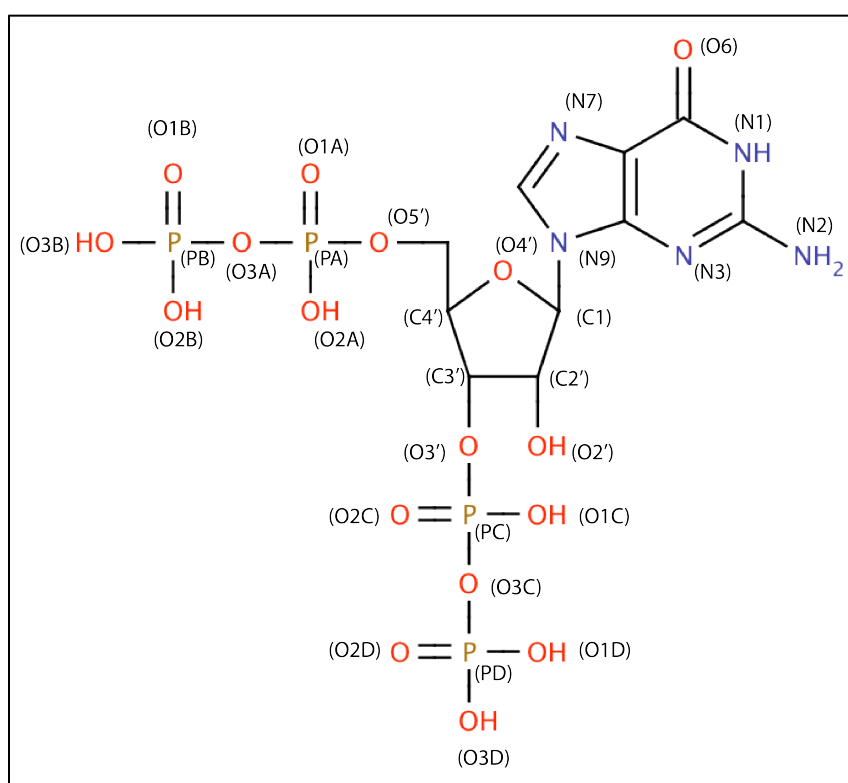


**Figure 4.1.6:** Chemical structure of ppGpp with atom names in parentheses

Thus, the structures of $Rel_{Seq}385$ in complex with GTP and ppGpp do not only reveal the precise binding modes of substrate and product of the (p)ppGpp synthesis reaction, but also uncover a surprising plasticity of the synthetase and hydrolase active site that seems to be independent of interdomain crosstalk.
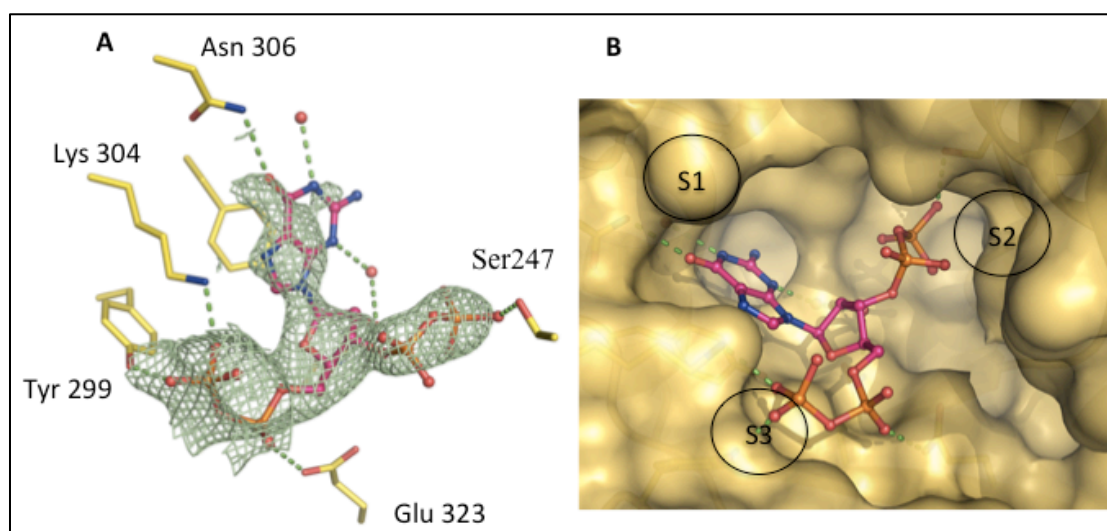
**Figure 4.1.7:** ppGpp binding mode in $Rel_{Seq}385$ (complex III): **A)** ppGpp as balls & sticks, modeled into the simulated-annealing omit map (green, $2F_o$-$F_c$ contoured at $1\sigma$ above the mean) and the interacting residues are shown as sticks of the synthetase-ON site. **B)** Surface representation of the synthetase active site (S1 – Site 1; S2 – Site 2, S3 - Site 3) with ppGpp shown as balls & sticks; atoms coloured as follows: carbon - pink, oxygen - red, nitrogen - blue, phosphorus – orange.

### 4.1.5.2 Product analog: compound (10)

Recently, the synthesis and characterization of ppGpp analogs of Rel proteins have been reported (Wexselblatt et al., 2010). *In-silico* docking and competition assays suggest that compound (10) blocks the activity of Rel proteins by competing with substrate (Wexselblatt et al., 2010). Compound (10) mimics ppGpp and differs from it by two features, non-hydrolyzable methylene-bisphosphonate groups at the 5' and 3' positions and a 2'-deoxyribose sugar moiety (Figure 4.1.8, see below). The binding modes of compound (10) will be discussed below in detail.

69
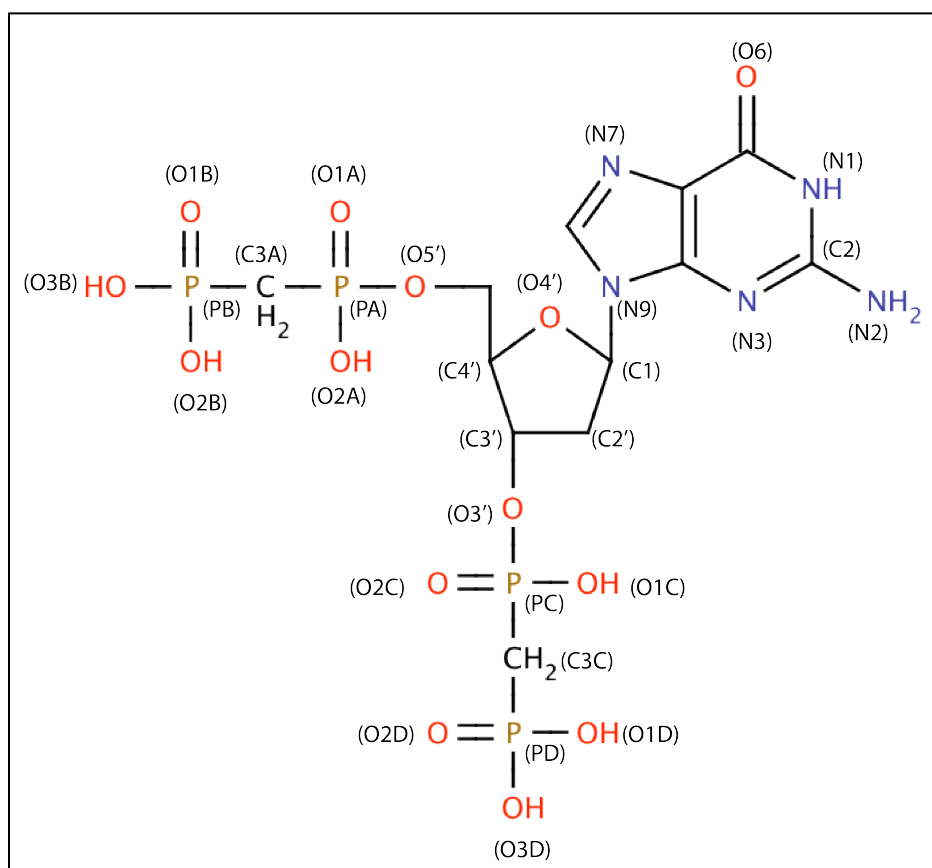
**Figure 4.1.8:** Chemical structure of compound (10) with atom names in parentheses

### 4.1.5.2.1 Binding mode of compound (10)
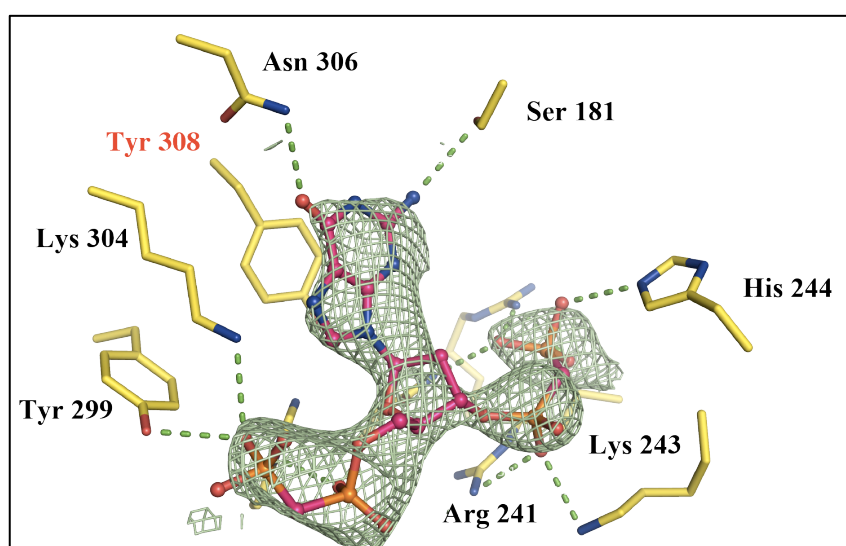


**Figure 4.1.9:** Compound (10) binding mode: Compound (10) as balls & sticks, modeled into the simulated-annealing omit map (2F$_o$-F$_c$ map in green contoured at 1σ above the mean) and interacting residues as sticks of the synthetase-ON binding pocket.

Modeling of compound (10) into the density (Figure 4.1.9, see above) in the synthetase-ON pocket revealed the positions and orientations of the key residues involved in the ligand interactions. The 5'-bisphosphonate of compound (10) adopts a similar conformation as the 5'-diphosphate of GDP in the crystal structure of Rel$_{Seq}$385 [Hogg et al., 2004]. The 3' moiety of compound (10) binds to a deep, well-defined pocket of strong positive charge (Site 2) present only in the synthesis-ON conformation of Rel$_{Seq}$385 (Figure 4.1.10, see below). Although the binding of compound (10) does not lead to major structural changes in the synthetase active-site region, considerable local changes such as side-chain rearrangements were visible. Guanine-base recognition involves hydrogen bonds with Lys304, Ala335, and Asn306. The surrounding residues envelope compound (10) forming an extensive hydrogen-bonded network and electrostatic interactions. Tyr299-O$\eta$ makes a 3.1-Å hydrogen bond to the O2B at the distal 5' end of compound (10). The 3' phosphonate oxygen moieties are involved in H-bonds. Lys243-N$\varsigma$ donates a hydrogen bond to O2A with a distance of 2.5 Å, whereas Arg269-N$\eta$2 forms a salt-bridge with O1D (2.6 Å) and O2D (2.9 Å). Remarkably, Arg269 is oriented away from the binding site providing ample space for the 3' end of compound (10) to be accommodated. The amide group (N$\varepsilon$2) of Gln325 makes a 2.9 Å hydrogen bond (Figure 4.1.11, see below).
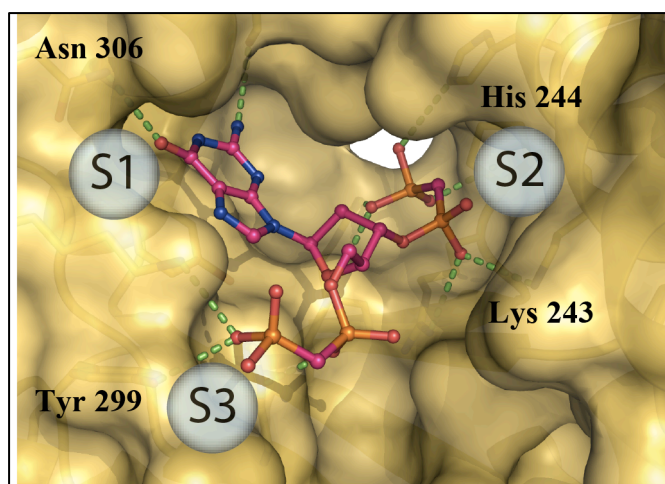


**Figure 4.1.10:** Surface representation of the interactions between compound (10) and Rel$_{Seq}$385; compound (10) as balls & sticks bound to synthetase-ON active site pocket.
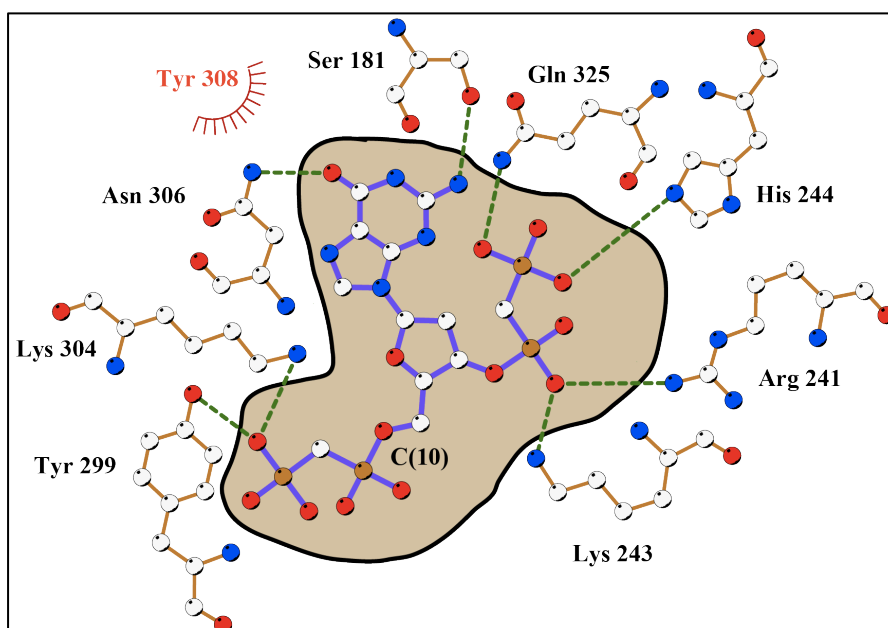
**Figure 4.1.11:** 2-D representation of the interactions between compound (10) and $Rel_{Seq}385$. Hydrogen bonds shown as dotted green lines, van-der-Waals interactions as red half-circles.

### 4.1.5.2.2 Comparisons with prediction and GDP-bound $Rel_{Seq}385$

Earlier prediction of compound (10) binding suggested that this compound could have less affinity for the synthetase active site in the OFF conformation than the ON conformation (Wexselblatt et al., 2010). Supporting this view, the crystal structure of compound (10) complex rationalizes affinity towards the synthetase active site in its ON conformation. The only difference between the crystal structure and the prediction is the glycosidic bond between the guanine ring and the associated deoxyribose moiety of compound (10), as it differs by a rotation of approximately 180°. The positioning of the 5' moiety of compound (10) is similar to the 5' moiety of GDP of the published structure (Hogg et al., 2004). A superimposition wit the GDP synthetase-ON form (root-mean-square deviation: 0.41 Å) revealed the rearrangement of loop β3/α13 residues Arg241-His244 in the compound (10) complex. The binding of compound (10) to the active site pocket of the synthetase-ON conformer reveals a surprising plasticity of the loop β3/α13. Arg241 and Lys243 are highly conserved residues in bifunctional Rel enzymes. The loop moves inward and participates in the interaction network of compound (10) binding. This leads to local conformational changes of Pro242 (shift of the Cα atom: 1.9 Å) and the side-chain of Arg241 (shift of

the Cα atom: 1.1 Å). In this conformation, Arg241 is oriented towards Glu323, thereby enabling the Site 2 pocket that accommodates the 3' - methylene bisphosphonate moiety of compound (10) (depicted in surface representation in Figure 4.1.10, see above). Moreover, the catalytic loop region (α13/β4) containing Ala267 (shift of the Cα atom: 0.9 Å) rearranges to fit the bound compound (10). However, one of the key residues involved in the catalytic event, Asp264, retained its typical "IN" conformation (see section 1.2.7.1).

### 4.1.5.3 Product analog: compound (15)

Based on the class of compound (10) and its effects on $Rel_{Seq}385$, a similar compound named "15" was synthesized and tested (Wexselblatt, unpublished data) and co-crystallized with $Rel_{Seq}385$. Compound (15), being a non-hydrolyzable ppGpp analog, differs from compound (10) by the substitution of 3' and 5' with methyl acetate phosphonate moieties (Figure 4.1.12). Overall, the binding modes of compound (10) and compound (15) share a high degree of similarity to the ppGpp-bound form. The binding modes of compound (15) will be discussed below in detail.
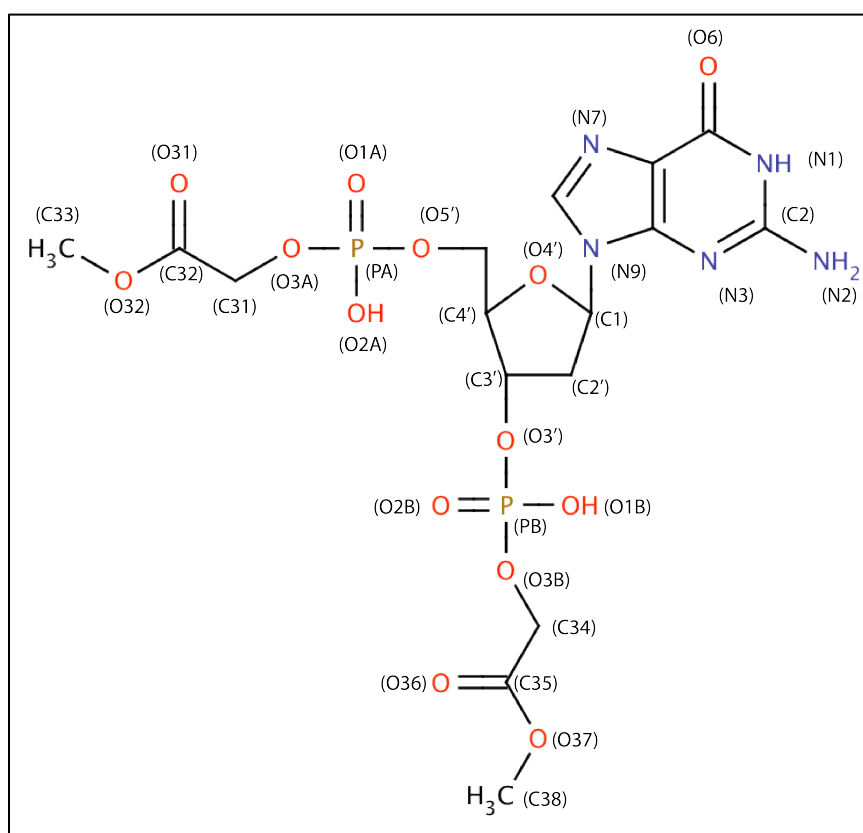


**Figure 4.1.12:** Chemical structure of compound (15) with atom names in parentheses

73

### 4.1.5.3.1 Binding mode of compound (15)
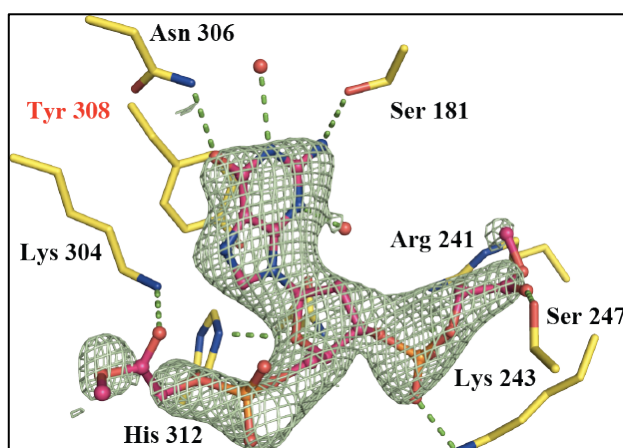


**Figure 4.1.13:** compound (15) binding mode: compound (15) as balls & sticks representation, modeled into the simulated annealing omit map ($2F_o$-$F_c$ map in green contoured at $1\sigma$ above the mean) and the interacting residues as sticks of the synthetase-ON binding pocket.

Fitting compound (15) into the density (Figure 4.1.13, see above) at the synthetase-ON pocket revealed the position and orientation of the key residues involved in the ligand interactions. The 3' methyl ester of compound (15) binds to the deep, well-defined Site 2 pocket (Figure 4.1.14, see below). Enveloping residues around compound (15) form an extensive hydrogen-bonded network and electrostatic interactions; the recognition involves H-bonds from Lys243-N$\varsigma$ to O2B at a distance of 2.72 Å and from Arg241-N$\eta$1 to O1B and O37 at distances of 2.95 Å and 2.75 Å, respectively. The O32 atom hydrogen bonds with Lys304-N$\varsigma$ at a distance of 2.72 Å. Ser247-O$\gamma$ and the backbone amide of His244 donate hydrogen bonds to phosphate oxygen O36. Other recognition involves H-bonds from Gln325-N$\varepsilon$2 to O3', from Asn306-N$\delta$2 to O6, and from Lys304-N$\varsigma$ to O32 (Figure 4.1.15, see below). Although the synthetase-OFF pocket of the crystal structure displays ambiguous density for a guanine-like moiety, the site is left unmodeled due to considerable disorder in the proximal catalytic loop residues.

74
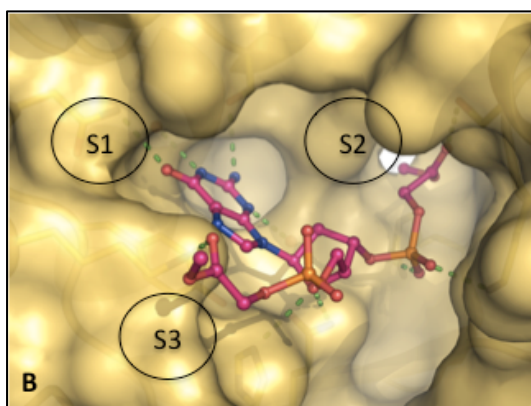
**Figure 4.1.14:** Surface representation of the compound (15) complex, in which the compound is shown as balls & sticks representation bound to the well-defined synthetase-ON active-site pocket.
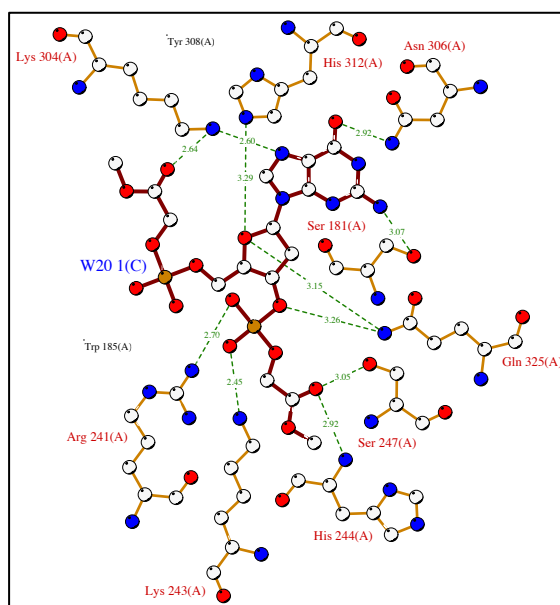


**Figure 4.1.15:** 2-D representation of the interactions between compound (15) and $Rel_{Seq}385$. Hydrogen bonds shown as dotted green lines, van-der-Waals interactions as red half-circles.

### 4.1.5.3.2 Comparison of the complexes with GDP, compound (15), and compound (10)

Despite the geometries of guanine-base and deoxyribose sugar recognition being nearly the same in all the complexes, considerable differences in the interacting network at the 3' and the 5' substituents of compound (10) and (15) are apparent. A

close inspection of the ligands during superimposition of $Rel_{Seq}385\bullet$compound (15) [complex II] and $Rel_{Seq}385\bullet$compound (10) [complex I] reveal that apart from nucleoside parts, the 5'-P$\alpha$ atoms of compound (10) and (15) shift by ~2.7 Å and 3'-P$\alpha$ atoms by ~1.0 Å. A similar inspection with $Rel_{Seq}385\bullet$GDP [1VJ7 chain A] revealed that 5'-P$\alpha$ of GDP from compound (10) shifts by ~1.0 Å and compound (15) by ~2.2 Å. Also, C5' of GDP from compound (10) shifts by ~2.5 Å and compound (15) by ~2.6 Å. The 3'-substituents of compound (15) or (10) binds to the deep, well-defined Site 2 near the Site 1 pocket. Unlike the 5'-methylene phosphonate of compound (10), the 5'-methyl ester group of compound (15) orients away from Site 3 into the bulk solvent. Comparison between molecule 2 of complex I, molecule 2 of complex II, and molecule 2 of the GDP complex [1VJ7 chain B] reveals the drastic rearrangement and the disintegration in the structural elements comprising loop $\beta3/\alpha13$, the catalytic loop, and part of $\beta4$. Residues 254 – 267 are completely disordered.

An overall comparison chart of the selective distances (hydrogen bonds) between the ligands and the synthetase-site residues and the torsion angles of the nucleotide and analogs of the complexes as observed are listed in the Appendix (sections 6.7, 6.8, and 6.9).

### 4.1.6 The product-bound state of the $Rel_{Seq}385$ hydrolase

3x-GppNHp crystal (complex IV) was obtained from co-crystallization of $Rel_{Seq}385$ with GppNHp. The synthetase active sites of both the monomers displayed well-defined densities for GppNHp. The mode of interaction of GppNHp in the synthetase-ON conformer displays distinctive characteristics at the imidophosphate moiety (Figure 4.1.16 A), whereas the binding mode of GppNHp at the synthetase-OFF conformer matches the GDP binding mode to the synthetase-OFF conformer of the published structure (Figure 4.1.16 B, see below). After a few iterative refinement steps, the hydrolase-ON conformer also displayed a clear density for GppNHp. The fit of a GppNHp molecule in the density is comparable to the published ppG2':3'p complex (Figure 4.1.17 A & B, see below). GppNHp mimics the product of the pppGpp hydrolysis reaction. An overall superimposition of complex IV molecule 2 with the $Rel_{Seq}385\bullet$ppG2':3'p monomer complex (1VJ7 chain B) gives a C$\alpha$ rms deviation of 0.30 Å over a 309-residue core. The segment Thr151 to Leu155 display a

high degree of disorder. The 5' imidophosphate group of GppNHp is widely exposed to bulk solvent.
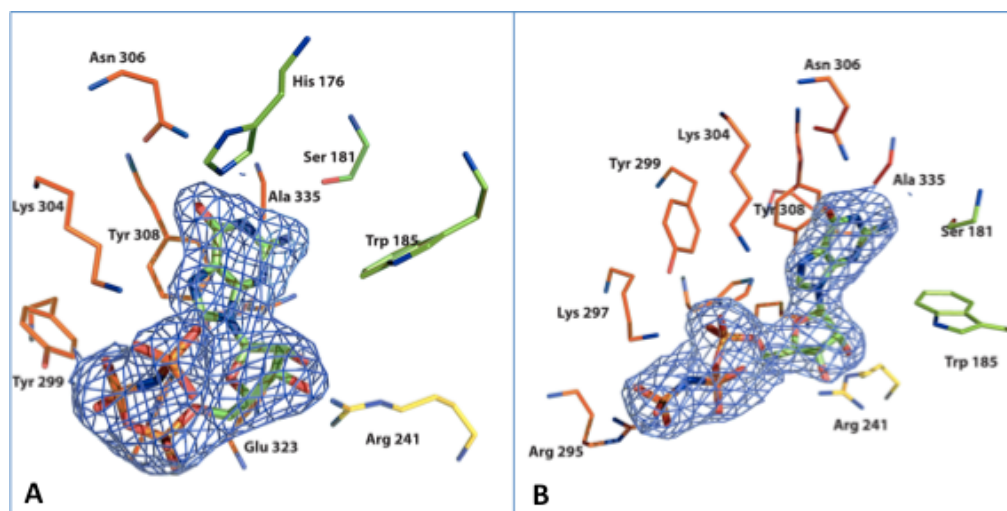


**Figure 4.1.16:** Binding modes of GppNHp in 3x-GppNHp (complex IV). (**A**) Modeled GppNHp in the electron-density map (2F$_o$-F$_c$ map in blue, contoured at 1σ above the mean) at the synthetase-ON conformer. (**B**) Modeled GppNHp in the electron-density map (2F$_o$-F$_c$ map in blue, contoured at 1σ above the mean) at the synthetase-OFF conformer.
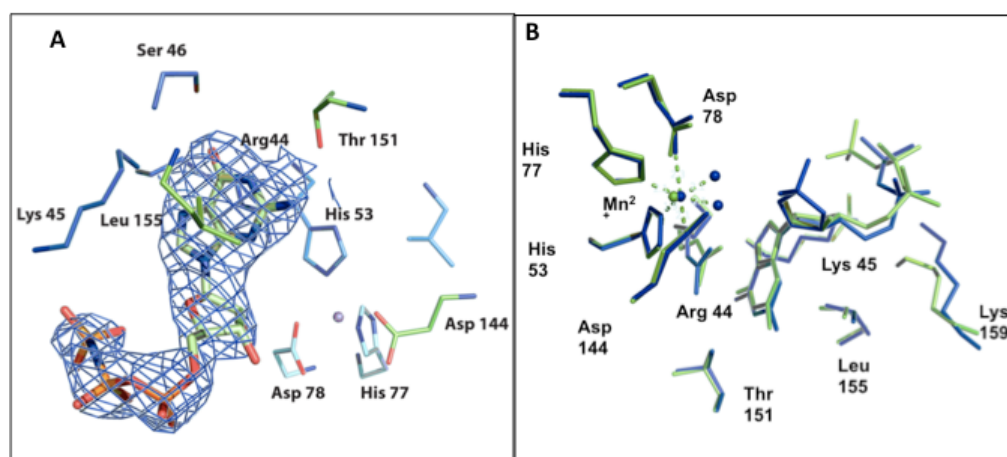


**Figure 4.1.17**: Binding modes of GppNHp to the hydrolase active site of 3x-GppNHp (complex IV). (A) Modeled GppNHp in the electron-density map (2F$_o$-F$_c$ map in blue, contoured at 1σ above the mean) at the hydrolase-ON binding pocket. (B) Stick/ spheres representation of superimposed structures of hydrolase-ON binding sites - ppG2':3'p from the published structure (blue), GppNHp from 3x-GppNHp (green).

### 4.1.7 Conformational states of the synthetase- and the hydrolase- domains of the Rel$_{Seq}$385 complexes

In order to get a better understanding of the reciprocal activity states [(p)ppGpp hydrolase-ON/synthetase-OFF and (p)ppGpp hydrolase-OFF/synthetase-ON; PDB ID: 1VJ7; Hogg et al., 2004], the domains hydrolase and synthetase from each monomer of the Rel$_{Seq}$385 complexes and their ON and OFF states were compared in detail.

### 4.1.7.1 Hydrolase- ON and OFF states

The reciprocal activity states of molecule 2 of 1VJ7 (i.e., chain B) are defined as hydrolase-ON/synthetase-OFF. Close comparisons through superimposition of 1VJ7 molecule 2 with Rel$_{Seq}$385 complexes analyzed in this work reveal intriguing observations for the hydrolase- ON and OFF states, particularly, molecule 2 of complex III (Rel$_{Seq}$385•ppGpp/ Rel$_{Seq}$385•GppNHp). Unlike all other copies of molecule 2 of the Rel$_{Seq}$385 complexes, complex III displays discrepancies in the reciprocal activity states through considerable local changes. M$^{2+}$ is hexacoordinated (His53, His77, Asp78, Asp144, and two water molecules) in a distorted octahedral arrangement, Asp78 from the inner M$^{2+}$-coordination sphere is oriented away by approximately 0.75 Å from the position in other complexes. Also, the critical residue Arg44 loses its interdomain contact with Asn148 and Thr151, and forms salt-bridge with Asp78 (Figure 4.1.18). These rearrangements suggest that the M$^{2+}$ coordination is in transition between 6-fold and 5-fold. Additionally, the α8-α9' loop (residues 154 – 159) alongwith the first turn of the α9'/α9″ of the central 3-helix bundle is disordered, and local conformational changes in residues 40-50 including β1/β2 hairpin are visible. Most of these changes are characteristic features for a hydrolase-OFF state previously observed by Hogg et al. [2004]. Although no global conformational changes occurred, these striking dissimilarities in the hydrolase domain of the complex III compared to the other complexes point a way towards understanding the transition between hydrolase-ON and OFF. Hence, a list of local displacements and disorder between key residues, and the structural elements were analyzed (Table 4.5). Another intriguing observation is the presence of the product-mimic GppNHp molecule in the hydrolase domain of molecule 1 of complex IV

(section 4.1.6, see above). However, the presence of this ligand does not alter the hydrolase-ON state of the monomer.
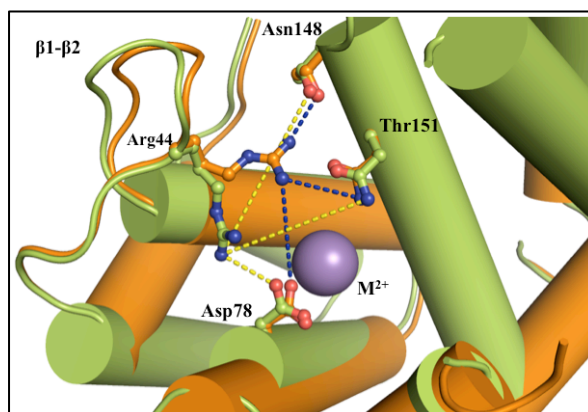


**Figure 4.1.18**: A superimposition of the crystal structures of complex III molecule 2 (green) and 1VJ7 molecule 2 (orange), showing the differences in the hydrolase site. The residues are shown as balls & sticks; contacts between residues are shown as dotted-lines (yellow – complex III molecule 2; blue – 1VJ7 molecule 2); gray sphere – $M^{2+}$.

**Table 4.5:** List of local displacements and disorder between key residues, and structural elements in the hydrolase domain of all $Rel_{Seq}385$ complexes.

| $Rel_{Seq}385$ complex | $M^{2+}$ coordination | | α8-α9' loop | | Asp78-Arg44 (salt-bridge formation) | | Arg44-Thr151 (distance in Å) | | Arg44-Asn148 (distance in Å) | |
|---|---|---|---|---|---|---|---|---|---|---|
| | M 2 | M 1 | M 2 | M 1 | M 2 | M 1 | M 2 | M 1 | M 2 | M 1 |
| complex I | 6-fold | 5-fold | Y | X | no | yes | 2.9 | 10.4 | 2.7 | 7.6 |
| complex II | 6-fold | 5-fold | Y | X | no | yes | 3.6 | 9.9 | 2.8 | 8.0 |
| complex III | **6- to 5-fold** | 5-fold | **X** | X | **yes** | yes | **9.9** | 10.5 | **7.6** | 7.7 |
| complex IV | 6-fold | 5-fold | Y | X | no | yes | 3.2 | 10.5 | 2.6 | 7.8 |
| 1VJ7 | 6-fold | 5-fold | Y | X | no | yes | 2.9 | 10.5 | 2.9 | 7.7 |

(M 2 – molecule 2 or chain B; M 1 – molecule 1 or chain A; X – segment disordered; Y- segment defined).

A list of changes in parameters (Table 4.5, see above) such as $M^{2+}$ coordination, the α8-α9' loop within the C3HB, the formation of a salt-bridge between Asp78 and Arg44, the distances between Arg44 and Asn148 or Thr151 were chosen as the characteristic features for signifying the hydrolase-ON and OFF states. These parameters suggest that molecule 2 of complex III is not truly hydrolase-OFF, but rather in a transition between hydrolase-OFF and -ON.

**4.1.7.2 Synthetase- ON and OFF states**

In case of molecule 1 of 1VJ7 (i.e., chain A), the reciprocal activity states are defined as hydrolase-OFF/synthetase-ON. Comparison of this monomer with its almost identical molecules 1 of other $Rel_{Seq}385$ complexes reveals key aspects for synthetase- ON and OFF states. A set of key parameters signifying synthetase-ON and -OFF states in all complexes is listed in Table 4.6. Although molecule 1 of complex III displays Asp264 in its typical "IN" conformation alongside Glu323 [Hogg et al., 2004], a deviation in the distance between Asp264 and Glu323 (7.9 Å) from the rest of the complexes (approximately 4.5 Å) is observed. This is probably due to the binding of the product ppGpp and the reorientation of the side-chain of Glu323.

The β6-β7 loop (residues 315-321) is located in close proximity to the α13-β4 loop (catalytic loop) and to α11/α12 (residues 211-216). These segments (α13-β4 loop and α11/α12) are disordered in the synthetase-OFF-state monomers. Hence, the distance between Tyr316 and Pro321 present in the β6-β7 loop (~ 6Å in synthetase-ON monomers and -~10Å in synthetase-OFF monomers) reflects a considerable local conformational change of the synthetase domain. However, no deviation is observed in the β6-β7 loop upon comparisons between the identical molecules of the complexes.

In synthetase-OFF states (Hogg et al., 2004; this study), the α13-β4 loop (catalytic loop; residues 256-264), and the α11-α12 loop (residues 211-216) are disordered. In synthetase-ON states, the α13-β4 loop and the α11-α12 loop are well defined. The flexibility and disorder of these residues are considered one of the key features in determining synthetase-ON or -OFF states [Hogg et al., 2004]. Unexpectedly, the synthetase domain of molecule 2 of complex III displays discrepancies through considerable local changes in the α13-β4 loop (catalytic loop). In this molecule, the

α13-β4 loop is defined and the α11-α12 loop is disordered. An overlay showing the status of loops α13-β4 and α11-α12 from 1VJ7 and complex III molecule 2 is shown in figure 4.1.19 (A & B). These changes in the structural elements suggest that it is likely that the conformational state exhibited by molecule 2 of complex III is an intermediate between synthetase-OFF and ON. Another intriguing observation is that in all the complexes, there is an acceptor substrate or ppGpp or a ppGpp analog bound to the synthetase site.
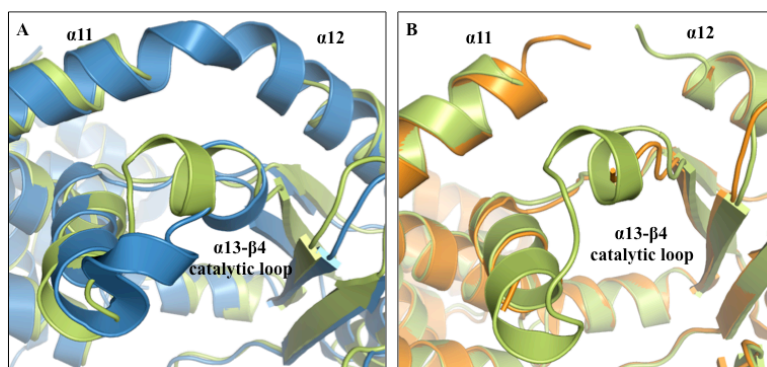


**Figure 4.1.19**: Crystal structures of $Rel_{Seq}385$ showing differences at the synthetase site. (A) Superimposition of complex III molecule 2 (green) over 1VJ7 molecule 1 (blue). (B) Superimposition of complex III molecule 2 (green) over 1VJ7 molecule 2 (orange).

**Table 4.6:** List of local displacements and disorder between key residues, and structural elements in the synthetase domain of all $Rel_{Seq}385$ complexes.

| $Rel_{Seq}385$ complex | Ligands | | α13 - β4 loop | | Asp264 – Glu323 (distance in Å) | | β6 - β7 loop Tyr316 – Pro321 (distance in Å) | |
|---|---|---|---|---|---|---|---|---|
| | M 1 | M 2 | M 1 | M 2 | M 1 | M 2 | M 1 | M 2 |
| complex I | compound (10) | GTP | Y | X | 4.3 | 12.1 | 6.7 | 10.1 |
| complex II | compound (15) | ¥ | Y | X | 4.5 | § | 6.2 | 9.8 |
| complex III | ppGpp | GppNHp | Y | **Y** | **7.9** | 14.6 | 6.6 | 9.8 |
| complex IV | GppNHp | GppNHp | Y | X | 4.3 | 14.6 | 5.9 | 10.1 |
| 1VJ7 | GDP | GDP | Y | X | 4.7 | 13.8 | 6.1 | 9.4 |

(M 1 – molecule 1 or chain B; M 2 – molecule 2 or chain A; X – segment disordered; Y- segment defined; ¥ - unmodeled ligand due to spurious density; § - Asp264 is a missing residue, due to disorder in the catalytic loop of molecule 2 of complex II)

### 4.1.7.2 Reciprocal activity states

Comparative analyses of the catalytic domains from the individual monomers of all $Rel_{Seq}385$ complexes reveals that each of the monomers displays reciprocal activity states (molecule 1: hydrolase-ON/synthetase-OFF; molecule 2: hydrolase-OFF/synthetase-ON) with the exception of complex-III molecule 2 (Table 4.7). Not only molecule 2 displays a hydrolase-ON-OFF-intermediate/synthetase-OFF-ON-intermediate state but also concurs a reciprocally regulating activity states. These dynamic conformational intermediate states are plausible, as the conformational change steps could avoid ineffective futile recycles of (p)ppGpp-synthesis and -hydrolysis.

**Table 4.7:** List of $Rel_{Seq}385$ complexes and their reciprocal activity states

| Complex No. | $Rel_{Seq}385$ complex | Reciprocal activity states | | | |
| --- | --- | --- | --- | --- | --- |
| | | Molecule 1 | | Molecule 2 | |
| | | Synthetase | Hydrolase | Synthetase | Hydrolase |
| I | $Rel_{Seq}385$•Compound (10) / $Rel_{Seq}385$•GTP | ON | OFF | OFF | ON |
| II | $Rel_{Seq}385$•Compound (15) / $Rel_{Seq}385$•¥ | ON | OFF | OFF | ON |
| III | $Rel_{Seq}385$•ppGpp/ $Rel_{Seq}385$•GppNHp | ON | OFF | **OFF→ON** | **ON→OFF** |
| IV | $Rel_{Seq}385$•GppNHp/ $Rel_{Seq}385$•GppNHp•GppNHp (or 3x-GppNHp[b]) | ON | OFF | OFF | ON |
| V | 1VJ7 (or $Rel_{Seq}385$•GDP/ $Rel_{Seq}385$•GDP•ppG2':3'p) | ON | OFF | OFF | ON |

### 4.1.8 ppGpp analogs serve as structural probes for Rel

In $Rel_{Seq}385$•ppGpp (molecule 1 of complex III), the 3' moiety of ppGpp hydrogen-bonds with the $O\gamma$ of Ser247 and weakly with the $N\eta1$ of Arg241, whereas in both the ppGpp-analog-complexes, the presence of the hydrophobic groups [compound (10) - methylene group; compound (15) - methyl acetate group] at the 3' region lead to a deviation of this interaction. The phosphate groups form hydrogen bonds and electrostatic interactions with Site-2 loop $\beta3/\alpha13$ residues. The subtle conformational

re-arrangement at Site 2 of the synthetase domain shows an alternative mode of the interactions between the product or product-analogs and the substrate or substrate-analogs. Such a conformational re-arrangement upon product or product-analog binding to the synthetase domain is significant, as it is proximal to the putative donor nucleotide-binding pocket. Moreover, it can presumably limit donor nucleotide (ATP) access to the synthetase active site. Although all available complexes lack ATP and $Mg^{2+}$, it can be assumed that the ppGpp or ppGpp-analog complexes with their interactions at Site 2 induces the synthetase domain to restore at some point after catalysis, i.e., AMP dissociation. In order to unveil more insights into the (p)ppGpp synthetase mechanism, a structural definition of a donor substrate complex is needed.

## 4.1.9 Prediction of the ternary complex of $Rel_{Seq}385 \bullet GDP \bullet ATP \bullet Mg^{2+}$

In order to synthesize (p)ppGpp, Rel enzymes should select a specific donor substrate (ATP) from the cytosolic pool to enable the transfer of pyrophosphate. A deeper understanding of the molecular mechanisms that influence the event of pyrophosphate transfer to GTP or GDP will provide clues on the interactions that modulate the catalytic accuracy of Rel enzymes. A model for the pyrophosphate transferase enzymatic mechanism has been postulated on the basis of the binary $Rel_{Seq}385$ substrate complex [Hogg et al., 2004]. This structure supported a single-cation mechanism similar to the divalent-cation mechanism proposed for DNA polymerases [Arndt et al., 2001; Beard and Wilson, 2006]. According to the Hogg et al., [2004] mechanism, the reaction proceeds by an in-line nucleophilic attack of the 3'-OH group of GDP (or GTP) onto the β-phosphorus atom of ATP. Most likely, Glu323 could activate the hydroxyl group by proton abstraction; supposedly, it coordinates the essential $Mg^{2+}$ ion and is expected to bind to the pyrophosphate donor ATP, which is not present in the crystals [Hogg et al., 2004]. Support for a critical role of Glu323 in the synthetase mechanism derives from a follow-up mutational study: A $Rel_{Seq}385$ mutant bearing a Glu323Gln substitution exhibited severely defective synthetase activity. However, the configuration of the synthetase active site through local conformational changes such as alternate side-chain rotamers and main-chain backbone motion induced by the different binding modes of the substrates/substrate-analogs or product/product-analogs provides an understanding of the pyrophosphate transfer mechanism. In fact, modeling of an $ATP \bullet Mg^{2+}$ complex in proximity to the GDP of the $Rel_{Seq}385 \bullet GDP$ S-ON pocket [PDB Id:1VJ7/chain A; Hogg et al., 2004]

83

along with the information on the position of the 3'-pyrophosphate of ppGpp derived from this work reveal intriguing observations (Figure 4.1.20).
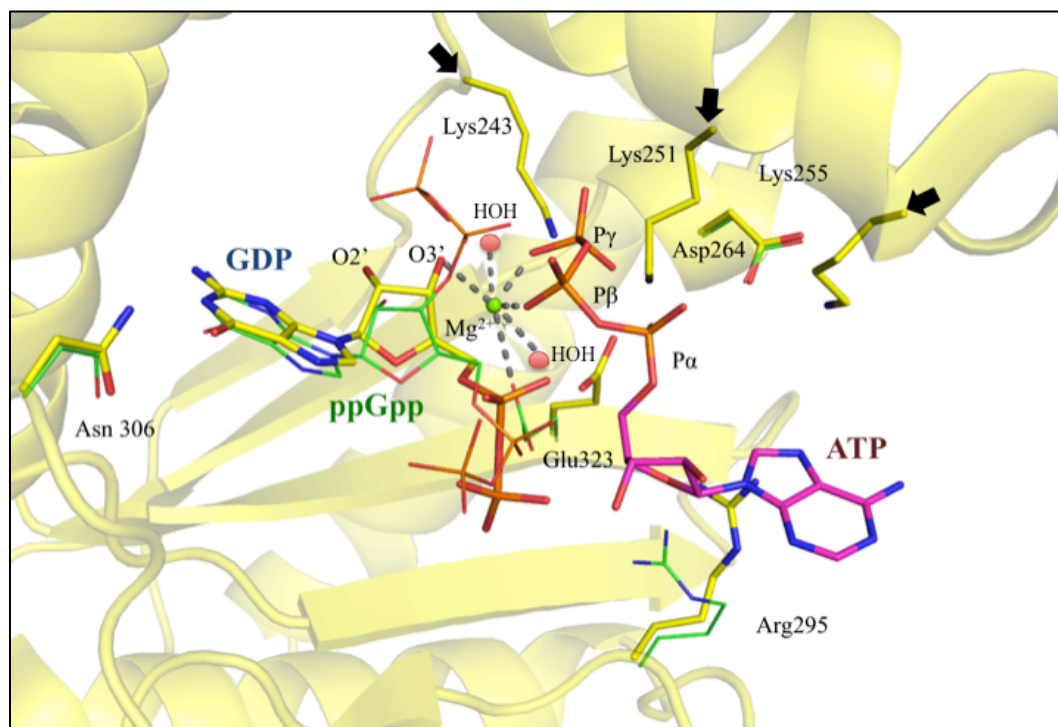


**Figure 4.1.20**: Modeled ternary $Rel_{Seq}385 \cdot GDP \cdot ATP \cdot Mg^{2+}$ complex overlayed with the $Rel_{Seq}385 \cdot ppGpp$ complex (complex III). The $Rel_{Seq}385 \cdot ppGpp$ complex is displayed as thin sticks in green. The 1VJ7 chain A synthetase site is displayed as thick sticks in yellow. Arrows represent presumable steric clashes between ATP and Lys243, Lys251, and Lys255. The green sphere represents $Mg^{2+}$. The red spheres represent water molecules. Dotted gray lines represent metal interactions.

## 4.1.10 Presumable transition-state complex and pyrophosphate transfer mechanism

As per the proposal by Hogg et al. (2004), the distance between Glu323-O$\epsilon$1 and the 3'-OH will be reduced upon coordination of both groups to $Mg^{2+}$. With such a conformational re-arrangement, an ATP molecule with 5'-O1$\beta$ and 5'-O1$\gamma$ coordinating to $Mg^{2+}$ has been modeled. The modeled ATP$\cdot Mg^{2+}$ was suitably placed to interact with 3'-OH of GDP or GTP. The arrangement of Glu323-O$\epsilon$1 in the ppGpp bound structure agrees with the coordination proposed for $Mg^{2+}$. Although residues Lys251 and Lys255 make steric clashes with $\alpha$ and $\gamma$ phosphates of the modeled ATP,

it can be assumed that upon ATP•Mg$^{2+}$ binding, the critical residues Asp264 and Glu323 might loose their hydrogen bonds from Lys251 and Lys255, respectively, and rearrange. Most possibly, the guanidinium group of Arg295 forms a cation-π interaction with the adenine base. The orientation of Asp264 is nearly identical in all complexes. The distance separation of Asp264 from the modeled Mg$^{2+}$ is greater than 6 Å, suggesting that Asp264 has to undergo an essential displacement to co-ordinate with ATP•Mg$^{2+}$. In fact, the combination of modeled ATP•Mg$^2$ with the structure of the Rel$_{Seq}$385•GDP and ppGpp/ppGpp-analog complexes suggests a plausible model for a single-cation mechanism of pyrophosphate transfer by Rel$_{Seq}$ (p)ppGpp synthetases (Figure 4.1.21 A & B, see below). The C3' hydroxyl group of GTP (GDP), Glu323, and the rearranged Asp264 in a proximal "IN" conformation might coordinate Mg$^{2+}$. In this arrangement, the C3' hydroxyl could undergo deprotonation through proton abstraction by Glu323 (Figure 4.1.21 A). Such an arrangement leads to guanosine hexaphosphate adenylate, a probable pentacoordinated bipyramidal beta-phosphate transition state (Figure 4.1.21 B). The transition state could be resolved by the release of the by-product AMP from the 5'-β–phosphate of ATP at the opposite side of the attacking 3'-O-site. Consequently, a stereochemical rotation might occur at the 5'-β-phosphate of ATP (now turned into the 3'-α-phosphate of the (p)ppGpp formed). The positioning of Lys251 in proximity to the α and β phosphate groups of ATP suggests the possibility that the leaving AMP group could be protonated by the basic amino-acid residue. However, it remains to be clarified whether the AMP separation occurs as a dissociative or associative nucleophilic attack, or concerted. Unlike all DNA polymerases, Rel enzymes possess a conserved aspartate residue and a conserved glutamate residue that might coordinate to the Mg$^{2+}$ ion participating in the pyrophosphate transfer reaction. Mg$^{2+}$ could lower the pK$_a$ of the 3'-OH of the (p)ppGpp formed as well as coordinate the 5'-O1β and 5'-O1γ of the ATP. Additionally, the release of pyrophosphate with Mg$^{2+}$ from ATP with the aid of Lys251 could assist AMP dissociation.

Thus, a plausible model for pyrophosphate transfer through a pentacoordinated transition state can be predicted from the available Rel$_{Seq}$385 complex structures.
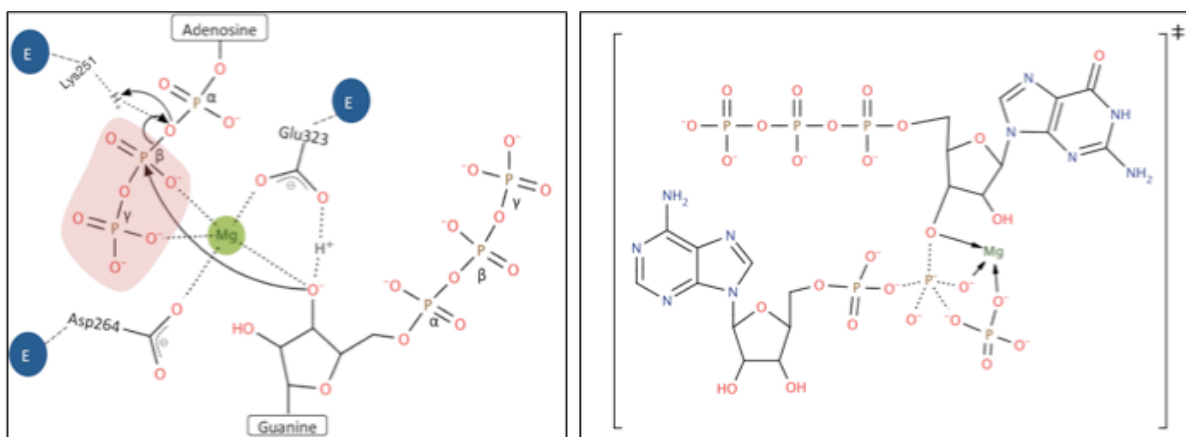
**Figure 4.1.21: A)** Schematic drawing of the proposed single-metal-ion mechanism of pyrophosphate transfer in Rel$_{Seq}$ (p)ppGpp synthetases. E in circle represents the corresponding protein environment. **B)** Guanosine hexaphosphate adenylate – a probable penta-coordinated beta-phosphorus transition state during the formation of pppGpp.

### 4.1.11 Conclusions

The three dimensional structure of Rel$_{Seq}$385 with product and product-analogs reveal a surprising plasticity of the synthetase active site that seems to be independent of interdomain crosstalk. An intriguing observation is that in all of the complexes there is an acceptor substrate or product or product analog bound to the synthetase site but not in the hydrolase site. Product, ppGpp, and their analogs in the synthetase domain would lock the synthetase site in a stable ON state, whereas acceptor substrates such as GDP, GTP or its analog, GppNHp, bind to the synthetase site in both OFF and ON states. A product mimic, GppNHp, or a product intermediate, ppG2':3'p, of the (p)ppGpp hydrolysis reaction prefers binding to the hydrolase site in ON state. The conformational state of molecule 2 of complex III reveals that dynamic conformational intermediates stages are plausible. Hence, it can be postulated as such that the reciprocal coupling of the activity states only prevents ineffective cycles of (p)ppGpp synthesis and hydrolysis; with the regulation itself probably depends on the lacking C-terminal half of the protein and on ribosome association.

Since stringent factors are absent in mammals, ppGpp analog compounds such as compound (10) and compound (15) point a way towards designing potential inhibitors

to Rel proteins [Wexselblatt et al., 2010]. Success in eliciting antibacterial properties against the stringent response mechanism is overdue. The significance of (p)ppGpp as the regulator of stringent response mechanism is the main motivation to study non-hydrolyzable ppGpp analogs targeting $Rel_{Seq}385$. The structural investigations from this study suggest that ppGpp analogs can be used as structural probes in studying the regulation of the (p)ppGpp catalysis. The $Rel_{Seq}385$ complex structures provide templates that will help design novel (p)ppGpp -synthetase or -hydrolase inhibitors. Recently, Relacin, has been established as a novel antibacterial agent potentially targeting the stringent response [Wexselblatt et al. 2012]. Relacin is a 2'-deoxyguanosine-based analog of ppGpp, in which the original pyrophosphate groups at positions 5' and 3' were replaced by glycyl-glycine dipeptides linked to the sugar ring (Figure 4.1.22). The production of (p)ppGpp, both *in vivo* and *in vitro*, has been markedly inhibited by Relacin. Also, Relacin appears to specifically target stringent factors, since the effect of the compound was nearly undetectable on Rel/Spo mutant cells. Moreover, Relacin perturbs the switch into stationary phase in Gram-positive bacteria, thereby causing bacterial death [Wexselblatt et al., 2012].
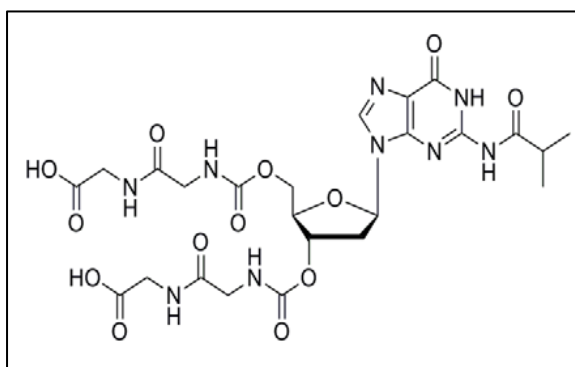


**Figure 4.1.22**: **Chemical structure of Relacin. (Wexselblatt et al., 2012)**

The structures determined so far show that no global conformational changes occur upon acceptor-substrate binding or product binding to the synthetase domain and product binding to the hydrolase domain. Hence, the design of an anti-ppGpp drug candidate (i.e., a drug against bacterial stringent response mechanism) may only need to target one conformation. Therefore, it is anticipated that potential candidates such as Relacin, compound (10) or (15), and transition state analogs of guanosine hexaphosphate adenylate will be tested in the future.

## 4.2 Rel$_{Seq}$385: Metal selectivity by the hydrolase domain

During recombinant Rel$_{Seq}$385 production and crystallization, no transition metal ions were present in the buffer. However, in all the available Rel$_{Seq}$385 complexes (Hogg et al., 2004; Section 4.1 of this study), one highly occupied metal ion site is present per hydrolase domain. The metal ion that has traditionally been reported to be essential for the hydrolase activity was Mn$^{2+}$ [Raue and Cashel, 1975; Sy, 1977; Mechold et al., 1996]. Most likely, metal ions from the *E. coli* expression cells were initially co-purified with Rel$_{Seq}$385. Here, anomalous X-ray scattering and atomic absorption spectroscopy have been used to determine the identity of the metal ion incorporated into the hydrolase active site.

### 4.2.1 Anomalous X-ray scattering

Co-purified and co-crystallized metal ions from the Rel$_{Seq}$385 crystal are heavy atoms, as their elemental absorption and anomalous scattering facilitate their identification in the three-dimensional crystal lattice. The X-ray absorption-edge scan permits determination of values for the heavy-atom anomalous scattering factors f′ and f″ as a function of energy in electron volt (eV). Initial absorption-edge scans from a few Rel$_{Seq}$385 crystals displayed significant indications for the presence of a zinc absorption edge rather than manganese absorption edge. An example is shown in figure 4.2.1 A & B.
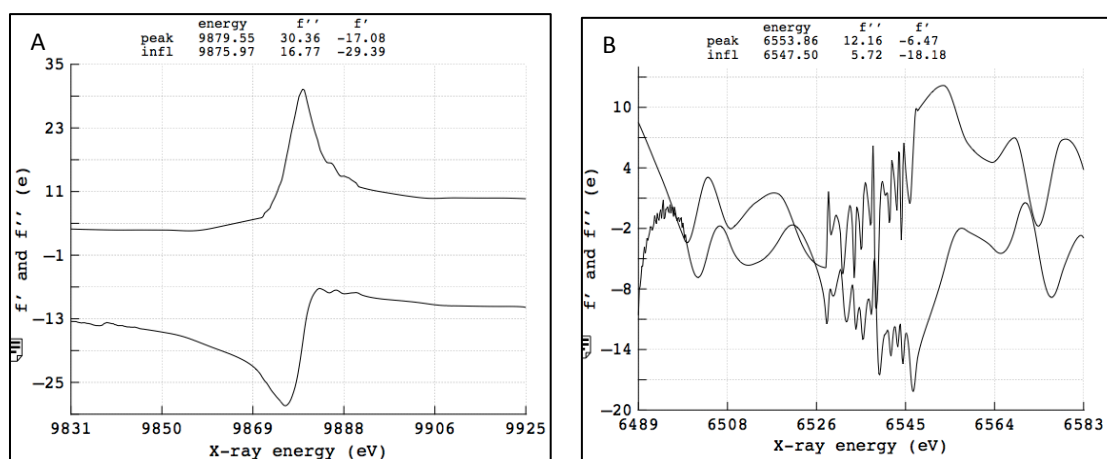


**Figure 4.2.1**: Plot of f′ and f″ against energy around (A) the Zn-K absorption edge (9880 eV) and (B) the Mn-K absorption edge (6554 eV) calculated from X-ray fluorescence measurements on a Rel$_{Seq}$385 crystal at beamline 14.2, BESSY, Berlin.

## 4.2.2 The quality of the crystal structures

The overall structures are identical to that previously solved [Hogg et al., 2004; PDB ID: 1VJ7]. These datasets were refined mainly to provide phases for the construction of anomalous difference maps and there is no new structural information to report. Data collection and refinement statistics are listed in Table 4.8 and indicate that the data and refinement are robust.

**Table 4.8**: Data collection and refinement statistics.

| | Zn peak dataset | Mn peak dataset |
|---|---|---|
| **Data collection statistics** | | |
| Beamline | BL14.2 - BESSY | BL14.2 - BESSY |
| Energy | 9880 eV | 6554 eV |
| Wavelength | 1.283 Å | 1.899 Å |
| Space group | C2 | |
| Cell dimensions a, b, c (Å); α, β, γ (°) | 173.28, 50.22, 127.67; 90, 109.22, 90 | 173.47, 50.29, 127.42; 90, 109.09, 90 |
| Resolution (Å) | 33.38–3.50 (3.69–3.50) | 33.36–3.50 (3.69–3.50) |
| $R_{sym}$[#] (%) | 6.3 (23.5) | 5.8 (20.1) |
| I / σI [§] | 12.1 (5.1) | 12.6 (5.7) |
| Completeness (%) | 99.3 (99.0) | 98.7 (97.2) |
| Redundancy | 3.6 (3.6) | 3.6 (3.6) |
| Anomalous completeness (%) | 93.8 (92.5) | 93.6 (90.9) |
| Anomalous multiplicity | 1.9 (1.9) | 1.9 (1.8) |
| **Refinement statistics** | | |
| No. of reflections (work / free) | 29078 / 1546 | 13072 / 689 |
| $R_{work}$ / $R_{free}$ [†] (%) | 20.3 / 22.5 | 21.0 / 26.6 |
| No. of atoms / average B-factor (Å$^2$) | 1610/26.5 | 1555/39.6 |
| r.m.s. deviations of bond lengths (Å) | 0.016 | 0.018 |
| r.m.s. deviations of bond angles (°) | 1.81 | 1.94 |
| Ramachandran plot (% preferred region / % allowed region) | 96.74 / 3.26 | 95.72 / 4.28 |

The values in the parentheses refer to the highest resolution shell.

[#]$R_{sym} = (\sum | I_{hkl} - <I_{hkl}> |) / (\sum I_{hkl})$, where the average intensity $<I_{hkl}>$ is taken over all symmetry-equivalent measurements and $I_{hkl}$ is the measured intensity for any given reflection.

[§]I/σI is the mean reflection intensity divided by the estimated error.

[†]$R_{work} = ||F_o| - |F_c|| / |F_o|$, where $F_o$ and $F_c$ are the observed and calculated structure factor amplitudes, respectively. $R_{free}$ is equivalent to $R_{work}$ but calculated for 5% of the reflections chosen at random and omitted from the refinement process.

### 4.2.3 Anomalous-difference Fourier syntheses

MR-phased anomalous difference Fourier syntheses from both datasets were calculated. For the 1.283-Å (9880-eV) dataset, the positions of the two prominent peaks in the asymmetric unit were identical to those of the two metal ions in the original native Fourier maps (this work, section 4.1). This is consistent with the fact that the anomalous-dispersion component f $''$ of a $Zn^{2+}$ ion is larger than that of a $Mn^{2+}$ at this wavelength or energy. In this Fourier map (Figure 4.2.2 A), only the anomalous scatterers can be located. Hence, the two prominent peaks can be unambiguously assigned to the $Zn^{2+}$ ion positions of the two molecules in the asymmetric unit. For the 1.899-Å (6554-eV) dataset, the f $''$ contribution of the $Mn^{2+}$ ion is smaller, and also only insignificant electron-density maxima were found in the anomalous difference Fourier map around the expected positions of metal ions (Figure 4.2.2 B). These peaks in the asymmetric unit could still be assigned to metal-ion positions, whereas the electron density peaks at this possible metal-ion positions were lower than those derived from the 1.283-Å (9880-eV) dataset (Table 4.9). This can be presumed as a contribution from f $''$ of $Zn^{2+}$ at the wavelength of 1.899 Å or energy of 6554 eV.

**Table 4.9:** Electron density $(e/Å^3)$ or σ above mean values at the metal sites of $Rel_{Seq}385$ measured from the anomalous difference Fourier maps ($\Delta F_{ano}$).

| Metal edge | Zn-K (9880 eV) | Mn-K (6554 eV) |
|---|---|---|
| **Monomer 1 (H-OFF)** | | |
| $e/Å^3$ | 10.39 | 5.56 |
| (σ above mean) | (12.80) | (6.81) |
| **Monomer 2 (H-ON)** | | |
| $e/Å^3$ | 10.88 | 4.82 |
| (σ above mean) | (13.40) | (5.91) |
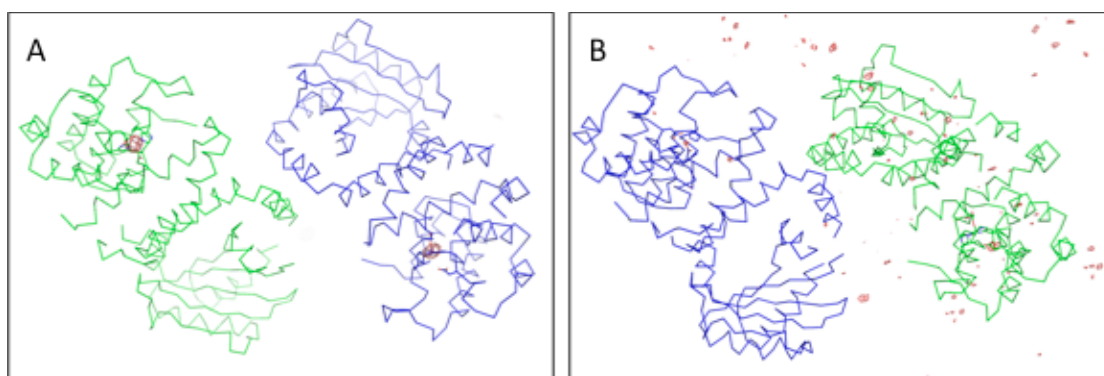
**Figure 4.2.2** Anomalous-difference Fourier maps ($\Delta F_{ano}$) calculated using phases from MR solutions and anomalous differences measured for a Rel$_{Seq}$385 crystal at (A), 1.283 Å/ 9880 eV for the zinc peak dataset (red, contoured at 5 σ above the mean) and (B), 1.899 Å/ 6554 eV for the manganese peak dataset (red, contoured at 4 σ above the mean).

### 4.2.4 Atomic absorption spectroscopy

Amounts of metal ions bound to recombinant Rel$_{Seq}$385 were measured using atomic absorption spectrometry. Rel$_{Seq}$385 purified from expression cultures not supplemented with any metal ion contained 0.79 Zn$^{2+}$ per Rel$_{Seq}$385 monomer, and 0.03 Mn$^{2+}$ per Rel$_{Seq}$385 monomer. The zinc ions originated from the 2X TY-medium used for cell growth. Further, the metal preference in Rel$_{Seq}$385 between zinc and manganese was assessed by a competition assay after extensive EDTA treatment. After supplementing an equal-molar-ratio mixture of Zn$^{2+}$ and Mn$^{2+}$ to the metal-free and EDTA-free Rel$_{Seq}$385, an incorporation of 0.62 Zn$^{2+}$ per Rel$_{Seq}$385 monomer and 0.10 Mn$^{2+}$ per Rel$_{Seq}$385 monomer was observed. Thus, Rel$_{Seq}$385 was found to be a metalloprotein that favours zinc-ion binding over manganese-ion binding (Table 4.10).

**Table 4.10** Atomic absorption spectroscopic quantification of the metal incorporation into Rel$_{Seq}$385.

| Samples / addition of: | Zn / monomer | Mn / monomer |
|---|---|---|
| Rel$_{Seq}$385 (before EDTA treatment) | 0.79 | 0.03 |
| Rel$_{Seq}$385 (after EDTA treatment) | 0.07 | 0.04 |
| Rel$_{Seq}$385 (after Mn$^{2+}$ addition) | 0.04 | 0.05 |
| Rel$_{Seq}$385 (after Zn$^{2+}$ addition) | 0.62 | 0.09 |
| Rel$_{Seq}$385 (after Mn$^{2+}$ & Zn$^{2+}$ addition) | 0.62 | 0.10 |

### 4.2.5 Conclusions

One of the crucial steps in the bacterial stringent response mechanism is the regulation of (p)ppGpp-signaling by metal-dependent 3'- pyrophosphate hydrolysis of (p)ppGpp. The metal-activated hydroxide ion is a discerning nucleophile in metallohydrolases. The most commonly observed metal ion in these reactions is Zn$^{2+}$. In certain cases, other transition metals such as manganese are involved. Bacteria industriously acquire several transition elements and implement them in structurally restricted binding sites to perform regulatory or catalytic roles [Finney and O'Halloran, 2003]. Investigations of transition metal allocation in *Escherichia coli* revealed that individual bacteria accumulate Fe and Zn by several orders of magnitude relative to the concentration in a typical growth medium, which is in the range of approximately 0.1 mM (i.e. approximately 10$^5$ ions per cell). However, metal ions such as Mn$^{2+}$ and Cu$^{2+}$ are limited to the 10- to 100-µM range (i.e. approximately 10$^7$ to 10$^8$ -ions per cell) [Finney and O'Halloran, 2003]. Unlike first-row transition metal ions such as Mn$^{2+}$, Fe$^{2+}$, Co$^{2+}$, Ni$^{2+}$, or Cu$^{2+}$; the zinc ion (Zn$^{2+}$) contains a filled d orbital ($d^{10}$). Due to the filled d-shell in Zn$^{2+}$, (i) it does not take part in redox reactions but functions as a Lewis acid instead, and (ii) it has a ligand-field stabilization energy of zero in all liganding geometries, allowing a variety of potential

coordination geometries [Williams, 1987; Christianson and Cox, 1999; McCall et al., 2000]. A significant kinship between the $d^{10}$ $Zn^{2+}$ and the $d^5$ $Mn^{2+}$ is that neither is subject to the complications of ligand field stabilization effects. The evolution of hydrolase specificity for a transition metal ion such as $Mn^{2+}$ or $Zn^{2+}$ depends on a number of factors such as environmental adequacy, appropriate chemical properties, and biological convenience. By nature, $Zn^{2+}$ and $Mn^{2+}$ exhibit differences in their ionic radii and effective nuclear charges. In addition, a major difference between these two metal ions is that manganese is capable of redox behavior under biological conditions, whereas zinc is not. The inherent archetype coordination geometry for $Mn^{2+}$ is square-pyramidal or trigonal-bipyramidal with a coordination number of five, or octahedral with a coordination number of six. $Zn^{2+}$ paradigmatically prefers tetrahedral with a coordination number of four, although the coordination number can increase to five or six to stabilize high-energy intermediates [Alberts et al., 1998; Christianson and Cox, 1999].

In the $Rel_{Seq}385$ crystal structure, the catalytic metal ion in the hydrolase domain of the enzyme molecule is located close to the bottom of an approximately 10 Å deep active-site cavity. In one $Rel_{Seq}385$ conformer, the metal ion is coordinated to two imidazole groups from His53 and His77, to $O\partial1$ of Asp144 and to two water molecules. In the other conformer, a sixth ligand, completing nearly a symmetric-octahedral coordination geometry, is $O\partial1$ of Asp78. Also, the $Rel_{Seq}385$ complex crystal structures showed that the metal coordinations in $Rel_{Seq}385$ hydrolase could switch between 5-fold, and 6-fold [Hogg et al., 2004; also this study - section 4.1]. $Zn^{2+}$ and $Mn^{2+}$ are the best candidate metal ions for coordination with HD motif of $Rel_{Seq}385$.

*In-vivo* [Raue and Cashel, 1975] and *in-vitro* [Sy, 1977] studies demonstrated that stimulation of ppGpp hydrolytic activity occured upon $Mn^{2+}$ addition. In these studies, it was also shown that $Zn^{2+}$ ions could partially substitute the $Mn^{2+}$ ions. However, an *in-vitro* study of the $Rel_{Seq}$ hydrolytic activity revealed similarities with $SpoT_{Ec}$ that include the stimulation of activity by $Mn^{2+}$ ions, which cannot be replaced by $Ca^{2+}$, $Co^{2+}$, $Zn^{2+}$, or $Fe^{2+}$ [Mechold et al., 1996]. There are few structurally known HD motifs with bound metal ions. Besides iron, cobalt, nickel, calcium, and magnesium, the most commonly observed metal ion in the HD motif is zinc. In these structurally known HD motif-containing zinc metallohydrolases, the binding geometry is distorted

with the metal ion coordinating three or four protein side-chains. Most of the HD motif-containing proteins involve a second site metal for catalysis (see Appendix 6.10).

In this work, anomalous X-ray scattering and atomic absorption spectroscopy revealed a $Zn^{2+}$ ion in the hydrolase active site of $Rel_{Seq}385$. It can be presumed that the $Zn^{2+}$ ion coordinates directly with the HD motif. Possibly, a $Mn^{2+}$ ion occupy a co-catalytic second site coordinating with substrate, explaining why the presence of both is essential for the (p)ppGpp hydrolysis reaction. Mechold et al., [1996] showed that the *in-vitro* (p)ppGpp hydrolysis of the purified $Rel_{Seq}$ is Mn⁻dependent and not Zn-dependent. It is possible in their experiments, the purified $Rel_{Seq}$ was bound with $Zn^{2+}$ whereas $Mn^{2+}$ and (p)ppGpp were added later in the *in-vitro* assays. The added $Mn^{2+}$ ions might have greatly stimulated the rate of hydrolysis by increasing the affinity of the catalytic site for the (p)ppGpp substrate. Recent crystal structures of bacterial DnaG-type primases in complex with pppGpp (PDB ID: 4EDV) and ppGpp (PDB ID: 4EDT) revealed that the 3' phosphates of both nucleotides directly engage with a $Mn^{2+}$ ion [Rymer et al., 2012].

A close inspection of the $Rel_{Seq}385$ hydrolase in complexes with the intermediate substrate (ppG2':3'p; PDB ID: 1VJ7; Hogg et al., 2004) and the product analog (GppNHp; complex IV; section 4.1, this study) in the hydrolase site reveals ample space for a second metal ion, with probable involvement of the substrate (p)ppGpp, and protein residues Glu81, Asp82, Tyr50, or water (Figure 4.2.3 A). Overall, this hypothesis suggests that $Rel_{Seq}$ is a hetero-dinuclear metallohydrolase. On this basis ($Zn_A/Mn_B$), a model has been developed which is illustrated in figure 4.2.3 B. The hydrolase subunit (HD domain) is highlighted with the bound zinc. The scheme shows a pathway for the pppGppase, one with the second metal ion-binding site empty (I) and the second with this site occupied by Mn•pppGpp (II). The cycles are in a metal ion-dependent equilibrium before pppGpp hydrolysis and immediately after the hydrolysis (I ↔ II). In the presence of a high concentration of free $Mn^{2+}$ ions, (p)ppGpp will be quickly hydrolyzed (II → I), but, after the release of Mn-PPi, the metal ion induces a very stable complex between GTP and the enzyme (III). In addition to the occupation of the $Mn^{2+}$-binding site, it is possible that certain conformational requirements are needed for the stable complex (III) to occur.
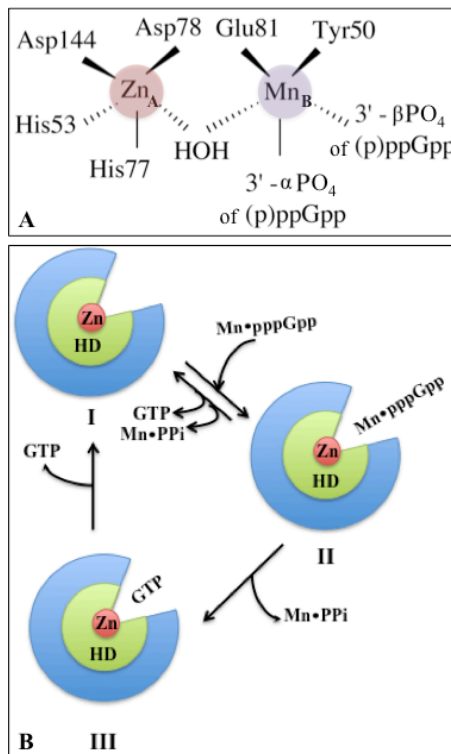
**Figure 4.2.3:** (A) Schematic representation of the suggested Rel$_{Seq}$385 hydrolase active site providing the coordination environment of the two metal ions Zn$_A$/Mn$_B$. (B) Proposed model for Rel$_{Seq}$385 hydrolase for the reaction cycles during (p)ppGpp hydrolysis, based on the occupation of the second metal-ion-binding site.

Metallohydrolases such as mammalian purple acid phosphatases [Fe(III)-Fe(II)] and kidney bean purple acid phosphatase [Fe(III)-Zn(II)] has dinuclear metal active sites. In these cases, the mechanism of phosphate ester hydrolysis involves a nucleophilic attack on the phosphate group by a Fe(III)-coordinated hydroxide ion [Sträter et al., 1995]. Two metal ions (Zn$_A$/Mn$_B$; Figure 4.2.3 A, see above) will stabilize a coordinated hydroxyl ion (or catalytic water) better than one because the number of metal ions to which the nucleophilic hydroxyl ion is coordinated reconciles the reactivity of the metal-activated hydroxyl ion.

## 4.3 RelA$_{Ec}$ ACT: Crystal structure of the fragment RelA$_{Ec}$564-744
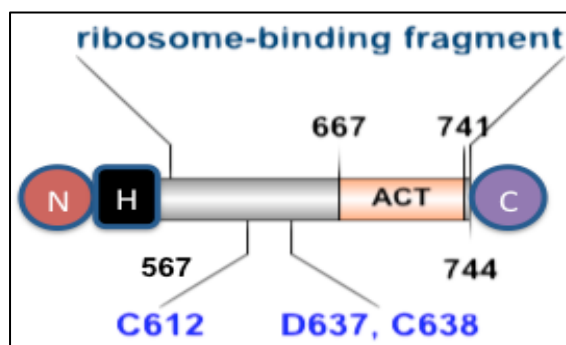


**Figure 4.3.1:** Domain organization of RelA$_{Ec}$564-744. ACT domain (Pfam reference: accession no. PF01842): residues 667-741 (ACT domain defined according to Pfam database, Sanger Institute, UK). Ribosome-binding fragment: residues 564-744; C612, D637, and C638 are involved in RelA$_{Ec}$ oligomerization [Gropp et al., 2001]. N refers to N –terminus, H refers to His$_6$ tag and C refers to C-terminus.

### 4.3.1 Recombinant protein production

RelA$_{Ec}$564-744 was successfully produced under heterologous conditions, at about 7 mg of protein per liter expression culture. RelA$_{Ec}$564-744 carrying a His$_6$ tag at the N terminus was purified in two steps, Ni$^{2+}$-NTA affinity and gel filtration chromatography. The protein exhibited an apparent molecular mass of about 22.2 kDa under denaturing conditions in SDS-PAGE (Figure 4.3.2 A) and Western blot (Figure 4.3.2 B). Purified protein fractions were pooled, concentrated to a final concentration of 4 mg/ml and used for crystallization studies. Purified RelA$_{Ec}$564-744 was assessed by Dynamic Light-Scattering (DLS). As evident from figure 4.3.2 (C), the RelA$_{Ec}$564-744 protein exhibited a high degree of oligomerization with a hydrodynamic radius of 40 to 110 nm, experiments showed that the sample was broadly monodisperse (54.58 nm ± 6.80 nm).
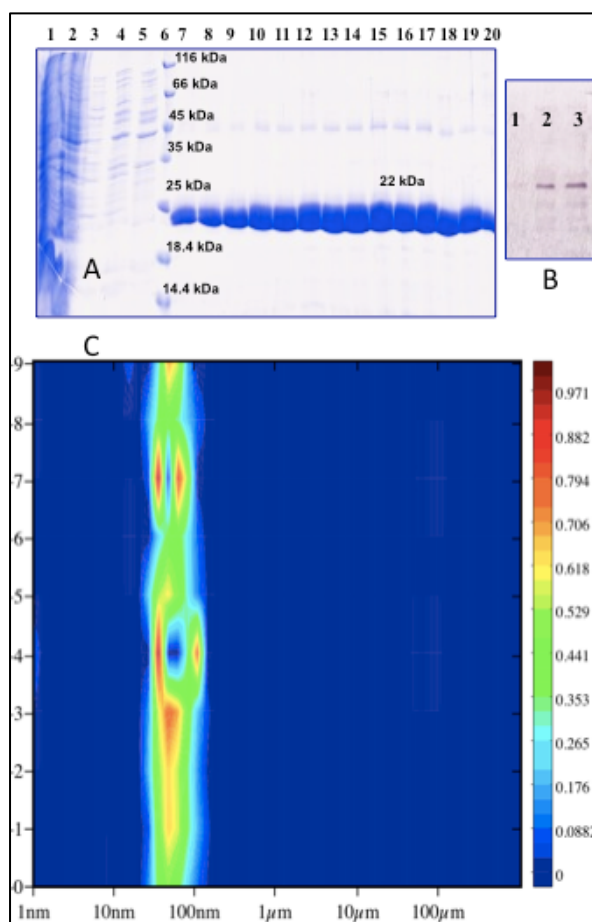
**Figure 4.3.2**: (A) SDS-PAGE of RelA$_{Ec}$564-744; Lane 1: *E. coli* lysate after induction, lane 2: flow-through of Ni$^{2+}$-NTA chromatography, lanes 3 - 5: three column washes, lanes 7 - 20: His$_6$- RelA$_{Ec}$564-744 eluted with an imidazole gradient. Lane 6: marker proteins with apparent molecular masses of 116 (most upper band), 66, 45, 35, 25, 18.4, 14.4 kDa (lowest band). (B) Western blot analysis of His$_6$-RelA$_{Ec}$564-744 using anti-Histidine; lane 1: BSA (control), lane 2: His$_6$- RelA$_{Ec}$564-744 (after Ni$^{2+}$-NTA chromatography), lane 3: His$_6$- RelA$_{Ec}$564-744 (after gel-filtration chromatography). (C) Dynamic Light-Scattering of purified RelA$_{Ec}$564-744.

## 4.3.2 Crystallization of RelA$_{Ec}$564-744

Initial crystallization trials were carried out using a Phoenix robot (Dunn Labortechnik, Thelenberg, Germany) employing the sitting-drop vapor diffusion method in a nano-scale volume (200 nl). Initial crystalline hits were optimized by manually setting up 2-µl hanging drops consisting of 1 µl of protein and 1 µl of reservoir solution. Crystals grew as clusters of thin plates within precipitated protein.

After extensive optimization, thin plate-like single crystals were obtained. To obtain well-diffracting crystals, the protein was mixed with an equivolume of 1500 mM – 2000 mM ammonium sulfate, 800 mM – 1000 mM KCl, and 100 mM sodium acetate pH 4.6 (25°C). Using the hanging drop technique, crystals grew approximately up to 50 x 40 x 5 $\mu m^3$ within 3 - 4 weeks at 20°C (Figure 4.3.3).
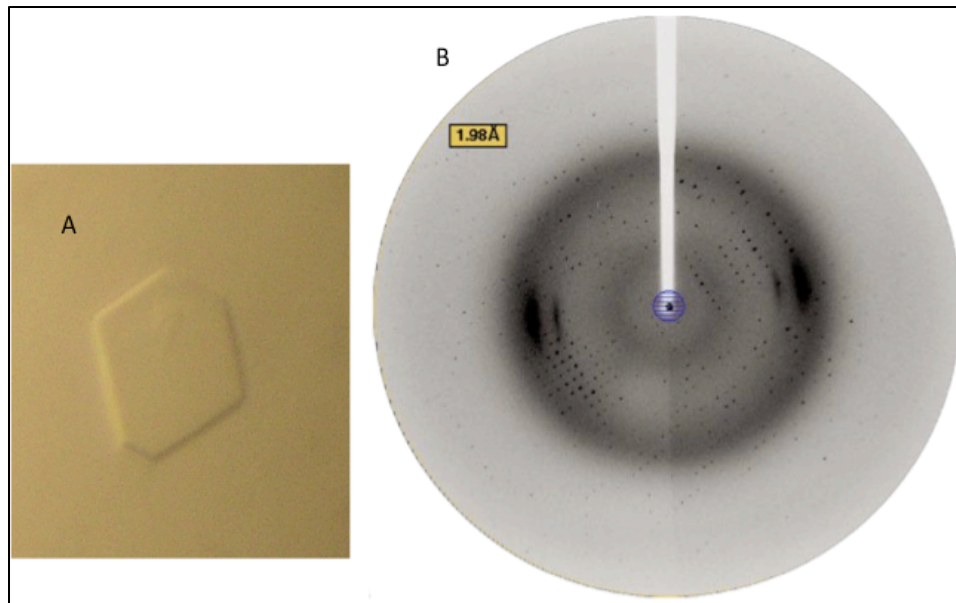


**Figure 4.3.3:** (A) Thin plate-like RelA$_{Ec}$564-744 protein crystal used for data collection (RACE 1). (B) An X-ray diffraction image from RACE1.

**Table 4.11**: Data collection and refinement statistics

| Crystals | RACE 1 | RACE 2 |
|---|---|---|
| .... | .... | ... |
| Wavelength (Å) | 1.40001 | 0.91841 |
| Beamline | 14.1 BESSY II | 14.1 BESSY II |
| Space group | $P2_1$ | $P2_1$ |
| Cell dimensions | ... | ... |
| a, b, c (Å) | 30.36, 46.82, 58.34 | 29.36, 47.00, 58.82 |
| $\alpha,\beta,\gamma$ (°) | 90, 100.97, 90 | 90, 98.54,90 |
| Resolution (Å) | 57.29 –2.00 (2.11–2.00) | 58.17-2.50 (2.64-2.50) |
| [a]$R_{merge}$ | 11.3 (52.9) | 9.7 (35.7) |
| [b]$R_{pim}$ | 7.8 (39.5) | 7.2 (26.6) |
| I / σI | 5.1 (2.0) | 7.2 (3.0) |
| Completeness (%) | 100 (100) | 98.4 (98.4) |
| Redundancy | 3.5 (3.4) | 3.3 (3.3) |
| **MR Phasing statistics** | .... | ... |
| RFZ score | 10 | 15.2 |
| TFZ score | 25.1 | 23.8 |
| LLG | 1037 | 854 |
| **Refinement statistics** | .... | ... |
| Resolution (Å) | 57.29 –2.00 | 58.17-2.50 |
| No. of reflections | 10458 | 5256 |
| [c]$R_{cryst}$ / $R_{free}$ | 21.7/26.0 | 22.8/28.9 |
| No. of atoms/ average B-factors (Å$^2$) | 1316/12.92 | 1242/26.21 |
| rms deviations | .... | ... |
| Bond lengths (Å) | 0.020 | 0.012 |
| Bond angles (°) | 1.876 | 1.656 |

Values in parentheses correspond to the value in the highest resolution shell.

[a]$R_{merge} = \Sigma_{hkl}\Sigma_i \,|I(hkl)_i - <I(hkl)>| \,/\, \Sigma_{hkl} \,\Sigma_i \,I(hkl)_i$, where $I(hkl)$ is the intensity of reflection $hkl$ and $<I(hkl)>$ is the average intensity over all equivalent reflections.

[b]$R_{pim}$ is the precision-indicating merging $R$ factor (Weiss and Hilgenfeld, 1997).

[c]LLG = log-likelihood gain, which expresses the probability of the solution compared to a random model.

[d]$R_{cryst} = \Sigma_{hkl} \,|F_o(hkl) – F_c(hkl)| \,/\, \Sigma|F_o(hkl)|$. $R_{free}$ was calculated for a test set of reflections (5%) omitted from the refinement.

### 4.3.3 Crystal structure determination

Initial attempts to determine the crystal structure of $RelA_{Ec}564$-$744$ were made using experimental phasing methods with $KI/I_2$-derivative data to 2.0 Å resolution (RACE 1 at a wavelength of 1.40 Å) (Figure 4.3.3 B) and native data to 2.5 Å resolution (RACE 2 at a wavelength of 0.92 Å). Preliminary $KI/I_2$-derivatization of $RelA_{Ec}564$-744 crystals (RACE1) was performed by a soaking method in which the native crystals were soaked in a 10% (v/v) $KI/I_2$ solution for a short period of 30-60 s and washed in the mother liquor for 5-10 s. Each crystal was immediately transferred into the cryobuffer (26% ethylene glycol, 50 mM sodium acetate pH 4.6 at 25°C) and subsequently flash-cooled to 100 K in a cold nitrogen-gas stream. Complete diffraction datasets for two crystals (labeled as RACE 1 and RACE 2; Table 4.11, see above) were collected. Data collection statistics are given in Table 4.11. To exploit the weak anomalous signal derived from the sulphurs (Cys612 and Cys638) inherent to $RelA_{Ec}564$-744 or in particular from anionic iodine potentially incorporated in $KI/I_2$-soaks RACE 1 dataset was collected at a wavelength of 1.40 Å, which would give weak anomalous signals. However, due to a low anomalous signal-to-noise ratio of <0.8 in the >3.5 Å resolution bin, the data was insufficient to determine the structure by experimental phasing methods.

Later, using a modified poly-alanine model of the ACT domain from 3-phosphoglycerate dehydrogenase (3PGDH) [Dey et al., 2007; PDB ID: 2P9C] as an initial search model, a solution with promising score was identified using molecular replacement phasing method. Subsequent modification of the coordinate set by truncating two surface loops of the ACT domain yielded an enhanced search model that allowed structure determination using the high-resolution dataset with $P2_1$ spacegroup. The resulting $2F_o$-$F_c$ electron-density maps could be easily interpreted, allowing the building of all main-chain residues of the ACT domain (residues 665-744). The model was completed using automated and manual model building (Figure 4.3.4, see below). In contrast to the well-defined ACT domain, no electron density for residues 564-664 were apparent. This suggests that during crystallization, these residues were cleaved off and crystals contained the ACT domain only. The crystallized RelA fragment (residues 665-744) will be referred to as $RelA_{Ec}$ ACT in the following. The $F_o$-$F_c$, $2F_o$-$F_c$ or anomalous difference Fourier synthesis calculated

maps from the RACE 1 dataset did not provide the locations of the iodine. Also, the MR-phasing of RACE 2 revealed the cleaved fragment (residues 665-744) that has been crystallized. Refinement statistics are included in table 4.11.
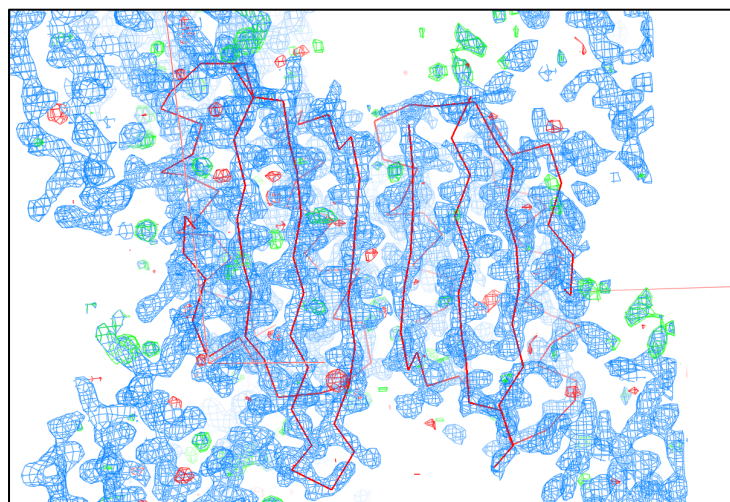


**Figure 4.3.4**: Traced main-chains are shown as ribbons (red). RelA$_{Ec}$ ACT dimer model with electron densities as observed after molecular replacement ($2F_o$-$F_c$ densities at 1.5 σ above the mean are shown in blue; $F_o$-$F_c$ densities at 3 σ above the mean are shown in green).

### 4.3.4 Analysis of the protein crystals

In order to further characterize the cleavage, dissolved crystals were analyzed by SDS-PAGE. The analysis revealed a fragment of approximately 9 kDa that could be interpreted as a monomeric ACT from RelA$_{Ec}$ (Figure 4.3.5).
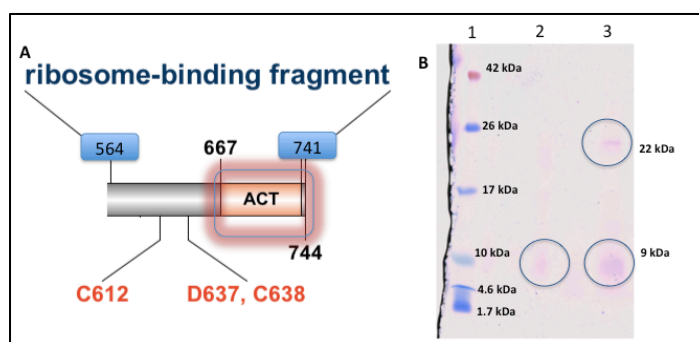


**Figure 4.3.5:** (A) Domain organization of RelA$_{Ec}$564-744. (B) SDS-PAGE analysis from RelA$_{Ec}$564-744 protein crystals (Lane 1: marker proteins with apparent molecular masses of 42 (most upper band), 26, 17, 10, 4.6, 1.7 kDa (lowest band); Lane 2: washed and dissolved crystals; Lane 3: dissolved crystals with protein drop).

### 4.3.5 Quality of the models

Crystals were of spacegroup P2₁, and contained a dimer in the asymmetric unit. The structure of RACE 1 was fully refined at 2.0 Å resolution and that of RACE 2 at 2.5 Å. The overall geometry of the models were very good, each with 98 % of the residues in the most favored regions of the Ramachandran plot and 2 % in additionally allowed regions.

### 4.3.6 The RelA$_{Ec}$ ACT monomer contains a tandem of ferredoxin-like βαββαβ motifs

The ACT domain has the archetypical βαββαβ ferredoxin fold (residues 664–742) (Figure 4.3.6 A, see below). The arrangement of secondary structure elements along the chain is β1–α1–β2–β3–α2–β4. Strand β4 is twisted with respect to β3 (Figure 4.3.6 B, see below). Of the two residues linking β3 and β4, Gly678 is highly conserved. Strands β2, β3, and β4 are almost equal in length and hydrogen-bonded together with antiparallel segment of β-sheets. The ferredoxin-like fold contains a well-defined hydrophobic core. The overall fold is stabilized by an extensive network of hydrogen bonds and polar interactions typical of α/β structures, together with hydrophobic interactions confined to hydrophobic cores within each domain.
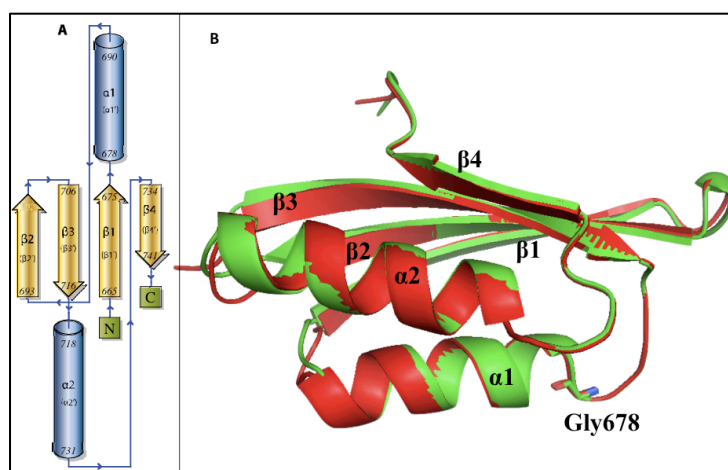


**Figure 4.3.6:** (A) Secondary-structure topology of RelA$_{Ec}$ ACT. (B) Crystal structure of RelA$_{Ec}$ ACT, monomers superimposed showing the overall fold with the βαββαβ module.

### 4.3.7 Dimer organization

Dimerization of RelA$_{Ec}$ ACT involves interactions between ACT monomer 1 and ACT monomer 2, making a large sheet of eight strands with four helices on one side of the sheet. The two monomers in the asymmetric unit arrange in a head-to-tail homodimer with an interface between the β-sheets (Figure 4.3.7 A & B, see below). The total surface area buried at the monomer-monomer interface is 1440 Å$^2$. The β2 strands from each ACT domain contribute to the interactions across the dimerization interface, including 9 hydrogen bonds but no salt-bridges. Direct hydrogen bonds, water-mediated hydrogen bonds, and Van der Waals interactions between hydrophobic side-chains contribute to the stability of the homodimer. The residues involved in the hydrogen bonds are Thr684, Leu695, Val697, Ser699, and Ser701 (Table 4.12, see below). Other residues including Ser677, Gly678, Leu680, Arg681, Thr684, Thr685, Ala688, Val694, Leu695, Gly696, Val697, Ala698, Ser699, Arg700, and Ser701 contribute to non-bonded interactions across the dimer interface.

**Table 4.12:** List of hydrogen bonds involved in RelA$_{Ec}$ ACT dimerization

| ACT Monomer 1 (Chain A) | | | ACT Monomer 2 (Chain B) | |
|---|---|---|---|---|
| Atom | Residue | Distance (Å) | Atom | Residue |
| Oγ1 (D) | Thr684 | 3.32 | Oγ1 (A) | Thr684 |
| Oγ1 (A) | Thr684 | 3.32 | Oγ1 (D) | Thr684 |
| O (A) | Leu695 | 3.00 | N (D) | Ser701 |
| N (D) | Val697 | 3.15 | O (A) | Ser699 |
| O (A) | Val697 | 2.89 | N (D) | Ser699 |
| N (D) | Ser699 | 2.80 | O (A) | Val697 |
| O (A) | Ser699 | 3.16 | N (D) | Val697 |
| Oγ (A) | Ser699 | 3.19 | N (D) | Val697 |
| N (D) | Ser701 | 2.84 | O (A) | Leu695 |

(D = donor; A= acceptor)
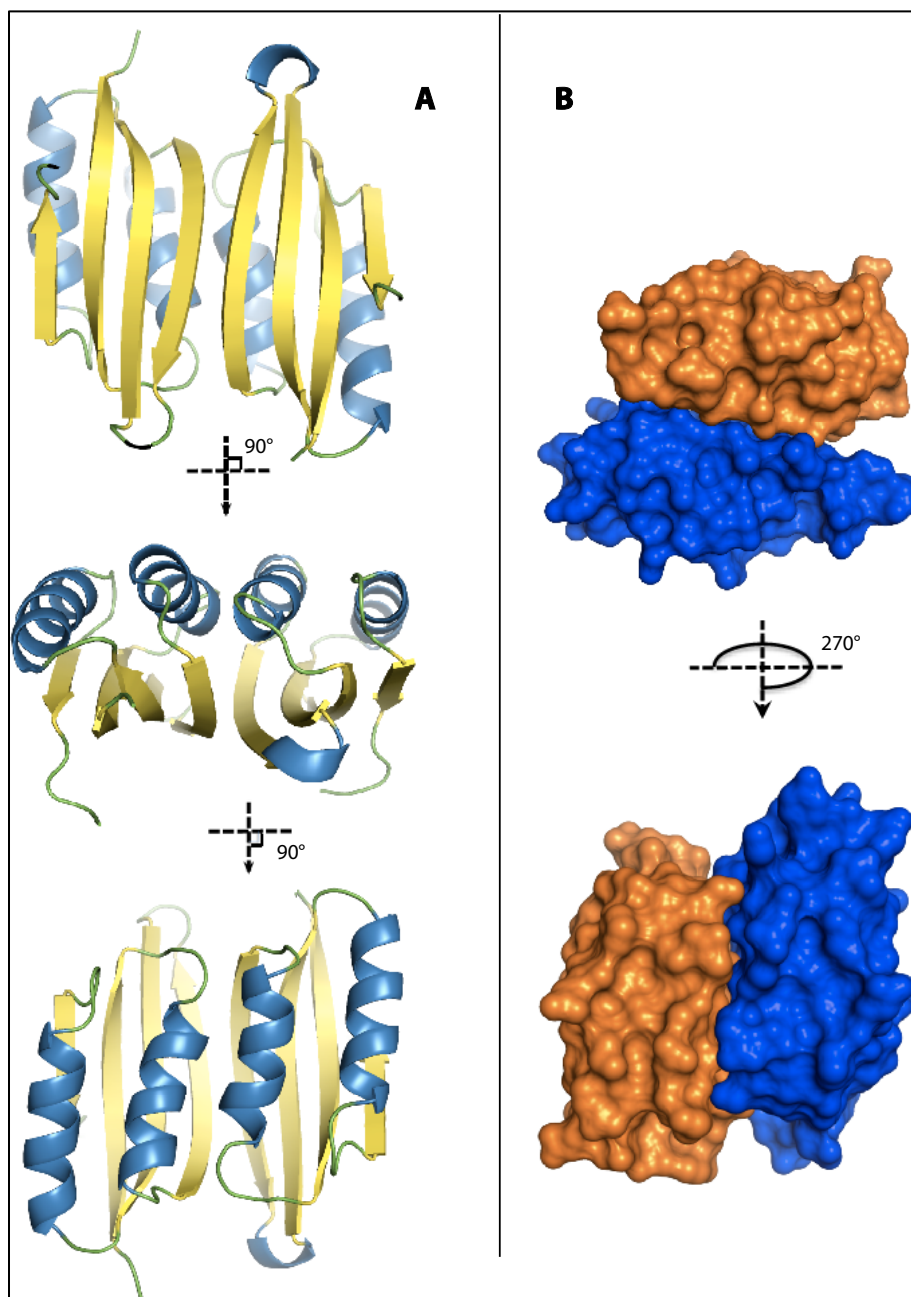
**Figure 4.3.7:** Dimer structure of RelA$_{Ec}$ ACT. (A) The RelA$_{Ec}$ ACT dimer structure is rotated by approximately 90° for displaying the 4 helices and the 8-stranded sheet. (B) Surface representation of the dimer, approximately rotated by 270°.

### 4.3.8 Ligand-binding site of the ACT domain

A highlight of the ACT domain structure is the observation of the effector-binding site at the interface between the two ferredoxin-like domains, as observed in the typical regulatory ACT domain structures of 3-phosphoglycerate dehydrogenase (Figure 4.3.8 A, see below), aspartate kinase, threonine deaminase, and prephanate dehydratase. Surprisingly, the initial electron density maps of the 2.5 Å RelA$_{Ec}$ ACT crystal structure from RACE 2 displayed unknown electron density (F$_o$-F$_c$) for two small molecules in the dimer interface (Figure 4.3.8 B & 4.3.9, see below). The appearance of the ligand-binding site in RelA$_{Ec}$ ACT is analogous to other effector binding sites of ACT domain-containing proteins. Moreover, the presence of this unknown density supports that RelA$_{Ec}$ binds small-molecule ligands, as typical ACT-like domain-containing proteins do.

Even though both RACE 1 and RACE 2 were crystallized under similar conditions, the protein purification batches used for crystallization experiments were different. Also, the RACE 1 crystal was initially soaked with KI/I$_2$ solution and washed in mother liquor for preliminary experimental phasing trials. Hence, it is likely that the 2.0-Å crystal structure lost the effector molecules during the soak procedure. It can be assumed that the small-molecule ligand from the *E. coli* host system was initially co-purified with RelA$_{Ec}$564-744, as no suitable compound was present during purification or crystallization of the protein that can be modeled into the unknown density for the ligands.
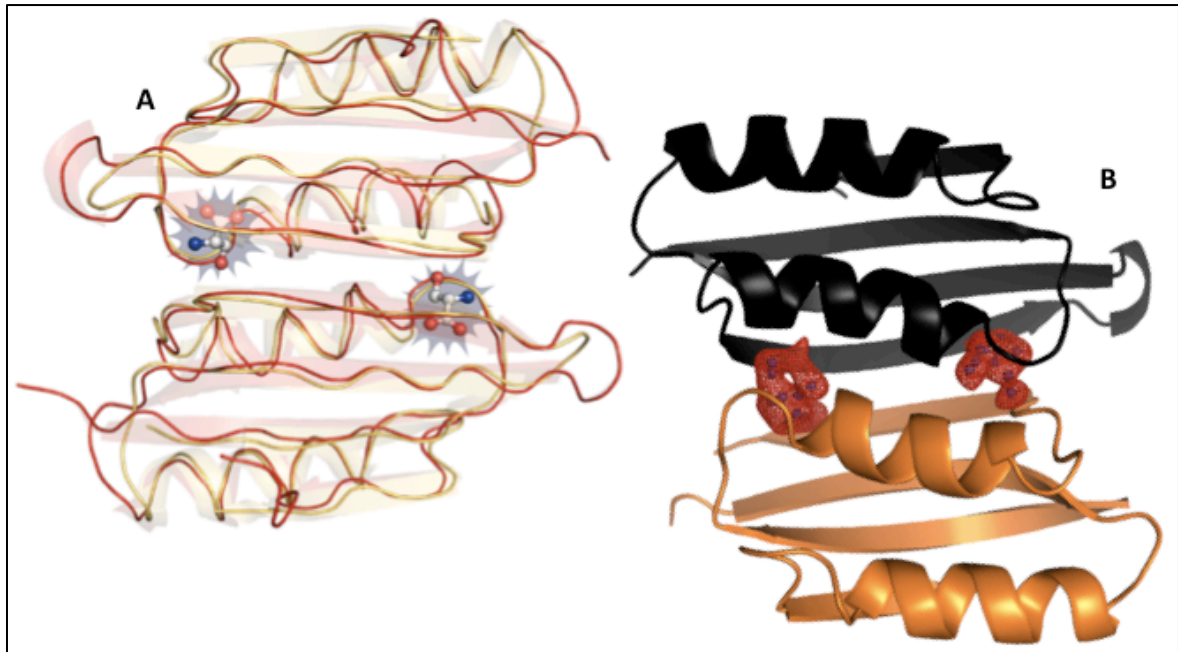
**Figure 4.3.8:** Location of the small-molecule binding site: (A) Superimposition of the ACT domains of $RelA_{Ec}$ (red) and 3-phosphoglycerate dehydrogenase (magenta) shown as Cα trace. The 3-phosphoglycerate dehydrogenase effector ligand, serine, is shown (balls and sticks) in the proposed binding site of $RelA_{Ec}$ ACT and the observed effector-binding site of 3-phosphoglycerate dehydrogenase, respectively. (B) Crystal structure of the $RelA_{Ec}$ ACT dimer (RACE 2) displaying $F_o$-$F_c$ density (red, contoured at 3 σ above the mean) at the small-molecule binding site.
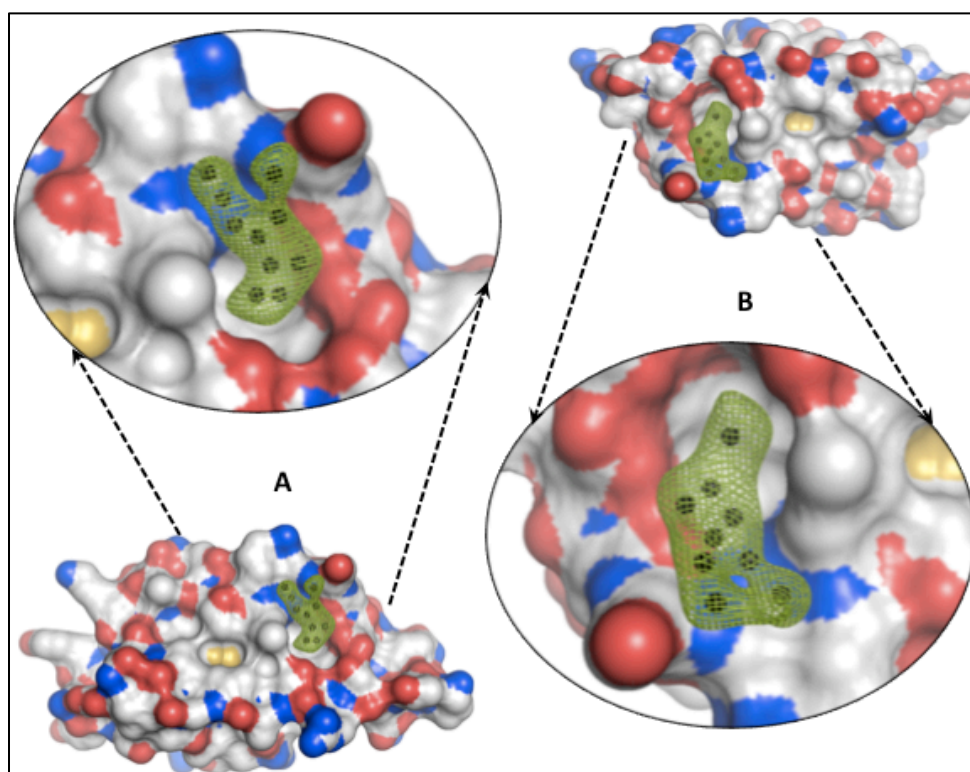
**Figure 4.3.9:** Surface representation of ACT monomer 1 (A) and monomer 2 (B) with the respective $F_o$-$F_c$ maps (green, contoured at $3\sigma$ above the mean) for the unknown small-molecule ligand (represented as black spheres).

### 4.3.9 Binding mode for the small-molecule ligand

An investigation of the binding site harboring the unknown density revealed the binding mode of the small-molecule ligand. The unknown density together with the superimposition of the RelA$_{Ec}$ ACT onto the archetypical ACT domain of 3-phosphoglycerate dehydrogenase in complex with serine [Schueller et al., 1995; PDB ID: 1PSD] allowed to locate putative small molecule-binding sites in each RelA$_{Ec}$ ACT molecule. Mostly hydrophobic residues form the observed putative small-molecule-binding pocket. In order to approximately position a small-molecule ligand, sequence variations between 3-phosphoglycerate dehydrogenase and RelA$_{Ec}$ ACT around the effector-binding site have to be considered. The carboxylate group of the ligand, serine, in 3-phosphoglycerate dehydrogenase is buried in the site with both carboxyl oxygen atoms pointing to His344. The equivalent region in the RelA$_{Ec}$ ACT

contains only the non-polar residues Ala673, Leu679 and Leu680. Hence it is probable that a small molecule containing carboxylate group must be rotated in order to place a carboxylate group near polar residues and a non-polar moiety in the non-polar environment. A probable non-polar moiety of the ligand could be fitted into a hydrophobic pocket formed by hydrophobic residues (Ala673, Leu679, Leu680, Ala708, and Ile710). An additional hydrogen bond from conserved Ser701 could provide further stabilization to the bound small molecule in this orientation (Figure 4.3.10). Moreover, the presence of small molecule-ligands bridge the ACT dimer interface by hydrogen bonds to atoms in both molecule.
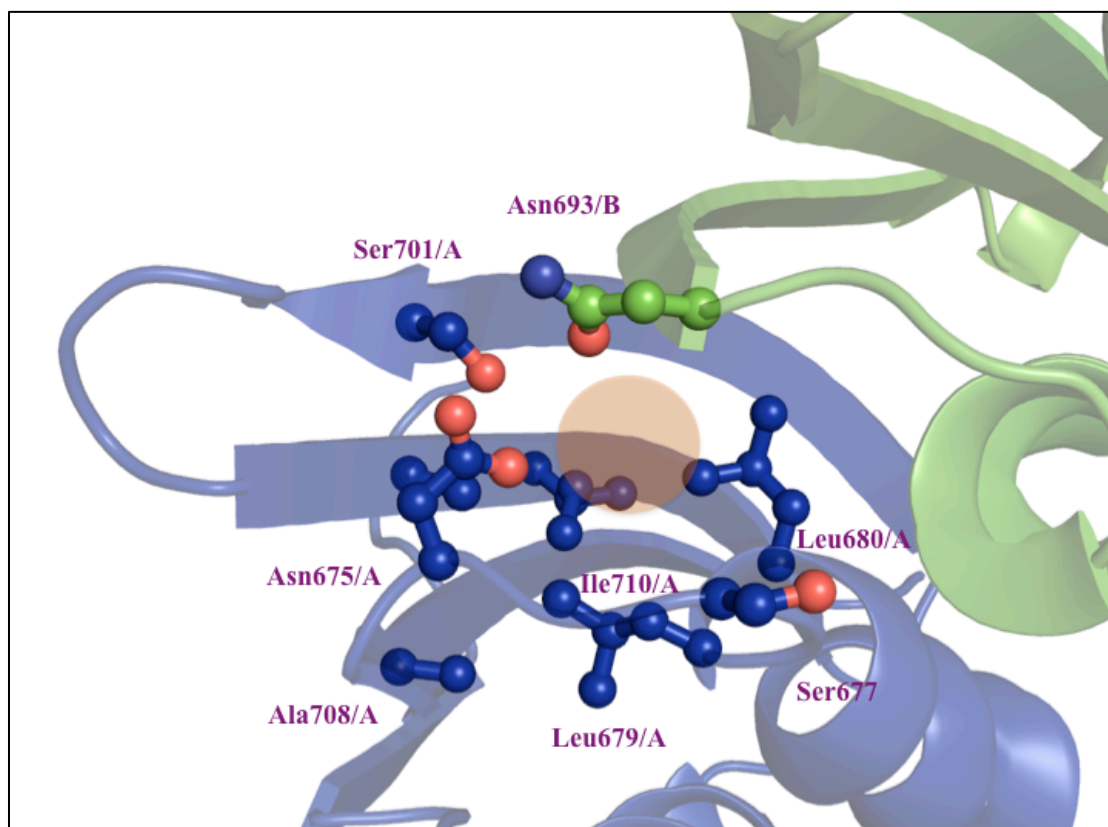


**Figure 4.3.10:** The RelA$_{Ec}$ ACT dimer (monomer A in blue and monomer B in green) showing a small-molecule ligand binding site. Associated residues are displayed as balls & sticks. A pale transparent circle represents the core site for the ligand.

**4.3.10 The RelA$_{Ec}$ ACT domain shares structural similarity with other proteins**

**4.3.10.1 Homology to other regulatory ACT domains**

A structural similarity search of the ACT domain of RelA$_{Ec}$ using the DALI server [Holm and Rosenström, 2010] found ACT domains in several different proteins with high Z-scores and low rmsd values. The results show that the ACT domain of RelA$_{Ec}$ is homologous to several classes of proteins containing an ACT-like domain [Chipman and Shaanan, 2001] such as the regulatory domains of metabolic enzymes such as 3-phosphoglycerate dehydrogenase [Schueller et al., 1995], ATP phosphoribosyltransferase [Cho et al., 2003], phenylalanine hydroxylase [Kobe et al., 1999], threonine deaminase [Gallagher et al., 1998], aspartate kinase [Mas-Droux et al., 2006], prephanate dehydratase [Tan et al., 2007], and acetohydroxy acid synthase. The associated catalytic domains of these enzymes are completely different and their structures display a remarkable diversity in how the domains associate. For example, 3-phosphoglycerate dehydrogenase, acetohydroxy acid synthase, and the C-terminal regulatory domain of NikR share a common structural topology with RelA$_{Ec}$ ACT. Also, they share a similar quaternary structure consisting of two protein monomers, and nearly identical positions for binding of their respective allosteric ligands. In contrast, phenylalanine hydroxylase has a different quaternary organization but its ligand (phenylalanine) has been proposed to bind in a similar mode to the ligand (serine) in 3-phosphoglycerate dehydrogenase. Therefore, it is rather difficult to generalize how the ACT domains regulate enzymatic function.
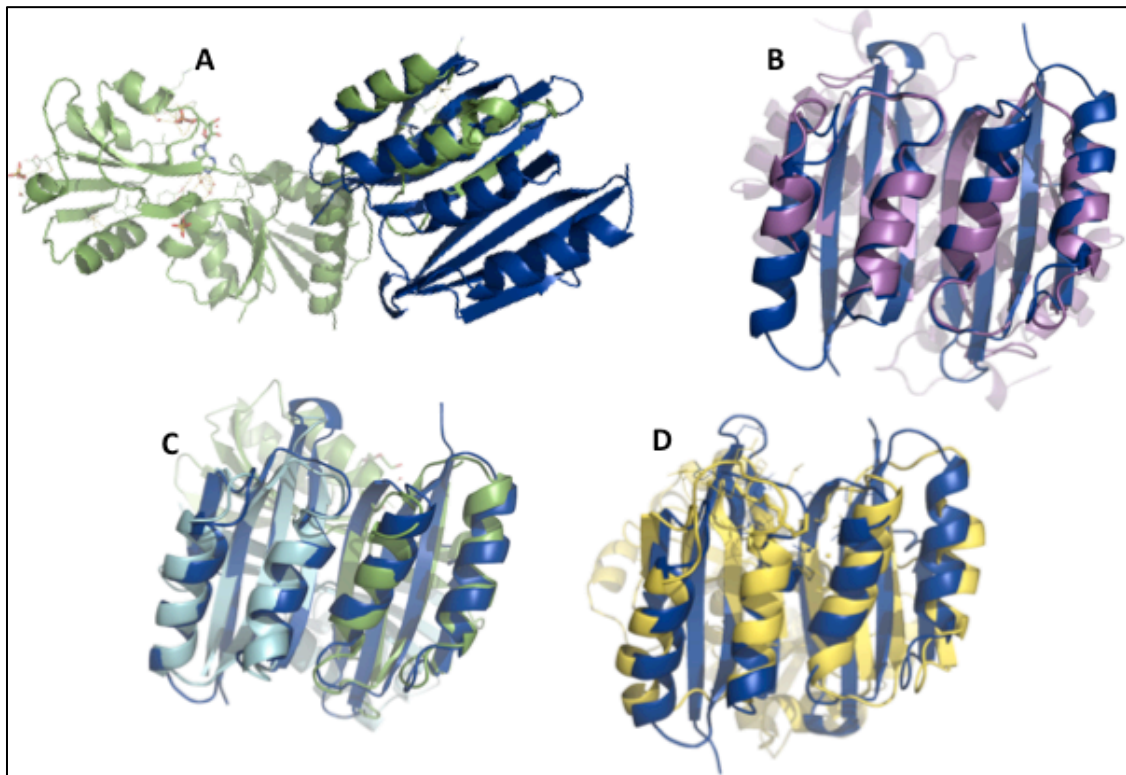
**Figure 4.3.11:** Superimposition of the ACT domains of RelA$_{Ec}$ (blue) with (**A**) ATP phosphoribosyl transferase (PDB ID: 1NH8; Cho et al., 2003), (**B**) AF1403 Probable metabolic regulator (PDB ID:1Y7P; unpublished), (**C**) acetohydroxyacid synthase isozyme III (PDB id: 2F1F; Kaplun et al., 2006), (**D**) TyrR transcription factor (PDB id: 2JHE; Verger et al., 2007).
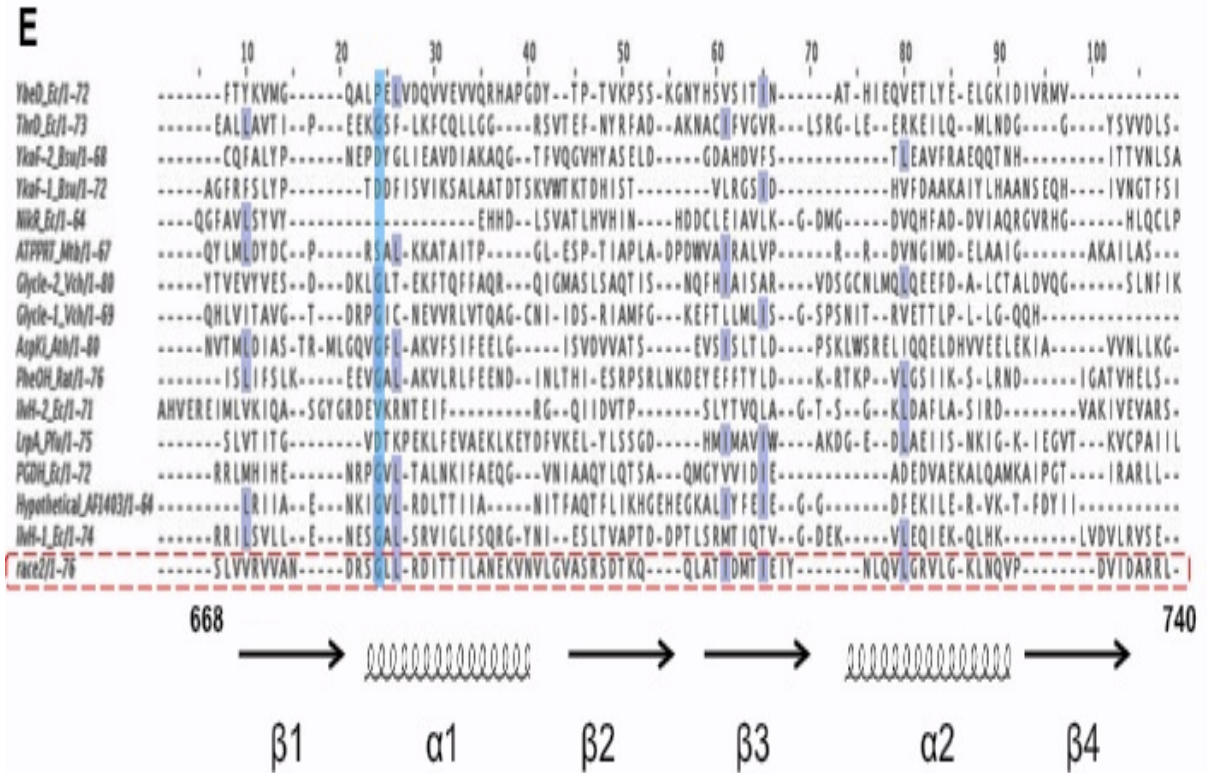
**(E)** Mutiple sequence alignment of selected (structurally known) ACT domains (coloring based on sequence identity). The sequences are aligned with regard to residue type and secondary structure. The blue colored vertical column represents the highly conserved Gly678 of RelA$_{Ec}$. The red-dotted rectangular box represents RelA$_{Ec}$ ACT domain residues. The black arrows represent β-strands, and the springs represent α-helices placed below their respective residue range. The protein abbreviations are: PGDH, D-3-phosphoglycerate dehydrogenase; IlvH, the regulatory subunit of acetohydroxyacid synthase; PheOH, phenylalanine hydroxylase; AspKi, aspartate kinase; Glycle, Glycine-cleavage system transcription regulator; ATPPRT, ATP-phosphoribosyltransferase; NikR, NikR transcription regulator; YbeD, YbeD protein; YkoF, YkoF thiamine binding protein; ThrD, threonine deaminase; LrpA and Lrp, Lrp transcription regulators; race, RelA$_{Ec}$ ACT; The species abbreviations are: Ec, *E. coli*; rat, *Rattus norvegicus*; Ath, *Arabadopsis thaliana*; Vch, *Vibrio cholerae*; Mtb, *Mycobacterium tuberculosis*; Bsu, *Bacillus subtilis*; Pfu, *P. furiosis*.

111

### 4.3.10.2 Analogy to regulatory RAM domains

The secondary structural topology of the $RelA_{Ec}$ ACT domain also matches the regulatory domain of LrpA, a representative of the leucine-responsive regulatory protein (Lrp) family of transcription factors (Figure 4.3.12). The LrpA C terminal domain serves as the archetype for the RAM domain (**R**egulation of **A**mino acid **M**etabolism) [Ettema et al., 2002]. The topological and functional similarities between these regulatory domains (ACT and RAM) suggest a common mechanism used to propagate ligand-binding cues to the contiguous catalytic protein domains.
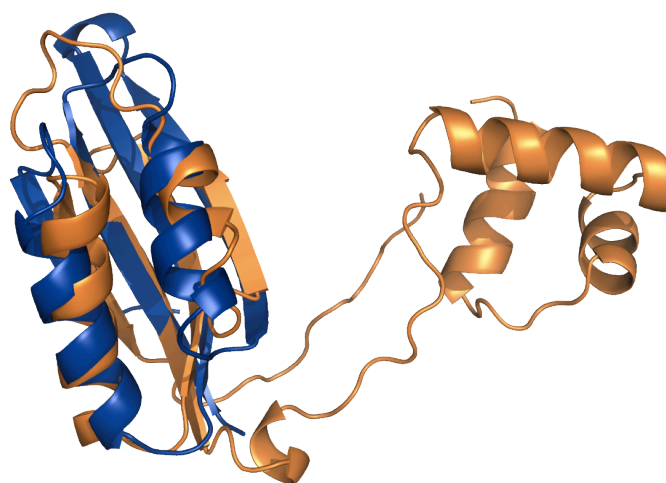


**Figure 4.3.12:** Superimposition of the ACT domain monomer of $RelA_{Ec}$ (blue) with LrpA (PDB ID: 2QZ8; Reddy et al., 2008) (orange).

### 4.3.10.3 Analogy to nucleotide diphosphate kinase

The $RelA_{Ec}$ ACT shares structural similarity to nucleoside diphosphate kinase (Ndk). Ndk enzyme catalyzes the exchange of γ-phosphate group from nucleoside triphosphates to nucleoside diphosphates. Superimposition of the Ndk monomer with the $RelA_{Ec}$ ACT monomer gives an rms deviation of 2.9 Å (Figure 4.3.13). Although the similarity exists in polypeptide conformation among these proteins, the analogy does not include the small molecule-ligand binding sites. A study in *Pseudomonas aeruginosa* revealed that AlgR2, an enzyme responsible for the biosynthesis of exopolysaccharide alginate, positively regulates two key enzymes involved in the

energy metabolism such as Ndk and succinyl-CoA synthetase [Schlictman et al., 1994]. Alginate protects the bacteria from adverse environments and increases adhesion to solid surfaces. As a result, biofilms form. Terry et al., [1992] showed that the synthesis of the exopolysaccharide alginate is coregulated with polyphosphate in mucoid strains during nutrient deprivation. A related study suggests that the regulation of exopolysaccharide alginate by Ndk enhances the formation of GTP, ppGpp and polyphosphate during the (p)ppGpp metabolic cycle. Further, the study revealed that a null mutation in *algR*2 gene decelerates the levels of alginate as well as ppGpp and polyphosphate [Kim et al., 1998]. Also, it is intriguing to note that Ndk enzymes are involved in the metabolic cycle of (p)ppGpp by probably maintaining the levels of GTP and GDP. It still remains unclear how these similar domains may be related, but their similarity is interesting.



**Figure 4.3.13:** Superimposition of the ACT of RelA$_{Ec}$ (pink) onto the *E. coli* Ndk (PDB id: 2HUR; Moynié et al., 2007) (pale-blue).

### 4.3.10.4 The ACT monomer may mimic the ribosomal subunit protein S6

A more intriguing secondary structural match of RelA$_{Ec}$ ACT monomer is the 30S ribosomal-subunit protein S6. This protein also exhibits a ferredoxin-like fold, which upon superimposition with RelA$_{Ec}$ ACT monomer gives an rms deviation of 1.95 Å. A close inspection of the superimposition of a RelA$_{Ec}$ ACT dimer with S6 monomer suggests that the non-superimposed monomer of RelA$_{Ec}$ ACT might interact with S6

(Figure 4.3.14 A & B). An ACT monomer and a S6 monomer could arrange in a head-to-tail heterodimer is possible, with an interface between the β-sheets. The possible intermolecular interactions include hydrogen bonds between Leu695, Val697, and Ser699 of RelA$_{Ec}$ ACT domain and Gly43, Asp41, and Leu39 of S6, and Van der Waals interactions between hydrophobic side-chains. The S6 subunit is situated on the platform of the 30S ribosome facing the 50S ribosome [Lindahl et al., 1994; Selmer et al., 2006]. S6 together with S18 form a complex that interacts with the central domain of 16S rRNA [Stern et al., 1988; Agalarov et al., 2000] and protects a portion of 16s rRNA [Held et al., 1974]. Also, S6 protein is known to undergo unique post-translational modification through RimK modification system [Kang et al., 1989]. RimK is an L-glutamate ligase that catalyzes post-translational addition of up to four C-terminal glutamate residues to S6 [Kino et al., 2011]. Post-translational modifications in some of the ribosomal proteins play a part in enhancing translational fidelity and structural stability of the ribosome [Kade et al., 1980]. Therefore, it is possible that a RelA$_{Ec}$ could mimic or interact with S6 and perturb 30S assembly. However, recent Cryo-EM report from Agirrezabala et al. [2013] suggests that *E. coli* RelA could bind near the GTPase associated region (GAR) of *Thermus thermophilus* 70S ribosome (70S$_{Tth}$). A deletion in the C-terminal half of RelA$_{Ec}$ failed to bind to the ribosome. The presence of C-terminal half from RelA$_{Ec}$ and an uncharged tRNA to the A-site promoted efficient complex formation with the 70S$_{Tth}$. Cryo-EM data of *E. coli* 70S-RelA complex with a 14.5 Å resolution (3D-EM database ID: EMD-2373) show that approximately 80 % of the mass of RelA was partially overlapping with the binding sites for EF-Tu, EF-G and other ribosomal GTPases on 70S. The density for RelA suggests contact with 50S via L11 lobe, and a cavity formed by helices h5 and h14 of 16S rRNA. L11 lobe comprises the N-terminal domain of L11 and nucleotides 1051-1108 of 23S rRNA. RelA also contacts with acceptor stem of A-site tRNA. The uncharged tRNA binds to the A-site with an unusual conformation.
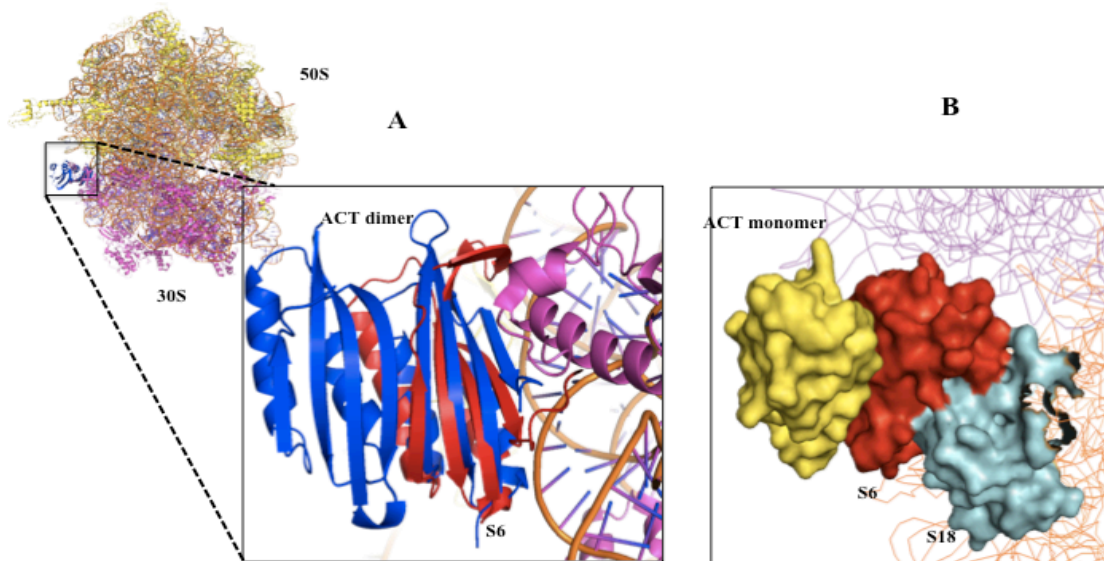
**Figure 4.3.14: (A)** Superimposition of the ACT dimer of RelA$_{Ec}$ (blue) with S6 (red) of 70S ribosome assembly (PDB id: 3I8F and 3I8G; Jenner et al., 2010), shown as cartoon. **(B)** Possible complex formation of the ACT monomer of RelA$_{Ec}$ (yellow) with S6 (red) of 70S ribosome assembly (PDB id: 3I8F and 3I8G; Jenner et al., 2010) (S18 in blue), shown as surface representation.

### 4.3.11 Conclusions

According to Gropp et al. [2001], RelA$_{Ec}$ activation is controlled by its oligomerization state. RelA$_{Ec}$ is inactive in its oligomeric state; upon amino-acid starvation, the dissociation of the oligomer leads to activation of RelA$_{Ec}$. They also proposed that instead of dissociation, a change in the conformation of the RelA$_{Ec}$ oligomer could occur during amino-acid starvation. RelA$_{Ec}$ forms homo-oligomers through its C-terminal half with the involvement of Cys612, Asp637, and Cys638. Despite lacking Cys638, Cys612 and Asp637, the crystal structure of RelA$_{Ec}$ ACT (residues 664-741) from this study displays strong and stable dimerization. This suggests that the ACT domain from the C-terminal domain of RelA$_{Ec}$ alone is sufficient to promote RelA-RelA interactions.

Most of the ACT domain-containing proteins interact with free amino-acids and are involved in some aspect of regulation of amino-acid metabolism [Chipman and Shaanan, 2001; Grant et al., 2006]. In a nutrient rich environment, free amino-acids are present in excess in the cytosol and it is likely that any amino-acid has the access

to the ACT domain. Hence, the binding of an amino-acid ligand to the ACT domain might serve a purpose of negative regulation rather than a positive regulation for RelA activation. Upon amino-acid deprivation, uncharged tRNAs bind at the A site of the ribosome and stalling translation. In this case, limited or no free amino-acids are available in the cytosol. This might influence the bound ligand from the ACT domain to release or exchange to activate RelA. The presence of the unknown electron density in the crystal structure of RelA$_{Ec}$ ACT from this study suggests that the RelA$_{Ec}$ dimer can bind a small-molecule ligand, a probable effector, which might control RelA$_{Ec}$ activity. Hence, it is possible that an aminoacid or a stable intermediate in an aminoacid metabolism might bind RelA$_{Ec}$ ACT and acts as an effector ligand in the regulation of the stringent metabolic pathway.

Thus, the crystal structure of RelA$_{Ec}$ ACT dimer opens the way for understanding the RelA$_{Ec}$ oligomerization and activation. Also, several protein families distantly related to ACT domain are linked through striking structural similarity. Further analyses of these homologous relationships and possible functions might clarify the regulation of the RelA enzyme in greater detail.

# Chapter 5. Synopsis

## 5.1 Summary

The $Rel_{Seq}385$ was successfully purified and crystallized. Crystal structures of $Rel_{Seq}385$ in complex with GTP, guanosine 5'-(β,γ-imido)triphosphate (GppNHp), ppGpp, and with the inhibitory compounds (10) and (15) were determined by molecular replacement using the previously published structure of $Rel_{Seq}385$ as a search model. The structures of $Rel_{Seq}385$ in complex with triphosphate substrates revealed alternative binding modes for the acceptor substrate of (p)ppGpp synthesis. The structures of $Rel_{Seq}385$ in complex with triphosphate substrates and ppGpp do not only reveal the precise binding modes of substrate and product of the (p)ppGpp synthesis reaction, but also uncover a surprising plasticity of the synthetase and hydrolase active site that seems to be independent of interdomain crosstalk. Comparative analyses of the catalytic domains from the individual monomers of all the $Rel_{Seq}385$ complexes revealed that each of the monomers displayed reciprocal activity states (e.g. hydrolase-ON/synthetase-OFF) with exception of complex III molecule 2, which displays an intermediate state in both domains. A plausible model for pyrophosphate transfer through a pentacoordinated transition state is predicted from the available $Rel_{Seq}385$ complex structures. These structural investigations suggest that ppGpp analogues can be used as structural probes in studying the regulation of (p)ppGpp catalysis. These $Rel_{Seq}385$ complex structures provide templates that will aid the design of (p)ppGpp -synthetase or -hydrolase inhibitors. Additionally, anomalous X-ray scattering and atomic absorption spectroscopy revealed a $Zn^{2+}$ ion in the hydrolase active site of $Rel_{Seq}385$ instead of the $Mn^{2+}$ ion that has traditionally been reported to be essential for the hydrolase activity. Based on these results, a model for (p)ppGpp hydrolysis is proposed that depends on two metal ions ($Zn^{2+}$ and $Mn^{2+}$) present in the hydrolase active site of $Rel_{Seq}$.

The C-terminal fragment $RelA_{Ec}$ 564-744 was successfully produced under heterologous conditions. After extensive optimization of crystallization conditions, thin plate-like single crystals were obtained. A modified poly-alanine model of the ACT domain from 3-phosphoglycerate dehydrogenase served as an initial search model. Subsequent modification of the coordinate set (truncating two surface loops of

117

the ACT domain) yielded an enhanced search model that allowed structure determination using a 2-Å resolution dataset in spacegroup P2$_1$. In contrast to the well-defined ACT domain, no electron density for residues 564-664 was visible, suggesting that these residues were cleaved off during crystallization. SDS-PAGE analysis of the dissolved crystals supported that cleavage has occurred. The ACT monomer consists of an archetypical βαββαβ ferredoxin fold. Furthermore, the crystal packing revealed that the RelA$_{Ec}$ ACT forms homodimers. The RelA$_{Ec}$ ACT dimer makes a long sheet of eight strands with four helices on one side of the sheet. The presence of unknown electron densities within the dimer interface supports that RelA$_{Ec}$ binds a small molecule ligand. RelA$_{Ec}$ ACT shares similarity with other regulatory ACT domains and a RAM domain  (**R**egulation of **A**mino acid **M**etabolism). Interestingly, RelA$_{Ec}$ ACT shares structural similarity to nucleoside diphosphate kinase (Ndk). Furthermore, RelA$_{Ec}$ ACT also shares structural similarity with the 30S ribosomal subunit protein S6 and therefore might interact with the ribosome by forming heterodimers with S6. The possibility of heterodimer formation of RelA$_{Ec}$ with S6 has been discussed, although a recent cryo-electron-microscopy structure of the complex between *E. coli* RelA and *Thermus thermophilus* 70S ribosome suggested a binding site for RelA near the GTPase associated region [Agirrezabala et al., 2013].

## 5.2 Zusammenfassung

Rel$_{Seq}$385 wurde erfolgreich gereinigt und kristallisiert. Kristallstrukturen der Rel$_{Seq}$385-Komplexe mit GTP, Guanosin 5'-(β,γ-imido)triphosphat (GppNHp), ppGpp und den Inhibitoren (10) und (15) wurden durch molekularen Ersatz mit der veröffentlichten Rel$_{Seq}$385-Struktur als Suchmodell gelöst. Basierend auf den Rel$_{Seq}$385-Komplexstrukturen mit Nukleotidtriphosphat-Substraten konnten unterschiedliche Interaktionsmöglichkeiten des Akzeptorsubstrats der (p)ppGpp-Synthese und Rel$_{Seq}$385 identifiziert werden. Die Strukturen im Komplex mit Nukleotidtriphosphat-Substraten und ppGpp deckten nicht nur den genauen Bindungsmodus von Substrat und Produkt der (p)ppGpp-Synthesereaktion auf, sondern demonstrieren auch eine überraschende Plastizität der Synthetase- und Hydrolase-Zentren. Diese Plastizität ist offenbar unabhängig von einer Signalübermittlung zwischen Hydrolase- und Synthetase-Domäne. Eine vergleichende Analyse der Subdomänen aller verfügbaren Rel$_{Seq}$385-Moleküle ergab für jedes einzelne Molekül einen reziproken Aktivierungszustand (z.B. Hydrolase-ON/Synthetase-OFF) außer in Komplex III Molekül 2, bei dem beide Subdomänen in einem Mischzustand vorliegen. Anhand der verfügbaren Rel$_{Seq}$385-Strukturen konnte ein plausibles Modell für den Pyrophosphattransfer abgeleitet werden, bei dem ein fünfbindiger Übergangszustand eine wichtige Rolle spielt. Diese strukturbasierten Untersuchungen legen nahe, dass ppGpp-Analoge als Ausgangspunkt für das Design von (p)ppGpp-Synthetase- und -Hydrolase-Inhibitoren geeignet sind. Zusätzlich konnte mittels anomaler Röntgenbeugung und atomarer Absorptionsspektrometrie Zn$^{2+}$ im Hydrolasezentrum von Rel$_{Seq}$385 identifiziert werden anstelle des Mn$^{2+}$-ions, welches traditionellerweise als essentiell für die Hydrolase-Reaktion beschrieben wurde. Diese Untersuchungen ermöglichten die Entwicklung eines Modell zur (p)ppGpp-Hydrolyse, das auf der Anwesenheit von zwei Metallionen (Zn$^{2+}$ und Mn$^{2+}$) im Hydrolasezentrum von Rel$_{Seq}$ basiert.

Das C-terminale Fragment RelA$_{Ec}$ 564-744 wurde erfolgreich heterolog hergestellt. Nach intensiver Optimierung der Kristallisationsbedingungen konnten plättchenförmige Kristalle erhalten werden. Ein modifiziertes Alaninmodell der ACT-Domäne der 3-Phosphoglycerat-Dehydrogenase wurde als Suchmodell für den molekularen Ersatz verwendet. Durch eine darauf folgende Modifikation des Koordinatensatzes (Verkürzung zweier Oberflächenschleifen der ACT-Domäne)

konnte ein Suchmodell erhalten werden, mit dessen Hilfe die Strukturlösung bis zu einer Auflösung von 2.0 Å in der kristallographischen Raumgruppe P2$_1$ gelang. Im Gegensatz zur gut definierten ACT-Domäne war keine Elektronendichte für die Aminosäurereste 564-664 sichtbar. Dies legte eine Abspaltung der entsprechenden Reste nahe, welche anschließend durch eine SDS-PAGE-Analyse von aufgelösten Kristallen belegt wurde. Die ACT-Domäne weist eine typische βαββαβ-Ferredoxin-Faltung auf. Innerhalb des Kristalls bilden zwei ACT-Domänen ein stabiles Homodimer. Das RelA$_{Ec}$-ACT-Dimer besteht aus einem langen, 8-strängigen Faltblatt und vier Helices, die sich alle auf einer Seite des Faltblattes befinden. Die Anwesenheit einer Region mit hoher Elektronendichte im Dimerisierungsbereich von RelA$_{Ec}$ deutet auf die Bindung eines kleinen Moleküls hin. Strukturell ähnelt RelA$_{Ec}$-ACT bekannten regulatorischen ACT-Domänen und einer RAM-Domäne (**R**egulation of **A**mino acid **M**etabolism). Interessanterweise besitzt RelA$_{Ec}$-ACT ebenfalls strukturelle Ähnlichkeit zur Nukleosiddiphosphat-Kinase (Ndk). Schließlich zeigt RelA$_{Ec}$-ACT ebenfalls strukturelle Ähnlichkeit zum S6 Protein der ribosomalen 30S Untereinheit und ermöglicht so eventuell eine Heterodimer-vermittelte Interaktion mit dem Ribosom. Die Möglichkeit einer Heterodimer-bildung zwischen RelA$_{Ec}$ und dem S6 Protein wurde diskutiert, obwohl eine kürzlich aufgeklärte Kryoelektronenmikroskopische Struktur eines Komplex in *E. coli* RelA und dem *Thermus thermophilus* 70S Ribosomalen darauf hindeutete, dass eine Bindungstelle für RelA sich nahe an der GTPase assozierten Region befindet.

# Chapter 6. Appendix

## 6.1 Abbreviations

| | |
|---|---|
| AAS | atomic absorption spectroscopy |
| aa-tRNA | aminoacyl tRNA |
| ACT | **A**spartate kinase, **C**horismate mutase and **T**yrA |
| ACP | acyl carrier protein |
| AHLs | acylhomoserine lactones |
| AMP | adenosine 5'-monophosphate |
| ATP | adenosine 5'-triphosphate |
| *B. subtilis* | *Bacilus subtilis* |
| cAMP | 2', 3'-cyclic adenosine 5'-monophosphate |
| C3HB | central 3-helix bundle |
| DNA | deoxyribonucleic acid |
| DLS | dynamic light-scattering |
| *E. coli* | *Escherichia coli* |
| EF-G | elongation factor G |
| EF-Ts | elongation factor Ts |
| EF-Tu | elongation factor Tu |
| ETAAS | electrothermal atomic absorption spectroscopy |
| EHEC | enterohemorrhagic *Escherichia coli* |
| EP | experimental phasing |
| ESI FT-ICR | Electrospray Fourier transform ion cyclotron resonance |
| GAR | GTPase associated region |
| GDP | guanosine 5'-diphosphate |
| GFAAS | graphite furnace atomic absorption spectroscopy |
| GppNHp | guanosine 5'-($\beta,\gamma$-imido)triphosphate |
| GST | glutathione S-transferase |
| GTP | guanosine 5'-triphosphate |
| IF2 | initiation factor 2 |
| LEE | locus of enterocyte effacement |
| MALDI-LIN-TOF | Matrix-assisted laser desorption and ionization-linear mode-time of flight |
| MR | molecular replacement |
| MS | mass spectrometry |
| mRNA | messenger ribonucleic acid |
| Ndk | nucleotide diphosphate kinase |
| NRPS | non-ribosomal peptide synthesis |
| NTA | nitrilotriacetic acid |
| NT-DNA | non-template deoxyribonucleic acid |
| OD | optical density |
| PEG | polyethylene glycol |
| PCD | programmed cell death |
| PCR | polymerase chain reaction |
| PMSF | phenylmethyl sulfonyl fluoride |
| poly-GlcNAc | poly-$\beta$-1,6-N-acetyl-glucosamine |
| $PP_i$ | inorganic pyrophosphate |

| | |
|---|---|
| ppGpp | guanosine 3'-5'-bis(diphosphate) |
| pppGpp | guanosine 3'-diphosphate 5'-triphosphate |
| (p)ppGpp | guanosine 3'-5'-bis(diphosphate) and guanosine 3'-diphosphate 5'-triphosphate |
| PRPP | 5-phosphoribosyl-1-pyrophosphate |
| RAM | regulation of amino-acid metabolism |
| RelA$_{Ec}$ | *Escherichia coli* RelA |
| Rel$_{Msm}$ | *Mycobacterium smegmatis* Rel |
| Rel$_{Mtb}$ | *Mycobacterium tuberculosis* Rel |
| Rel$_{Seq}$ | *Streptococcus dysgalactiae subsp. equisimilis* Rel |
| RelA$_{Sty}$ | *Salmonella typhimurium* RelA |
| RelA$_{Tth}$ | *Thermus thermophilus* RelA |
| Rms | root-mean-square |
| RSH | RelA/SpoT homolog |
| RNA | ribonucleic acid |
| RNAP | RNA polymerase |
| rRNA | ribosomal RNA |
| SDS-PAGE | sodium dodecyl sulphate – polyacrylamide gel electrophoresis |
| SPI1 | *Salmonella* pathogenicity island 1 |
| SPI2 | *Salmonella* pathogenicity island 2 |
| SpoT$_{Ec}$ | *Escherichia coli* SpoT |
| T3SS | type-III secretion system |
| TA | toxin-antitoxin |
| TGS | **T**hrRS (threonyl tRNA synthetase), **G**TPase (Obg family GTPases), and **S**poT |
| TLS | Translation/Libration/Screw |
| tmRNA | tRNA-mRNA hybrid |
| tRNA | transfer RNA |
| *T. thermophilus* | *Thermus thermophilus* |
| UPEC | Uropathogenic *Escherichia coli* |

## 6.2 Purification and analysis of RelA$_{Ec}$
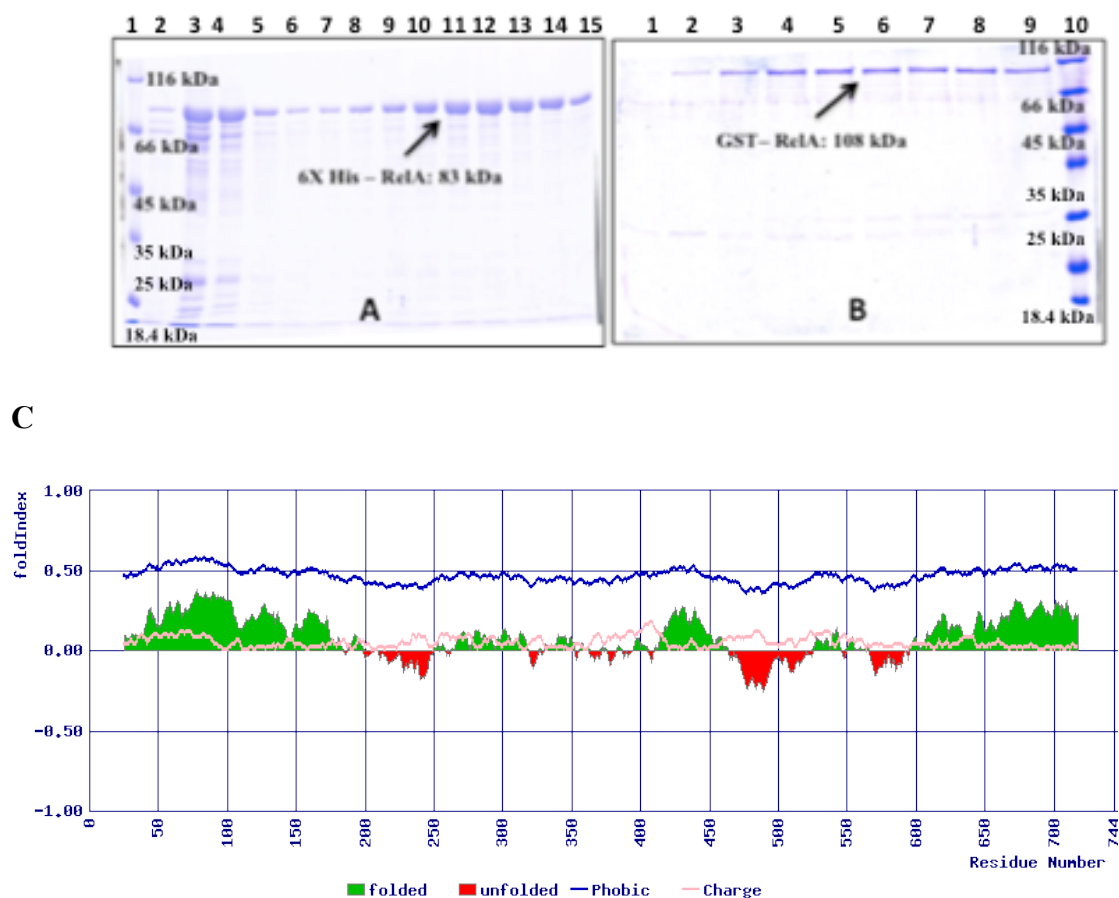


**Figure 6.3:** (**A**) Ni$^{2+}$-NTA chromatography elution profile of His-tagged RelA$_{Ec}$ fractions in SDS-PAGE; Lane 1: Marker proteins with apparent molecular masses of 116 (most upper band), 66.2, 45, 35, 25, 18.4 kDa (lowest band), Lanes 2-15: RelA$_{Ec}$ His$_6$ (83 kDa) fractions eluted with increasing imidazole concentration. (**B**) Elution profile of GST-tagged RelA$_{Ec}$ fractions in SDS-PAGE; Lanes 1-9: RelA$_{Ec}$-GST (108 kDa) fractions eluted glutathione (loaded in reverse order), Lane 2: Marker proteins with apparent molecular masses of 116 (most upper band), 66.2, 45, 35, 25, 18.4 kDa (lowest band), (**C**) Fold and disorder profile of RelA$_{Ec}$

## 6.3 RelA$_{Sty}$372-744 from *Salmonella typhimurium*

RelA$_{Sty}$372-744 (42 kDa) consists of two conserved domains, TGS and ACT. The construct carries a His$_6$ tag at the N terminus and was purified by two-step Ni$^{2+}$-NTA affinity chromatography. SDS-PAGE analysis of the desalted peak fractions showed a cleaved product of approximately 28 kDa (Figure 6.4 A). The cleavage product was confirmed as a fragment from the N-terminus, as judged by the Western blot assay with anti-His antibodies (Figure 6.4 B). The remaining cleavage product of approximately 14 kDa lacking a His$_6$-tag has been washed. However, pure desalted fractions were pooled, concentrated to a final concentration of 5 mg/ml and used for crystallization studies. Preliminary crystallization screening using the Sigma Basic and Extension screens, Nextal pH clear Screen, and Structure screen (Molecular Dimensions Ltd.) were ineffective.
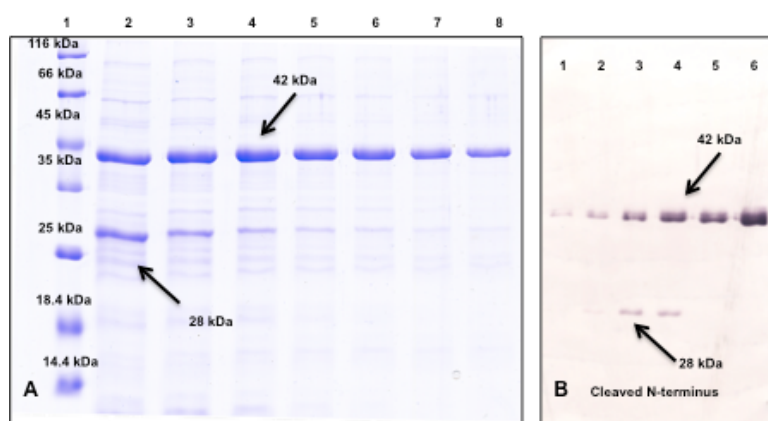


**Figure 6.4:** (**A**) Ni$^{2+}$-NTA chromatography elution profile of His$_6$-tagged RelA$_{Sty}$ 372-744 fractions in SDS-PAGE; Lane 1: Marker proteins with apparent molecular masses of 116 (most upper band), 66.2, 45, 35, 25, 18.4, 14.4 kDa (lowest band), Lanes 2-8: RelA$_{Sty}$ 372-744-His$_6$ eluents. (**B**) Western blot profile of His$_6$-tagged RelA$_{Sty}$ fractions using antiHistidine; Lanes 1-6: RelA$_{Sty}$ 372-744-His$_6$ eluents.

## 6.4 L11$_{Ec}$ analyses
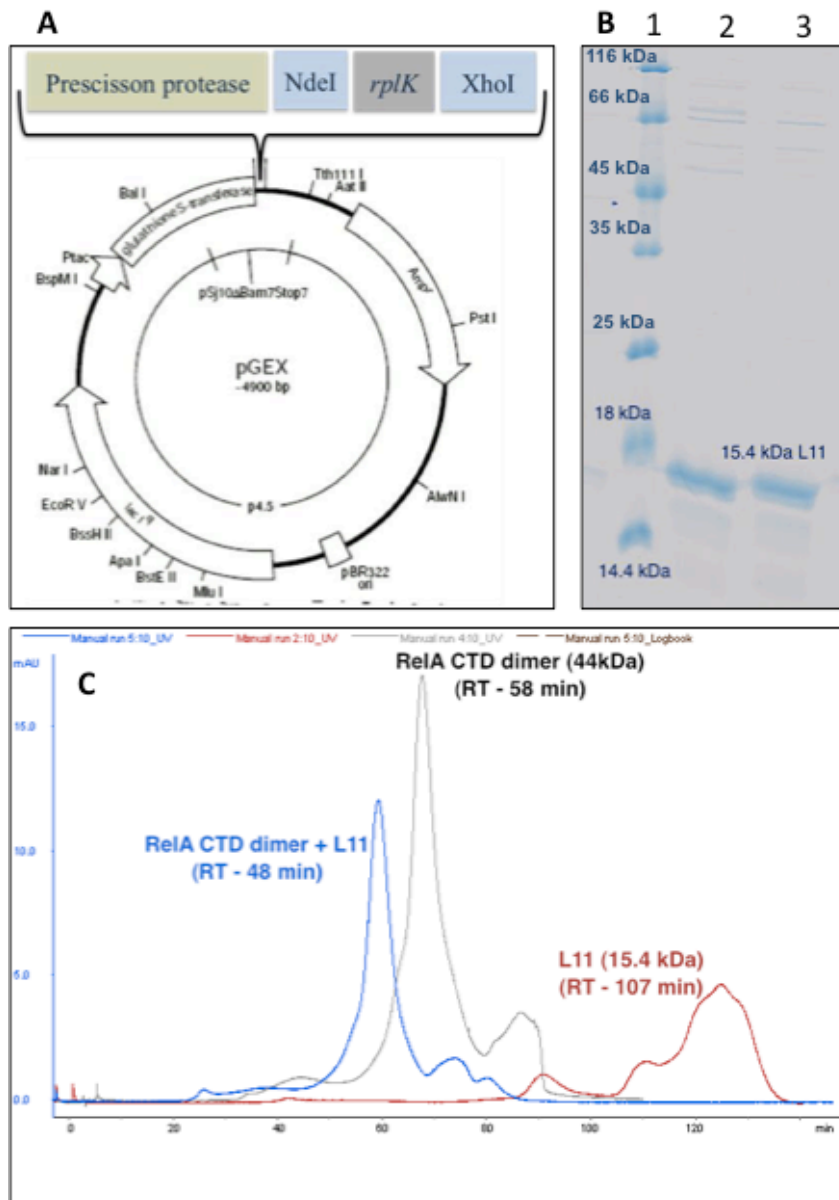


**Figure 6.5: (**A) pGEX-pre01 vector map used for cloning L11$_{Ec}$. (B) Coomassie-stained SDS-PAGE showing purified L11$_{Ec}$ after removal of the GST-tag; Lane 1: Marker proteins with apparent molecular masses of 116 (most upper band), 66.2, 45, 35, 25, 18.4, 14.4 kDa (lowest band), Lane 2: L11$_{Ec}$ eluent after GST- tag cleavage, Lane 3: L11$_{Ec}$ gel-filtered eluent, (C) Gel-filtration analysis of individual L11$_{Ec}$ (red), RelA$_{Ec}$ 564-744 (grey) and the sample containing both proteins (blue). RT- retention time.

## 6.5 ESI mass spectra of water-dialysed Rel$_{Seq}$385 protein solution
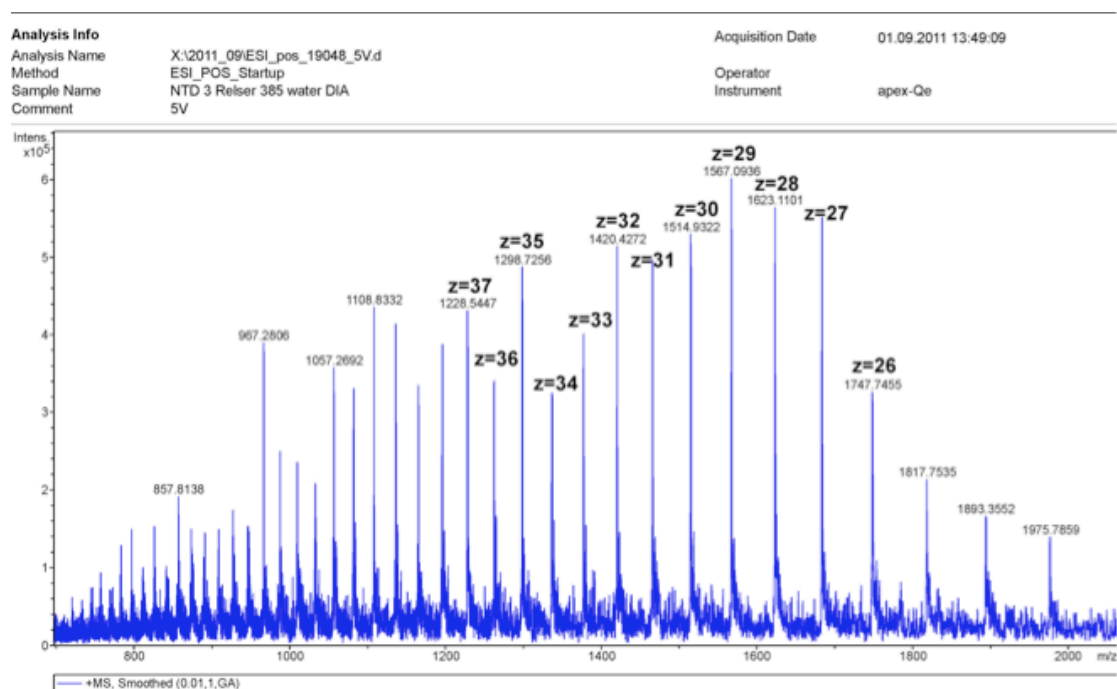


**Figure 6.9**: High-resolution ESI FT-ICR MS spectra of purified Rel$_{Seq}$385 protein sample. (**M$_{average}$ = 45417.8 ± 2.4 Da)**. Electrospray ionization Fourier transform ion cyclotron (ESI-FT-ICR) mass spectrometry was performed on intact Rel$_{Seq}$385 in the negative ion mode using an APEX QE (Bruker Daltonics, Billerica, USA) equipped with a 7-Teslas actively shielded magnet.

## 6.6 MALDI mass spectra of dissolved Rel$_{Seq}$385 protein crystals
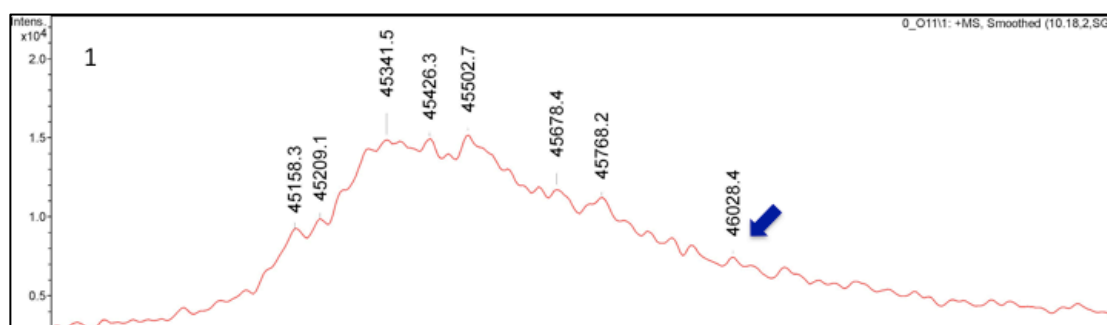


**Figure 5.10:** MALDI-TOF mass spectra of positive ions recorded with a Reflex II, Bruker-Franzen (Bremen, Germany) spectrometer in the linear mode (MALDI-LIN-TOF). Performed at 28.5 kV acceleration voltage using 2,5-dihydroxybenzoic acid as matrix. With the MALDI–TOF MS instrument information from the intact protein can be determined. However, the mass accuracy as well as the mass resolution is clearly reduced. Furthermore, non-covalent ligands are lost easier by the MALDI- than by the ESI- ionization process, which can be observed as different adduct ions (e.g.: $+Na^+$, $+K^{+,....}$ or several adducts –H+Na, -2H+2Na,….). (**1**) Red, shows overview spectra from dissolved Rel$_{Seq}$385 protein crystals. The mass of the main peak is not significantly changed in comparison to the sample in section **6.9**. The asymmetric distribution to higher masses is caused by adducts or ligands. Peak corresponding to blue arrow signify a Rel$_{Seq}$385 monomer (**M = 46028.4 Da)** with a ligand of mass **602.4 ± 2.4**, which corresponds to the approximate mass of ppGpp.

## 6.7 Rel$_{Seq}$385 and nucleotide-interaction chart (synthetase-ON conformers)

**Table 6.6** Hydrogen bond interactions between nucleotide/nucleotide analogue ligands to the **S-ON** site of Rel$_{Seq}$385 complexes

| | | Guanine Base | Rel$_{Seq}$/ HOH | Distance (Å) | Ribose/ Deoxyribose | Rel$_{Seq}$/ HOH | Distance (Å) | Phosphates/ Phosphonates | Rel$_{Seq}$/ HOH | Distance (Å) |
|---|---|---|---|---|---|---|---|---|---|---|
| **1VJ7** | **GDP** | O6 | Asn306:ND2 | 3.0 | O2' | Arg241:NH1 | 3.0 | O1B | His312:ND1 | 2.8 |
| | | N7 | Lys304:NZ | 3.0 | O2' | HOH2153 | 2.9 | O2B | Tyr299:OH | 2.9 |
| | | N1 | HOH2022 | 2.7 | O4' | Gln325:NE2 | 2.8 | | | |
| | | N2 | Ala335:O | 3.0 | | | | | | |
| | | N2 | HOH2036 | 2.9 | | | | | | |
| | | N3 | HOH2153 | 2.9 | | | | | | |
| | | | | | | | | | | |
| **C-I** | **C(10)** | O6 | Asn306:ND2 | 3.0 | | | | O2A | His312:ND1 | 3.2 |
| | | N7 | Lys304:NZ | 2.8 | | | | | | |
| | | | | | | | | O2B | Tyr299:OH | 3.0 |
| | | | | | | | | O2B | Lys304:NZ | 3.0 |
| | | | | | | | | | | |
| | | | | | | | | O2C | Arg241:NH1 | 3.0 |
| | | | | | | | | O2C | Arg241:NE | 3.0 |
| | | | | | | | | O2C | Lys243:NZ | 2.9 |
| | | | | | | | | | | |
| | | | | | | | | O1D | Arg241:NH1 | 3.0 |
| | | | | | | | | O2D | Arg241:NH1 | 3.1 |
| | | | | | | | | | | |

| | | | | | | | | | | |
|---|---|---|---|---|---|---|---|---|---|---|
| **C-II** | **C(15)** | O6 | Asn306:ND2 | 3.0 | O4' | Gln325:NE2 | 3.2 | O1B | Arg241:NH1 | 2.7 |
| | | N7 | Lys304:NZ | 2.8 | | | | O2B | Lys243:NZ | 2.5 |
| | | | | | | | | | | |
| | | | | | | | | O36 | His244:N | 3.0 |
| | | | | | | | | O36 | Ser247:OG | 3.0 |
| | | | | | | | | O31 | Lys304:NZ | 2.6 |
| | | | | | | | | O37 | Arg241:NE | 3.0 |
| | | | | | | | | | | |
| **C-III** | **ppGpp** | O6 | Asn306:ND2 | 2.9 | O2' | Gln325:NE2 | 2.8 | O1B | Tyr299:OH | 2.4 |
| | | N7 | Lys304:NZ | 2.7 | O2' | HOH47 | 3.0 | O2B | Lys304:NZ | 2.6 |
| | | N3 | HOH54 | 2.8 | O4' | Gln325:NE2 | 3.2 | | | |
| | | N1 | HOH3 | 2.8 | | | | O3D | Ser247:OG | 3.0 |
| | | | | | | | | | | |
| **C-IV** | **GppNHp** | O6 | Asn306:ND2 | 3.0 | O2' | Arg241:NH2 | 2.7 | O1A | HOH69 | 3.0 |
| | | O6 | HOH27 | 2.7 | O2' | HOH7 | 3.1 | | | |
| | | N7 | Lys304:NZ | 2.9 | O4' | Gln325:NE2 | 3.0 | O1B | Tyr299:OH | 2.5 |
| | | N2 | Ser181:OG | 3.2 | | | | O1B | Lys304:NZ | 2.8 |
| | | N2 | Ala335:O | 3.2 | | | | O2B | Lys297:NZ | 3.0 |
| | | N2 | HOH30 | 2.8 | | | | | | |
| | | N3 | HOH7 | 2.7 | | | | O1G | HOH69 | 2.8 |
| | | N1 | HOH31 | 2.7 | | | | | | |

## 6.8 Rel$_{Seq}$385 and nucleotide-interaction chart (synthetase-OFF conformers)

**Table 6.7** Hydrogen bond interactions between nucleotide/nucleotide analogue ligands to the **S-OFF** site of Rel$_{Seq}$385 complexes

| | | Guanine Base | Rel$_{Seq}$/HOH | Distance (Å) | Ribose/Deoxyribose | Rel$_{Seq}$/HOH | Distance (Å) | Phosphates/Phosphonates | Rel$_{Seq}$/HOH | Distance (Å) |
|---|---|---|---|---|---|---|---|---|---|---|
| **1VJ7** | **GDP** | O6 | Asn306:ND2 | 3.0 | O2' | Arg241:NH1 | 2.6 | O2A | His312:ND1 | 2.8 |
| | | N7 | Lys304:NZ | 3.0 | O4' | Gln325:NE2 | 2.8 | | | |
| | | N2 | Ala335:O | 2.8 | | | | O3B | Tyr299:OH | 2.9 |
| | | N2 | Ser181:OG | 3.1 | | | | O3B | Lys304:NZ | 2.4 |
| | | | | | | | | | | |
| **C-I** | **GTP** | O6 | Asn306:ND2 | 3.0 | O2' | Gln325:NE2 | 3.2 | O2B | Lys297:NZ | 3.1 |
| | | N7 | Lys304:NZ | 3.2 | | | | O2B | His312:ND1 | 2.8 |
| | | N2 | Ala335:O | 3.2 | | | | | | |
| | | N2 | Ser181:OG | 2.5 | | | | O3G | Tyr299:OH | 3.0 |
| | | | | | | | | | | |
| **C-II** | **-** | | | | | | | | | |
| | | | | | | | | | | |
| **C-III** | **GppNHp** | O6 | Asn306:ND2 | 3.2 | O2' | HOH29 | 2.5 | O1A | Lys297:NZ | 3.0 |
| | | N7 | Lys304:NZ | 2.9 | O4' | Gln325:NE2 | 2.8 | O1A | His312:ND1 | 2.4 |
| | | N3 | HOH34 | 2.7 | | | | O3A | Lys297:NZ | 3.1 |
| | | | | | | | | | | |
| | | | | | | | | O1G | Arg295:NH1 | 2.7 |
| | | | | | | | | | | |
| **C-IV** | **GppNHp** | O6 | Asn306:ND2 | 3.2 | | | | O1A | Lys297:NZ | 3.2 |

| | | | | | O2' | HOH77 | 3.1 | O1A | His312:ND1 | 2.7 |
|---|---|---|---|---|---|---|---|---|---|---|
| | N7 | Lys304:NZ | 3.2 | O4' | Gln325:NE2 | 3.1 | | | |
| | | | | | | | O1G | Lys297:NZ | 2.7 |
| | N2 | Ala335:O | 3.0 | | | | O3G | Arg295:NH2 | 2.2 |
| | N2 | HOH70 | 3.2 | | | | | | |
| | N3 | HOH1 | 2.5 | | | | | | |
| | N1 | HOH70 | 2.5 | | | | | | |

## 6.9 Nucleotides bound to Rel$_{Seq}$385, and their conformational angles chart

**Table 6.8** Comparison of conformation angles (torsion angles) observed in Rel$_{Seq}$385 complexes

| Complexes | Active-site state | Nucleotide/ Nucleotide analog | α O3'-P-O5'-C5' | β P-O5'-C5'-C4' | γ O5'-C5'-C4'-C3' | δ C5'-C4'-C3'-O3' | ε C4'-C3'-O3'-P | ζ C3'-O3'-P-O5' | χ O4'-C1'-N9-C4 | Sugar pucker C3' endo/exo |
|---|---|---|---|---|---|---|---|---|---|---|
| 1VJ7 | S-ON | GDP | 86.96 | -170.35 | 83.45 | 103.83 | | | -161.13 | C3' endo |
| | H-OFF | -- | | | | | | | | |
| | S-OFF | GDP | 80.2 | -176.44 | 88.94 | 80.2 | | | -156.71 | C3' endo |
| | H-ON | ppG2':3'p | 98.5 | 16.85 | -143 | 98.5 | | | 77.54 | C3' endo |
| | | | | | | | | | | |
| Compound (10)•GTP | S-ON | Compound (10) | 164.97 | 49.29 | 176.47 | 157.92 | -142.57 | -87.44 | -177.88 | C3' exo |
| (complex I) | H-OFF | -- | | | | | | | | |
| | S-OFF | GTP | -177.18 | -7.28 | 151.24 | 112.45 | | | -148.8 | C3' endo |
| | H-ON | -- | | | | | | | | |
| | | | | | | | | | | |
| Compound (15) | S-ON | Compound (15) | 134.75 | 179.05 | 167.74 | 161.69 | -105.64 | -61.57 | -176.65 | C3' exo |
| | H-OFF | -- | | | | | | | | |
| (complex II) | S-OFF | | | | | | | | | |
| | H-ON | -- | | | | | | | | |
| | | | | | | | | | | |
| ppGpp•GppNHp | S-ON | ppGpp | 134.12 | 133.56 | 153.85 | 97.65 | -135.08 | -91.12 | -175.49 | C3' endo |
| | H-OFF | -- | | | | | | | | |
| (complex III) | S-OFF | GppNHp | 62.58 | 147.89 | 71.77 | 82.85 | | | -151.34 | C3' endo |

| | | | | | | | | | | |
|---|---|---|---|---|---|---|---|---|---|---|
| | H-ON | -- | | | | | | | | |
| | | | | | | | | | | |
| 3X-GppNHp | S-ON | GppNHp | 160.99 | 141.88 | 128.18 | 89.37 | | | -171.84 | C3' endo |
| (complex IV) | H-OFF | -- | | | | | | | | |
| | S-OFF | GppNHp | 20.56 | 170.65 | 78.47 | 83.81 | | | -154.24 | C3' endo |
| | H-ON | GppNHp | 54.22 | -79.45 | -91.93 | 86.27 | | | 80.36 | C3' endo |

## 6.10 List of structurally known metal-binding HD motif-containing proteins and their coordination geometries

| Name of the protein | Organism | PDB codes | HD motif-binding ion | Co-ordination number | Solvent-binding sites | Protein-binding sites | Ligand-binding site | shape | Second site metal ions involved in catalysis | associated PDB codes |
|---|---|---|---|---|---|---|---|---|---|---|
| | | | | | | | | | | |
| Oxetanocin-like protein | *Pyrococcus furiosus* | 1XX7 | Ni$^{2+}$ | 4 | - | 4 | - | T4 Tetrahedral | - | |
| Putative Hydrolase | *Aquifex aeolicus* | 1YNB | Zn$^{2+}$ | 5 | 1 | 3 | 1 | T5 Trigonal Bipyramidal | - | |
| BH1327 Hydrolase | *Bacillus halodurans* | 2O08 | Fe$^{3+}$ | 6 | 2 | 4 | - | T6 Octahedral | Fe$^{3+}$ | |
| dNTPase HD domain | *Enterococcus faecalis* | 2O6I | Zn$^{2+}$ | 4 | - | 4 | - | T4 Tetrahedral | - | |
| Putative Hydrolase | Streptococcus agalactiae | 2OGI | Fe$^{3+}$ | 6 | 1 | 4 | 1 | T6 Octahedral | Fe$^{3+}$ | |
| PH0347 HD | *Pyrococcus horikoshii* | 2CQZ | Ni$^{2+}$ | 4 | - | 4 | - | T4 Tetrahedral | - | |
| 5'-deoxynucleotidase YfbR | *Escherichia coli* | 2PAR | Co$^{2+}$ | 6 | 1 | 4 | 1 | T6 Octahedral | | 2PAU |
| Putative Hydrolase | *Thermotogales sp.* | 2PQ7 | Fe$^{3+}$ | 6 | 1 | 3 | 2 | T6 Octahedral | Fe$^{3+}$ | |
| YqeK ortholog Hydrolase | *Clostridium acetobutylicum* | 3CCG | Fe$^{3+}$ | 6 | 1 | 4 | 1 | T6 Octahedral | Fe$^{3+}$ | |
| Hydrolase | *Bacillus thuringiensis* | 3DJB | Mg$^{2+}$ | 4 | - | 4 | - | T4 Tetrahedral | - | |
| YedJ | *Escherichia coli* | 3GW7 | Ni$^{2+}$ | 4 | - | 3 | 1 | T4 Tetrahedral | Ni$^{2+}$ | |
| HD-domain protein | *Enterococcus faecalis* | 3IRH | Ca$^{2+}$ | 6 | 2 | 4 | - | T6 Octahedral | - | |
| PDEB1 | *Leishmania major* | 2R8Q | Zn$^{2+}$ | 6 | 2 | 4 | - | T6 Octahedral | Mg$^{2+}$ | |
| Rat PDE10 | *Rattus rattus* | 3HR1 | Zn$^{2+}$ | 5 | 1 | 4 | - | T5 Trigonal Bipyramidal | Mg$^{2+}$ | 3HQZ, 3HQY, 3HQW, 2OVY, 2OVV, 2O8H |
| Human PDE2A | *Homo sapiens* | 3ITM | Zn$^{2+}$ | 4 | - | 4 | - | T4 Tetrahedral | - | |
| Human PDE2A | | 3IBJ | Zn$^{2+}$ | 4 | - | 4 | - | T4 Tetrahedral | Mg$^{2+}$ | |
| Human PDE2A | | 3ITU | Zn$^{2+}$ | 6 | 2 | 4 | - | T6 Octahedral | Mg$^{2+}$ | |
| Human | | 1Z1L | Zn$^{2+}$ | 6 | 1 | 4 | 1 | T6 | Mg$^{2+}$ | |

| | | | | | | | | | | |
|---|---|---|---|---|---|---|---|---|---|---|
| PDE2A | | | | | | | | Octahedral | | |
| Human PDE4A | | 2QYK | $Zn^{2+}$ | 5 | 1 | 4 | - | T5 Trigonal Bipyramidal | $Mg^{2+}$ | |
| Human PDE4A | | 3I8V | $Zn^{2+}$ | 6 | 2 | 4 | - | T6 Octahedral | $Mg^{2+}$ | |
| Human PDE4B | | 1Y2J | $Zn^{2+}$ | 4 | 1 | 3 | - | T4 Tetrahedral | $Mg^{2+}$ | 1Y2H |
| Human PDE4B | | 1RO6 | $Zn^{2+}$ | 5 | 1 | 4 | - | T5 Trigonal Bipyramidal | $Zn^{2+}$ | 1ROR, 1RO9 |
| Human PDE4B | | 1F0J | $Zn^{2+}$ | 5 | 1 | 4 | - | T5 Trigonal Bipyramidal | $Mn^{2+}$ | |
| Human PDE4B | | 2QYL | $Zn^{2+}$ | 5 | 1 | 4 | | T5 Trigonal Bipyramidal | $Mg^{2+}$ | |
| Human PDE4B | | 1TB5 | $Zn^{2+}$ | 6 | 1 | 4 | 1 | T6 Octahedral | $Mg^{2+}$ | |
| Human PDE4B | | 3D3P | $Zn^{2+}$ | 6 | 2 | 4 | - | T6 Octahedral | $Mg^{2+}$ | 1XLX, 1XLZ, 1XM4, 1XMU, 1XMY, 1XN0, 1XOS, 1XOT |
| Human PDE4C | | 2QYM | $Zn^{2+}$ | 6 | 2 | 4 | - | T6 Octahedral | $Mg^{2+}$ | |
| Human PDE4D | | 1MKD | $Zn^{2+}$ | 4 | - | 4 | - | T4 Tetrahedral | $Mg^{2+}$ | |
| Human PDE4D | | 1OYN | $Zn^{2+}$ | 5 | 1 | 4 | - | T5 Trigonal Bipyramidal | $Zn^{2+}$ | |
| Human PDE4D | | 1ZKN | $Zn^{2+}$ | 5 | 1 | 4 | - | T5 Trigonal Bipyramidal | $Mg^{2+}$ | |
| Human PDE4D | | 1PTW | $Zn^{2+}$ | 5 | - | 4 | 1 | T5 Trigonal Bipyramidal | $Zn^{2+}$ | |
| Human PDE4D | | 1TB7 | $Zn^{2+}$ | 6 | 2 | 4 | - | T6 Octahedral | $Mg^{2+}$ | 1Y2B, 1Y2C, 1Y2D, 1Y2E, 1Y2K, 1XOM, 1XON, 1XOQ, 2FM0, 2FM5, 2QYN |
| Human PDE4D | | 1XOR | $Zn^{2+}$ | 6 | 1 | 5 | - | T6 Octahedral | $Mg^{2+}$ | |
| Human PDE4D | | 1TBB | $Zn^{2+}$ | 6 | 1 | 4 | 1 | T6 Octahedral | $Mg^{2+}$ | |
| Human PDE4D | | 2PW3 | $Zn^{2+}$ | 6 | 2 | 4 | - | T6 Octahedral | - | |
| Human PDE5A | | 1UDU | $Zn^{2+}$ | 4 | - | 4 | - | T4 Tetrahedral | $Mg^{2+}$ | 1UHO, 2H42, 3JWR |
| Human PDE5A | | 1T9R | $Zn^{2+}$ | 4 | - | 3 | 1 | T4 Tetrahedral | - | |
| Human PDE5A | | 1T9S | $Zn^{2+}$ | 5 | 1 | 4 | - | T5 Trigonal Bipyramidal | $Mg^{2+}$ | 3HC8, 3JWQ, 3HC8, 3BJC |
| Human PDE5A | | 1RKP | $Zn^{2+}$ | 6 | 2 | 4 | - | T6 Octahedral | $Mg^{2+}$ | 1TBF, 1UDT 1XOZ, 1XP0, 2H40,2H44, 3HDZ |

| Protein | | PDB | Metal | | | | | Geometry | Metal 2 | Related |
|---|---|---|---|---|---|---|---|---|---|---|
| Human PDE5A | | 1T9S | $Zn^{2+}$ | 6 | 2 | 4 | - | T6 Octahedral | $Mg^{2+}$ | |
| Human PDE7A | | 1ZKL | $Zn^{2+}$ | 6 | 2 | 4 | - | T6 Octahedral | $Mg^{2+}$ | |
| Human PDE8A | | 3ECN | $Zn^{2+}$ | 4 | - | 4 | - | T4 Tetrahedral | - | |
| Human PDE8A | | 3ECM | $Zn^{2+}$ | 5 | 1 | 4 | - | T5 Trigonal Bipyramidal | $Mg^{2+}$ | |
| Human PDE9A | | 2YY2 | $Zn^{2+}$ | 4 | - | 4 | - | T4 Tetrahedral | $Mg^{2+}$ | |
| Human PDE9A | | 2HD1 | $Zn^{2+}$ | 5 | 1 | 4 | - | T5 Trigonal Bipyramidal | $Mg^{2+}$ | |
| Human PDE9A | | 3DYN | $Zn^{2+}$ | 6 | 2 | 4 | - | T6 Octahedral | $Mg^{2+}$ | |
| Human PDE9A | | 3DYL | $Mn^{2+}$ | 6 | 1 | 4 | 1 | T6 Octahedral | $Mg^{2+}$ | |
| Human PDE9A | | 3DY8 | $Mn^{2+}$ | 6 | 2 | 4 | - | T6 Octahedral | $Mg^{2+}$ | |
| Human PDE10 | | 2OUP | $Zn^{2+}$ | 5 | 1 | 4 | - | T5 Trigonal Bipyramidal | $Mg^{2+}$ | |
| Human PDE10 | | 2OUQ | $Zn^{2+}$ | 6 | - | 4 | 2 | T6 Octahedral | $Mg^{2+}$ | 2OUN |
| Human PDE10 | | 2WEY | $Zn^{2+}$ | 6 | 2 | 4 | - | T6 Octahedral | $Mg^{2+}$ | 2OUY, 2OUV |

# Chapter 7. References

Aberg, A., Fernandez-Vazquez. J., Cabrer-Panes, J.D., Sanchez, A. & Balsalobre, C. (2009): Similar and divergent effects of ppGpp and DksA deficiencies on transcription in *Escherichia coli*. *J Bacteriol* **191**, 3226-3236.

Adams, J.L., & McLean. R.J.C. (1999): Impact of *rpoS* deletion on *Escherichia coli* biofilms. *Appl Environ Microbiol* **65**, 4285-4287.

Adams, P.D., Afonine, P.V., Bunkóczi, G., Chen, V.B., Davis, I.W., Echols, N., Headd, J.J., Hung, L.W., Kapral, G.J., Grosse-Kunstleve, R.W., McCoy, A.J., Moriarty, N.W., Oeffner, R., Read, R.J., Richardson, D.C., Richardson, J.S., Terwilliger, T.C. & Zwart, P.H. (2010): PHENIX: a comprehensive Python-based system for macromolecular structure solution. *Acta Cryst* **D66**, 213-221.

Agalarov. S.C., Prasad, G.S. & Funke, P.M., Stout C.D. & Williamson, J.R. (2000): Structure of the S15, S6, S18-rRNA complex: assembly of the 30S ribosome central domain. *Science* **288**, 107 -112.

Agirrezabala, X., Fernández, I.S., Kelley, A.C., Cartón, D.G., Ramakrishnan, V. & Valle, M. (2013): The ribosome triggers the stringent response by RelA via a highly distorted tRNA. *EMBO Rep* **14**, 811-816

Aizenman, E., Engelberg-Kulka, H. & Glaser G. (1996): An *Escherichia coli* chromosomal "addiction module" regulated by guanosine 3', 5'-bispyrophosphate: a model for programmed bacterial cell death. *Proc Natl Acad Sci USA* **93**, 6059-6063.

Alberts, I.L., Nadassy, K. & Wodak, S.J. (1998): Analysis of zinc binding sites in protein crystal structures. *Prot Sci* **7**, 1700-1716.

Arai, K., Arai, N. & Kawakita, M. (1972): Interaction of guanosine 5'-diphosphate, 2'-(or 3'-) diphosphate (ppGpp) with elongation factors from *E. coli*. *Biochem Biophys Res Commun* **48**, 191-196.

Aravind, L., & Koonin, E.V. (1998): The HD domain defines a new superfamily of metal-dependent phosphohydrolases. *Trends Biochem Sci* **23**, 469-472.

Arndt, J.W., Gong, W., Zhong., X., Showalter, A.K., Liu, J., Dunlap, C.A., Lin, Z., Paxson, C., Tsai M-D. & Chan, M.K. (2001): Insight into the catalytic mechanism of DNA polymerase β: Structures of intermediate complexes. *Biochemistry* **40**, 5368-5375.

Artsimovitch, I., Patlan, V., Sekine, S. & Vassylyeva, M. (2004): Structural basis for transcription regulation by alarmone ppGpp. *Cell* **117**, 299-310.

Atkinson, G.C., Tenson, T. & Hauryliuk, V. (2011): The RelA/SpoT homolog (RSH) superfamily: distribution and functional evolution of ppGpp synthetases and hydrolases across the tree of life. *PLoS One* **6**, e23479.

Avarbock, D., Avarbock, A. & Rubin, H. (2000): Differential regulation of opposing Rel$_{Mtb}$ activities by the aminoacylation state of a tRNA•ribosome•mRNA•Rel$_{Mtb}$ complex. *Biochemistry* **39**, 11640-11648.

Avarbock, A., Avarbock, D., Teh, J. & Buckstein M. (2005): Functional regulation of the opposing (p) ppGpp synthetase/hydrolase activities of Rel$_{Mtb}$ from *Mycobacterium tuberculosis*. *Biochemistry* **44**, 9913-9923.

Balaban, N.Q., Merrin, J., Chait, R., Kowalik, L. & Leibler, S. (2004): Bacterial persistence as a phenotypic switch. *Science* **305**, 1622-1625.

Balzer, G.J. & McLean, R.J. (2002): The stringent response genes *relA* and *spoT* are important for *Escherichia coli* biofilms under slow-growth conditions. *Can J Microbiol* **48**, 675-680.

Battesti, A. & Bouveret, E. (2006): Acyl carrier protein/SpoT interaction, the switch linking SpoT-dependent stress response to fatty acid metabolism. *Mol Microbiol* **62**, 1048-1063.

Battesti, A. & Bouveret E. (2009): Bacteria possessing two RelA/SpoT-like proteins have evolved a specific stringent response involving the acyl carrier protein-SpoT interaction. *J Bacteriol* **191**, 616-624.

Baysse, C., Cullinane, M., Denervaud, V., Burrowes, E., Dow, J.M., Morrissey, J.P., Tam, L., Trevors, J.T. & O'Gara, F. (2005): Modulation of quorum sensing in *Pseudomonas aeruginosa* through alteration of membrane properties. *Microbiology* **151,** 2529-2542.

Beard, W.A. & Wilson, S.H. (2006): Structure and mechanism of DNA polymerase β. *Chem Rev* **106**, 361- 382.

Blaby-Haas, C.E., Furman, R., Rodionov, D.A., Artsimovitch, I. & de Crécy-Lagard, V. (2011): Role of a Zn-independent DksA in Zn homeostasis and stringent response. *Mol Microbiol* **79**, 700-715.

Boehm, A., Steiner, S., Zaehringer, F., Casanova, A., Hamburger, F., Ritz, D., Keck, W., Ackermann, M., Schirmer, T. & Jenal, U. (2009): Second messenger signalling governs *Escherichia coli* biofilm induction upon ribosomal stress. *Mol Microbiol* **72**, 1500-1516.

Branda, S. S., Vik, S., Friedman, L. & Kolter, R. (2005): Biofilms: the matrix revisited. *Trends Microbiol* **13**, 20-26.

Breeden, L. & Yarus, M. (1982): Amber suppression relaxes stringent control by elongating stringent factor. *Mol Gen Genet* **187**, 254-264.

Buglino, J., Shen, V., Hakimian, P. & Lima C. (2002): Structural and biochemical analysis of the Obg GTP binding protein. *Structure* **10**, 1581-1592.

Cashel, M. & Gallant, J. (1969): Two compounds implicated in the function of the RC gene of *Escherichia coli*. *Nature* **221**, 838-841.

Cashel, M., Gentry, D.R., Hernandez, V.H. & Vinella D (1996): The stringent response. In *Escherichia coli* and *Salmonella*: *cellular and molecular biology*. Vol. 2. Neidhardt, F.C., Curtiss III, R., Ingraham, J.L., Lin, E.C.C., Low, K.B., Magasanik, B., Reznikoff, W.S., Riley, M., Schaechter, M., & Umbarger, H.E. ASM Press. Washington, D.C. pp. 1410-1438.

Chatterji, D. & Ojha, A. (2001): Revisiting the stringent response, ppGpp and starvation signaling. *Curr Opin Microbiol* **4**, 160-165.

Chatterji, D., Ogawa, Y., Shimada, T. & Ishihama, A. (2007): The role of the omega subunit of RNA polymerase in expression of the *relA* gene in *Escherichia coli*. *FEMS Microbiol Lett* **267**, 51-55.

Chipman, D. & Shaanan, B. (2001): The ACT domain family. *Curr Opin Struct Biol* **11**, 694-700.

Cho, Y., Sharma, V. & Sacchettini, J.C. (2003): Crystal Structure of ATP phospho-ribosyltransferase from *Mycobacterium tuberculosis*. *J Biol Chem* **278**, 8333-8339.

Chowdhury, M.N., Kambal, A.M., al-Eissa, Y,A., Khaliq, M.R., al-Ayed, I.H., & al-Sanie, A.M. (1997): Non-group A streptococci: are they pathogens in the throat? *J R Soc Health* **117**, 160-163.

Christianson, D.W. & Cox, J.D. (1999): Catalysis by metal-activated hydroxide in zinc and manganese metalloenzymes. *Annu Rev Biochem* **68**, 33-57.

Christensen, S.K., Mikkelsen, M., Pedersen, K. & Gerdes, K. (2001): RelE, a global inhibitor of translation, is activated during nutritional stress. *Proc Natl Acad Sci USA* **98**, 14328-14333.

Christensen, S.K. & Gerdes, K. (2003): RelE toxins from bacteria and Archaea cleave mRNAs on translating ribosomes, which are rescued by tmRNA. *Mol Microbiol* **48**,1389-1400.

Dalebroux, Z.D., Svensson, S.L., Gaynor, E.C. & Swanson, M.S. (2010): ppGpp conjures bacterial virulence. *Microbiol Mol Biol Rev* **74**, 177-191.

Das, B., Pal, R. R., Bag, S. & Bhadra, R. K. (2009): Stringent response in *Vibrio cholerae*: genetic analysis of *spoT* gene function and identification of a novel (p)ppGpp synthetase gene. *Mol Microbiol* **72**, 380-398.

Dennis, P.P., Ehrenberg, M. & Bremer, H. (2004): Control of rRNA synthesis in *Escherichia coli*: a systems biology approach. *Microbiol Mol Biol Rev* **68**. 639-668.

Dey, S., Hu, Z., Xu, X.L., Sacchettini, J.C. & Grant, G.A. (2007): The effect of hinge mutations on effector binding and domain rotation in *Escherichia coli* D-3-phosphoglycerate dehydrogenase. *J Biol Chem* **282**, 18418-18426.

Dieye, Y., Ameiss, K., Mellata, M. & Curtiss III, R. (2009): The Salmonella Pathogenicity Island (SPI) 1 contributes more than SPI2 to the colonization of the chicken by *Salmonella enterica serovar typhimurium*. *BMC Microbiol* **9**, 3.

Dix, D.B. & Thompson, R.C. (1986): Elongation factor Tu.guanosine 3'-diphosphate 5'-diphosphate complex increases the fidelity of proofreading in protein biosynthesis: mechanism for reducing translational errors introduced by amino acid starvation. *Proc Natl Acad Sci USA* **83**, 2027-2058.

Emsley, P. & Cowtan, K. (2004): Coot: model-building tools for molecular graphics. *Acta Cryst* **D60**, 2126-2132.

Engelberg-Kulka, H., Amitai, S., Kolodkin-Gal, I. & Hazan, R. (2006): Bacterial programmed cell death and multicellular behavior in bacteria. *PLoS Genet* **2**, e135.

Ettema, T. J. G., Brinkman, A. B., Tani, T. H., Rafferty, J. B., and van der Oost, J. (2002): A novel ligand-binding domain involved in regulation of amino acid metabolism in prokaryotes. *J Biol Chem* **277**. 37464 –37468.

Evans, P. (2006): Scaling and assessment of data quality. *Acta Cryst* **D62**, 72-82.

Finney L.A. & O'Halloran T.V. (2003): Transition metal speciation in the cell: insights from the chemistry of metal ion receptors. *Science* **300**, 931-936.

Fischetti, V.A. (1989): Streptococcal M protein: molecular design and biological behavior. *Clin Microbiol Rev* **2**, 285-314.

Friesen, J.D., Fiil, N.P., Parker, J.M., & Haseltine, W.A. (1974): A new relaxed mutant of *Escherichia coli* with an altered 50S ribosomal subunit. *Proc Natl Acad Sci USA* **71**, 3465-3469.

Gale, E.F. & Epps, H.M. (1942): The effect of the pH of the medium during growth on the enzymic activities of bacteria (*Escherichia coli* and *Micrococcus lysodeikticus*) and the biological significance of the changes produced. *Biochem J* **36**, 600-618.

Gallagher, D.T., Gilliland, G.L., Xiao, G., Zondlo, J., Fisher, K.E., Chinchilla, D. & Eisenstein, E. (1998): Structure and control of pyridoxal phosphate dependent allosteric threonine deaminase. *Structure* **6**. 465-475.

Gasteiger, E., Hoogland, C., Gattiker, A., Duvaud, S., Wilkins, M.R., Appel, R.D. & Bairoch, A. (2005); Protein identification and analysis tools on the ExPASy Server; (In) John M. Walker (ed): The Proteomics Protocols Handbook, Humana Press. 571-607.

Gentry, D.R. & Cashel, M. (1996): Mutational analysis of the *Escherichia coli* spoT gene identifies distinct but overlapping regions involved in ppGpp synthesis and degradation. *Mol Microbiol* **19**, 1373-1384.

Gerdes, K. (2000): Toxin–antitoxin modules may regulate synthesis of macromolecules during nutritional stress. *J Bacteriol* **182**, 561–572.

Gerdes, K., Christensen, S. K. & Løbner-Olesen A. (2005): Prokaryotic toxin-antitoxin stress response loci. *Nat Rev Microbiol* **3**, 371-382.

Geyer, A. & Schmidt, K.H. Genetic organisation of the M protein region in human isolates of group C and G streptococci: two types of multigene regulator-like (mgrC) regions. *Mol Gen Genet* **262**, 965-976.

Ginther, C.L. & Ingraham, J.L. (1974): Nucleoside diphosphokinase of *Salmonella typhimurium*. *J Biol Chem* **249**, 3406-3411.

Gong, L., Takayama, K. & Kjelleberg, S. (2002): Role of spoT-dependent ppGpp accumulation in the survival of light-exposed starved bacteria. *Microbiology* **148**, 559-570.

Gorgel, M. (2009): *In vitro* Analyse des Stringenz Faktors Rel aus *Thermus thermophilus* und anderen Bakterien. (Bachelor Thesis)

Gotfredsen, M. & Gerdes, K. (1998): The *Escherichia coli relBE* genes belong to a new toxin-antitoxin gene family. *Mol Microbiol* **29**, 1065-1076.

Grant, G.A. (2006): The ACT domain: A small molecule binding domain and its role as a common regulatory element. *J Biol Chem* **281**, 33825-33829.

Gropp, M., Strausz, Y., Gross, M. & Glaser, G. (2001): Regulation of *Escherichia coli* RelA requires oligomerization of the C-terminal domain. *J Bacteriol* **183**, 570-579.

Hansen, J.L., Moore, P.B. & Steitz, T.A. (2003): Structures of five antibiotics bound at the peptidyl transferase center of the large ribosomal subunit. *J Mol Biol* **330**, 1061-1075.

Haraga, A., Ohlson, M. B., & Miller, S. I. (2008): Salmonellae interplay with host cells. *Nat Rev Microbiol* **6**, 53-66.

Harris, B.Z., Kaiser, D. & Singer, M. (1998): The guanosine nucleotide (p)ppGpp initiates development and A-factor production in *Myxococcus xanthus*. *Genes Dev* **12**, 1022-1035.

Haseltine, W.A. & Block, R. (1973): Synthesis of guanosine tetra- and penta phosphate requires the presence of a codon-specific, uncharged transfer ribonucleic acid in the acceptor site of ribosomes. *Proc Natl Acad Sci USA* **70,** 1564-1568.

Heinemeyer, E. A., & Richter, D. (1978): Mechanism of the in vitro breakdown of guanosine 5'-diphosphate 3'-diphosphate in *Escherichia coli*. *Proc Natl Acad Sci USA* **75**, 4180-4183.

Held, W.A., Ballou, B., Mizushima, S. & Nomura, M. (1974): Assembly mapping of 30S ribosomal proteins from *Escherichia coli*. Further studies. *J Biol Chem* **249**, 3103-3111.

Hernandez, V.J. & Bremer, H. (1991): *Escherichia coli* ppGpp synthetase II activity requires *spoT*. *J Biol Chem* **266**, 5991-5999.

Hogg, T., Mechold, U., Malke, H., Cashel, M. & Hilgenfeld, R. (2004): Conformational antagonism between opposing active sites in a bifunctional RelA/SpoT homolog modulates (p)ppGpp metabolism during the stringent response. *Cell* **117**, 57-68.

Holm, L. & Rosenström, P. (2010): Dali server: conservation mapping in 3D. *Nucleic Acids Res* **38**, W545-W549.

Inaoka, T. & Ochi, K. (2002): RelA protein is involved in induction of genetic competence in certain *Bacillus subtilis* strains by moderating the level of intracellular GTP. *J Bacteriol* **184**, 3923-3930.

Itoh, Y., Rice, J., Goller, C., Pannuri, A., Taylor J., Meisner, J., Beveridge, T.J., Preston III, J.F. & Romeo, T. (2008): Roles of *pgaABCD* genes in synthesis, modification, and export of the *Escherichia coli* biofilm adhesin poly-β-1,6-N-acetyl-D-glucosamine. *J Bacteriol* **190**, 3670-3680.

Jain, V., Saleem-Batcha, R., China, A. & Chatterji, D. (2006a): Molecular dissection of the mycobacterial stringent response protein Rel. *Protein Sci* **15**, 1449-1464.

Jain, V., Kumar, M. & Chatterji, D. (2006b): ppGpp: stringent response and survival. *J Microbiol* **44**, 1-10.

Jain, V., Saleem-Batcha, R. & Chatterji, D. (2007): Synthesis and hydrolysis of pppGpp in mycobacteria: a ligand mediated conformational switch in Rel. *Biophys Chem* **127**, 41-50.

Jayaraman, R. (2008a): Bacterial persistence: some new insights into an old phenomenon. *J Biosci* **33**, 795-805.

Jayaraman, A. & Wood, T.K. (2008b): Bacterial quorum sensing: signals, circuits, and implications for biofilms and disease. *Annu Rev Biomed Eng* **10**, 145-167.

Jenvert, R-M. & Schiavone, L. (2007): The flexible N-terminal domain of ribosomal protein L11 from *Escherichia coli* is necessary for the activation of stringent factor. *J Mol Biol* **365**, 764-836.

Jenner, L.B., Demeshkina, N., Yusupova, G. & Yusupov, M. (2010): Structural aspects of messenger RNA reading frame maintenance by the ribosome. *Nat Struct Mol Biol* **17**, 555-560.

Jiang, M., Sullivan, S. M., Wout, P. K. & Maddock, J.R. (2007): G-protein control of the ribosome-associated stress response protein SpoT. *J Bacteriol*, **189**, 6140-6147.

Jishage, M., Kvint, K., Shingler, V. & Nyström, T (2002): Regulation of σ factor competition by the alarmone ppGpp. *Genes Dev* **16**, 1260-1270.

Justesen, J., Lund, T., Skou Pedersen, F. & Kjeldgaard, N.O. (1986): The physiology of stringent factor (ATP:GTP 3'-diphosphotransferase) in *Escherichia coli*. *Biochimie* **68**, 715-722.

Kabsch, W. (1976): A solution for the best rotation to relate two sets of vectors. *Acta Cryst* **A32**, 922-923.

Kade, B., Dabbs, E.R. & Wittmann-Liebold, B. (1980): Protein-chemical study on *Escherichia coli* mutants with altered ribosomal proteins S6 and S7. *FEBS Lett* **121**, 313-316.

Kamada, K., Hanaoka, F. & Burley, S.K. (2003): Crystal structure of the MazE/MazF complex: molecular bases of antidote-toxin recognition. *Mol Cell* **11**, 875-884.

Kang, W,K., Icho, T., Isono, S., Kitakawa, M. & Isono, K. (1989): Characterization of the gene rimK responsible for the addition of glutamic acid residues to the C-terminus of ribosomal protein S6 in *Escherichia coli* K12. *Mol Gen Genet* **217,** 281-288.

Kanjee, U., Gutsche, I., Alexopoulos, E., Zhao, B., El Bakkouri, M., Thibault, G., Liu, K., Ramachandran, S., Snider, J., Pai, E.F. & Houry, W.A. (2011): Linkage between the bacterial acid stress and stringent responses: the structure of the inducible lysine decarboxylase. *EMBO J* **30**, 931-944.

Kaplun, A., Vyazmensky, M., Zherdev, Y., Belenky, I., Slutzker, A., Mendel, S., Barak, Z., Chipman, D.M., Shaanan, B. (2006): Structure of the regulatory subunit of acetohydroxyacid synthase isozyme III from *Escherichia coli*. *J Mol Biol* **357**, 951-963.

Kari, C., Török, I. & Travers, A. (1977): ppGpp cycle in *Escherichia coli*. *Mol Gen Genet* **150**, 249-255.

Karzai, A.W., Roche, E.D., & Sauer, R.T. (2000): The SsrA-SmpB system for protein tagging, directed degradation and ribosome rescue. *Nat Struct Biol* **7**, 449-455.

Keasling, J.D., Bertsch, L., & Kornberg, A. (1993): Guanosine pentaphosphate phosphohydrolase of *Escherichia coli* is a long-chain exopolyphosphatase, *Proc Natl Acad Sci USA* **90**, 7029-7033.

Khorana, H., Fernandes, J. & Kornberg, A. (1958): Pyrophosphorylation of ribose 5-phosphate in the enzymatic synthesis of 5-phosphorylribose 1-pyrophosphate. *J Biol Chem* **230**, 941-949.

Kim, H.Y., Schlictman, D., Shankar, S., Xie, Z., Chakrabarty, A.M. & Kornberg, A. (1998): Alginate, inorganic polyphosphate, GTP and ppGpp synthesis co-regulated in *Pseudomonas aeruginosa*: implications for stationary phase survival and synthesis of RNA/DNA precursors. *Mol Microbiol* **27**, 717-725.

Kino, K., Arai, T. & Arimura,Y. (2011): Poly-alpha-glutamic acid synthesis using a novel catalytic activity of RimK from *Escherichia coli* K-12. *Appl Environ Microbiol* **77**, 2019-2025.

Kleywegt, G.J. & Jones, T.A. (1998): Databases in protein crystallography. *Acta Cryst* **D54,** 1119-1131.

Klinkenberg, L.G., Lee, J.H., Bishai, W.R. & Karakousis, P.C. (2010): The stringent response is required for full virulence of *Mycobacterium tuberculosis* in guinea pigs. *J Infect Dis* **202**, 1397-1404.

Kobe, B, Jennings, I.G., House, C.M., Michell, B.J., Goodwill, K.E., Santarsiero, B.D., Stevens, R.C., Cotton, R.G., & Kemp, B.E. (1999): Structural basis of autoregulation of phenylalanine hydroxylase. *Nat Struct Biol* **6**, 442–448.

Korch, S., Henderson, T. & Hill, T. (2003): Characterization of the *hipA7* allele of *Escherichia coli* and evidence that high persistence is governed by (p)ppGpp synthesis. *Mol Microbiol* **50**, 1199–1213.

Kristensen, O., Laurberg, M. & Gajhede, M. (2002): Crystallization of a stringent response factor from *Aquifex aeolicus*. *Acta Cryst* **D58**, 1198-1200.

Kristensen, O., Laurberg, M., Liljas, A., Kastrup, J.S. & Gajhede, M. (2004): Structural characterization of the stringent response related exopoly-phosphatase /guanosine pentaphosphate phosphohydrolase protein family. *Biochemistry* **43**, 8894-8900.

Kristensen, O., Ross, B. & Gajhede, M. (2008): Structure of the PPX/GPPA phosphatase from *Aquifex aeolicus* in complex with the alarmone ppGpp. *J Mol Biol* **375**, 1469-1476.

Kuroda, A., Murphy, H., Cashel, M. & Kornberg, A. (1997): Guanosine tetra- and pentaphosphate promote accumulation of inorganic polyphosphate in *Escherichia coli*. *J Biol Chem* **272**, 21240–21243.

Laskowski, R.A., MacArthur, M.W., Moss, D.S. & Thornton, J.M. (1993): PROCHECK: a program to check the stereochemical quality of protein structures. *J Appl Cryst* **26**, 283-291.

Lemos, J.A., Brown Jr, T.A. & Burne, R.A. (2004): Effects of RelA on key virulence properties of planktonic and biofilm populations of *Streptococcus mutans*. *Infect Immun* **72,** 1431-1440.

Lemos, J.A., Nascimento, M.M., Lin, V.K., Abranches, J. & Burne, R.A. (2008): Global regulation by (p)ppGpp and CodY in *Streptococcus mutans*. *J Bacteriol* **190,** 5291-5299.

Leslie, A.G.W., (1992): Recent changes to the MOSFLM package for processing film and image plate data. *Jnt CCP4/ESF-EACBM Newsl Protein Crystallogr* **26**, 27-33.

Lesley, J.A. & Shapiro, L. (2008): SpoT regulates DnaA stability and initiation of DNA replication in carbon-starved *Caulobacter crescentus*. *J Bacteriol* **190**, 6867-6880.

Levin, A.D., Pribytkov, V.A., Rukin, E.M. & Seregina, I.F. (2001): Atomic-absorption spectrometry in the elemental analysis of biological materials. *Meas Tech* **44**, 660-662.

Levine, A., Vannier, F., Dehbi, M., Henckes, G. & Séror S.J. (1991): The stringent response blocks DNA replication outside the ori region in *Bacillus subtilis* and at the origin in *Escherichia coli*. *J Mol Biol* **219**, 605-613.

Liberles, J.S., Thorolfsson, M. & Martinez, A. (2005): Allosteric mechanisms in ACT domain containing enzymes involved in amino acid metabolism. *Amino Acids* **28**, 1-12.

Lindahl, M., Svensson, L.A., Lilijas, A., Sedelnikova, S.E., Eliseikina, I.A., Fomenkova, N.P., Nevskaya, N., Nikonov, S.V., Garber, M.B., Muranova, T.A., Rykonova, A.I. & Amons, R. (1994): Crystal structure of the ribosomal protein S6 from *Thermus thermophilus*. *EMBO J* **13**, 1249-1254.

Maciag, M., Kochanowska, M., Lyzeń, R., Wegrzyn, G. & Szalewska-Pałasz, A. (2010): ppGpp inhibits the activity of *Escherichia coli* DnaG primase. *Plasmid* **63**, 61-67.

Magnusson, L., Farewell, A. & Nyström, T. (2005): ppGpp: a global regulator in *Escherichia coli*. *Trends Microbiol* **13**, 236-242.

Mas-Droux, C., Curien, G., Robert-Genthon, M., Laurencin, M, Ferrer J-L. & Dumas, R. (2006): A novel organization of ACT domains in allosteric enzymes revealed by the crystal structure of *Arabidopsis* aspartate kinase. *Plant Cell* **18**, 1681-1692.

Mathew, R. & Chatterji, D. (2006): The evolving story of the omega subunit of bacterial RNA polymerase. *Trends Microbiol* **14**, 450-455.

Matthes, N., Mesters, J.R., Coutard, B., Canard, B., Snijder, E.J., Moll, R. & Hilgenfeld, R. (2006): The non-structural protein Nsp10 of mouse hepatitis virus binds zinc ions and nucleic acids. *FEBS Letters* **580,** 4143-4149.

McCall, K.A., Huang, C.C. & Fierke, C.A. (2000): Function and mechanism of zinc metalloenzymes. *J Nutr* **130**, 1437S-1446S.

McCoy, A.J., Grosse-Kunstleve, R.W., Adams. P.D., Winn, M.D., Storoni, L.C. & Read, R.J. (2007): Phaser crystallographic software. *J Appl Cryst* **40**, 658-674.

McDonald, M., Towers, R.J., Andrews, R.M., Carapetis, J.R. & Currie, B.J. (2007): Epidemiology of *Streptococcus dysgalactiae subsp. equisimilis* in Tropical Communities, Northern Australia. *Emerg Infect Dis* **13**, 1694-1700.

Mechold, U., Cashel, M., Steiner, K., Gentry., D & Malke., H. (1996): Functional analysis of a *relA/spoT* gene homolog from *Streptococcus equisimilis*. *J Bacteriol* **178**, 1401-1411.

Mechold, U., Murphy, H., Brown, L. & Cashel, M. (2002): Intramolecular regulation of the opposing (p)ppGpp catalytic activities of Rel$_{Seq}$, the Rel/Spo enzyme from *Streptococcus equisimilis*. *J Bacteriol* **184**, 2878–2888.

Mellies, J.L., Barron, A.M. & Carmona, A.M. (2007): Enteropathogenic and enterohemorrhagic *Escherichia coli* virulence gene regulation. *Infect Immun* **75**, 4199–4210.

Moynié, L., Giraud, M.-F., Georgescauld, F., Lascu, I., Dautant. & Mellies, J.L.A. (2007): The structure of the *Escherichia coli* nucleoside diphosphate kinase reveals a new quaternary architecture for this enzyme family. **Proteins** *67*: 755-765.

Milon, P., Tischenko, E., Tomsic, J., Caserta, E., Folkers, G., La Teana, A., Rodnina, M.V., Pon, C.L., Boelens, R. & Gualerzi, C.O. (2006): The nucleotide-binding site of bacterial translation initiation factor 2 (IF2) as a metabolic sensor. *Proc Natl Acad Sci USA* **103**, 13962-13967.

Mirouze, N., Prepiak, P. & Dubnau, D. (2011): Fluctuations in spo0A transcription control rare developmental transitions in *Bacillus subtilis*. *PLoS Gene*t **7**, e1002048.

Mitkevich, V.A., Ermakov, A., Kulikova, A.A., Tankov, S., Shyp, V., Soosaar, A., Tenson, T., Makarov, A.A., Ehrenberg, M. & Hauryliuk, V. (2010): Thermodynamic characterization of ppGpp binding to EF-G or IF2 and of initiator tRNA binding to free IF2 in the presence of GDP, GTP, or ppGpp. *J Mol Biol* **402**, 838-846.

Mittenhuber G. (2001): Comparative genomics and evolution of genes encoding bacterial (p)ppGpp synthetases/hydrolases (the Rel, RelA and SpoT proteins). *J Mol Microbiol Biotechnol* **3**, 585-600.

Muñoz-Gómez, A.J., Santos-Sierra, S., Berzal-herranz, A., Lemonnier, M. & Díaz-Orejas, R. (2004): Insights into the specificity of RNA cleavage by the *Escherichia coli* MazF toxin. *FEBS Letters* **567**, 316-320.

Murshudov G.N., Vagin, A.A. & Dodson, E.J. (1997): Refinement of macromolecular structures by the maximum-likelihood method. *Acta Cryst* **D53**, 240-255.

Nakanishi, N., Abe, H., Ogura, Y., Hayashi, T., Tashiro, K., Kuhara, S., Sugimoto, N. & Tobe, T. (2006): ppGpp with DksA controls gene expression in the locus of enterocyte effacement (LEE) pathogenicity island of enterohaemorrhagic *Escherichia coli* through activation of two virulence regulatory genes. *Mol Microbiol* **61**,194–205.

Nataro, J. P. & J. B. Kaper, J.B. (1998): Diarrheagenic *Escherichia coli*. *Clin Microbiol Rev* **11**, 142–201.

Neubauer, C., Gao, Y.G., Andersen, K.R., Dunham, C.M., Kelley, A.C., Hentschel, J., Gerdes, K., Ramakrishnan, V. & Brodersen, D.E. (2009): The structural basis for mRNA recognition and cleavage by the ribosome-dependent endonuclease RelE. *Cell* **139**, 1084-1095.

Nyström, T. (1998): To be or not to be: the ultimate decision of the growth-arrested bacterial cell. *FEMS Microbiol Rev* **21**, 283-290.

Ochi, K., Kandala, J.C. & Freese, E. (1981): Initiation of *Bacillus subtilis* sporulation by the stringent response to partial amino acid deprivation. *J Biol Chem* **256**, 6866-6875.

Ochi, K., Kandala, J.C. & Freese, E. (1982): Evidence that *Bacillus subtilis* sporulation induced by the stringent response is caused by the decrease in GTP or GDP. *J Bacteriol* **151**, 1062-1065.

Overgaard, M., Borch, J., Gerdes, K., (2009): RelB and RelE of *Escherichia coli* form a tight complex that represses transcription via the ribbon-helix-helix motif in RelB. *J Mol Biol* **394**, 183-196.

Painter, J. & Merritt, E.A. (2006): Optimal description of a protein structure in terms of multiple groups undergoing TLS motion. *Acta Cryst* **D62**, 439-450.

Paul, B.J., Barker, M.M., Ross, W., Schneider, D.A., Webb, C., Foster, J.W. & Gourse, R.L. (2004): DksA: a critical component of the transcription initiation machinery that potentiates the regulation of rRNA promoters by ppGpp and the initiating NTP. *Cell* **118,** 311-322.

Paul, B.J., Berkmen, M.B. & Gourse, R.L. (2005): DksA potentiates direct activation of amino acid promoters by ppGpp. *Proc Natl Acad Sci USA* **102,** 7823-7828.

Pedersen, K., Christensen, S. & Gerdes, K. (2002): Rapid induction and reversal of a bacteriostatic condition by controlled expression of toxins and antitoxins. *Mol Microbiol* **45**, 501-510.

Pedersen, F.S. & Kjeldgaard, N.O. (1977): Analysis of the *relA* gene product of *Escherichia coli*. *Eur J Biochem* **76**, 91-97.

Perederina, A., Svetlov, V., Vassylyeva, M., Tahirov, T.H., Yokoyama, S., Artsimovitch, I. & Vassylyev, D.G. (2004): Regulation through the secondary channel - structural framework for ppGpp-DksA synergism during transcription. *Cell* **118**, 297-309.

Pettersen, E. F., Goddard, T. D., Huang, C. C., Couch, G. S., Greenblatt, D. M., Meng, E. C., & Ferrin, T. E. (2004): UCSF Chimera -- a visualization system for exploratory research and analysis. *J Comput Chem* **13**, 1605-1612.

Pingoud, A., Gast, F.U., Block, W. & Peters, F. (1983): The elongation factor Tu from *Escherichia coli*, aminoacyl-tRNA, and guanosine tetraphosphate form a ternary complex which is bound by programmed ribosomes. *J Biol Chem* **258**, 14200-14205.

Potier, N., Lamour, V., Poterszman, A., Thierry, J.C., Moras, D. & Van Dorsselaer, A. (2000): Characterization of crystal content by ESI-MS and MALDI-MS. *Acta Cryst* **D56**, 1583-1590.

Potrykus, K. & Cashel, M. (2008): (p)ppGpp: still magical? *Annu Rev Microbiol* **62**, 35-51.

Prilusky, J., Felder, C.E., Zeev-Ben-Mordehai, T., Rydberg, E.H., Man, O., Beckmann, J.S., Silman, I. & Sussman, J.L. (2005): FoldIndex[©]: a simple tool to predict whether a given protein sequence is intrinsically unfolded. *Bioinformatics* **21**, 3435-3438.

Rantala, S., Vähäkuopus, S., Vuopio-Varkila, J., Vuento, R. & Syrjänen, J. (2010): *Streptococcus dysgalactiae subsp. equisimilis* Bacteremia, Finland, 1995–2004. *Emerg Infect Dis* **16**, 843-846.

Ratnayake-Lecamwasam, M., Serror, P., Wong, K.W. & Sonenshein, A.L. (2001): *Bacillus subtilis* CodY represses early-stationary-phase genes by sensing GTP levels. *Genes Dev* **15**, 1093-1103.

Raskin, D.M., Judson, N. & Mekalanos, J.J. (2007): Regulation of the stringent response is the essential function of the conserved bacterial G protein CgtA in *Vibrio cholerae*. *Proc Natl Acad Sci USA* **104**, 4636-4641.

Raue, A.H. & Cashel, M. (1975): Regulation of RNA synthesis in *Escherichia coli*. III. Degradation of guanosine 5'-diphosphate 3'-diphosphate in cold-shocked cells. *Biochim Biophys Acta* **383,** 290-304.

Reddy, M.C., Gokulan, K., Jacobs, W.R., Ioerger, T.R. & Sacchettini, J.C. (2008): Crystal structure of *Mycobacterium tuberculosis* LrpA, a leucine-responsive global regulator associated with starvation response. *Prot Sci* **17**, 159-170.

Rojas, A., Ehrenberg, M., Andersson S.G. & Kurland, C.G. (1984): ppGpp inhibition of elongation factors Tu, G and Ts during polypeptide synthesis. *Mol Gen Genet* **197**, 36-45.

Rymer, R.U., Solorio, F.A., Tehranchi, A.K., Chu, C., Corn, J.E., Keck, J.L., Wang, J.D. & Berger, J.M. (2012): Binding mechanism of metal·NTP substrates and stringent-response alarmones to bacterial DnaG-type primases. *Structure* **20**, 1478-1489.

Sabo, D.L., Boeker, E.A., Byers, B., Waron, H. & Fischer, E.H. (1974): Purification and physical properties of inducible *Escherichia coli* lysine decarboxylase. *Biochemistry* **13**, 662–670.

Sajish, M., Tiwari, D., Rananaware, D., Nandicoori, V.K. & Prakash, B. (2007): A charge reversal differentiates (p)ppGpp synthesis by monofunctional and bifunctional Rel proteins. *J Biol Chem* **282**, 34977-34983.

Sankaranarayanan, R., Dock-Bregeon, A., Romby, P., Caillet. J., Springer, M., Rees, B., Ehresmann, C., Ehresmann, B., & Moras, D. (1999): The structure of threonyl-tRNA synthetase-tRNA[Thr] complex enlightens its repressor activity and reveals an essential zinc ion in the active site. *Cell* **97**, 371-381.

Schlictman, D., Kavanaugh-Black, A., Shankar, S. & Chakrabarty, A.M. (1994): Energy metabolism and alginate biosynthesis in *Pseudomonas aeruginosa*: role of the tricarboxylic acid cycle. *J Bacteriol* **176**, 6023-6029.

Schluenzen, F., Tocilj, A., Zarivach, R., Harms, J., Gluehmann, M., Janell, D., Bashan, A., Bartels, H., Agmon, I., Franceschi, F. & Yonath, A. (2000): Structure of functionally activated small ribosomal subunit at 3.3 angstroms resolution. *Cell* **102**, 615-623.

Schmidt, F.J., Thompson, J., Lee, K., Dijk, J. & Cundliffe, E. (1981): The binding site for ribosomal protein L11 within 23S ribosomal RNA of *Escherichia coli*. *J Biol Chem* **256**, 12301-12305.

Schuller, D.J., Grant, G.A. & Banaszak, L.J. (1995): The ACT domain family. *Nat Struct Biol* **2**, 69-76.

Schrödinger: The PyMOL Molecular Graphics System, Version 1.5.0.4 Schrödinger, LLC.

Selmer, M., Dunham, C.M., Murphy IV, F.V., Weixlbaumer, A., Petry, S., Kelley, A, C., Weir, J.R., Ramakrishnan, V. (2006): Structure of the 70S ribosome complexed with mRNA and tRNA. *Science* **313**, 1935-1942.

Spira, B., Silberstein, N. & Yagil, E. (1995): Guanosine 3',5'- bispyrophosphate (ppGpp) synthesis in cells of *Escherichia coli* starved for $P_i$. *J Bacteriol* **177**, 4053-4058.

Srivatsan, A. & Wang J.D. (2008): Control of bacterial transcription, translation and replication by (p)ppGpp. *Curr Opin Microbiol* **11**, 100-105.

Stern, S., Powers, T., Changchien, L-M. & Noller, H.F. (1988): Interaction of ribosomal proteins S5, S6, S11, S12, S18 and S21 with 16S rRNA. *J Mol Biol* **201**. 683-695.

Sträter, N., Klabunde, T., Tucker, P., Witzel, H. & Krebs, B. (1995): Crystal structure of a purple acid phosphatase containing a dinuclear Fe(III)-Zn(II) active site. *Science* **268**, 1489-1492.

Sun, D., Lee, G., Lee, J.H., Kim, H.Y., Rhee, H.W., Park, S.Y., Kim, K.J., Kim, Y., Kim, B.Y., Hong, J.I., Park, C., Choy, H.E., Kim, J.H., Jeon, Y.H. & Chung, J. (2010): A metazoan ortholog of SpoT hydrolyzes ppGpp and functions in starvation responses. *Nat Struct Mol Biol* **17**, 1188-1194.

Sy, J. (1977): *In vitro* degradation of guanosine 5'-diphosphate, 3'-diphosphate. *Proc Natl Acad Sci USA* **74**, 5529-5533.

Takagi, H., Kakuta, Y., Okada, T., Yao, M., Tanaka, I. & Kimura, M. (2005): Crystal structure of archaeal toxin-antitoxin RelE-RelB complex with implications for toxin activity and antitoxin effects. *Nat Struct Mol Biol* **12**, 327-31.

Tan, K., Li, H., Zhang, R., Gu, M., Shonda, T.C. & Joachimiak, A. (2007): Structures of open (R) and close (T) states of prephenate dehydratase (PDT)—Implication of allosteric regulation by L-phenylalanine. *J Struct Biol* **162**, 94-107.

Taylor, C.M., Beresford, M., Epton, H.A., Sigee, D.C., Shama, G., Andrew, P.W. & Roberts, I.S. (2002): *Listeria monocytogenes relA* and *hpt* mutants are impaired in surface-attached growth and virulence. *J Bacteriol* **184**, 621-628.

Terry, J. M., Piña, S.E. & Mattingly, S. J. (1992): Role of energy metabolism in conversion of nonmucoid *Pseudomonas aeruginosa* to the mucoid phenotype. *Infect Immun* **60**,1329-1335.

Thompson, J., Musters, W., Cundliffe, E. & Dahlberg, A.E. (1993): Replacement of the L11 binding region within *E. coli* 23S ribosomal RNA with its homologue from yeast: *in vivo* and *in vitro* analysis of hybrid ribosomes altered in the GTPase centre. *EMBO J* **12**, 1499–1504.

van Delden, C., Comte, R. & Bally, A. (2001): Stringent response activates quorum sensing and modulates cell density-dependent gene expression in *Pseudomonas aeruginosa*. *J Bacteriol* **183**, 5376-5384.

Verger, D., Carr, P.D., Kwok, T. & Ollis, D.L. (2007): Crystal structure of the N-terminal domain of the TyrR transcription factor responsible for gene regulation of aromatic amino acid biosynthesis and transport in *Escherichia coli* K12. *J Mol Biol* **367**, 102-112.

Viducic, D., Ono, T., Murakami, K., Susilowati, H., Kayama, S., Hirota, K. & Miyake Y. (2006): Functional analysis of spoT, relA and dksA genes on quinolone tolerance in *Pseudomonas aeruginosa* under nongrowing condition. *Microbiol Immunol* **50**, 349-357.

Vinella, D., Albrecht, C., & Cashel, M. & D'Ari, R. (2005): Iron limitation induces SpoT-dependent accumulation of ppGpp in *Escherichia coli*. *Mol Microbiol* **56**, 958-970.

Voellmy, R. & Goldberg, A.L. (1980): Guanosine-5'-diphosphate-3'-diphosphate (ppGpp) and the regulation of protein breakdown in *Escherichia coli*. *J Biol Chem* **255**, 1008-1014.

Vrentas, C.E., Gaal, T., Ross, W., Ebright, R.H. & Gourse, R.L. (2005): Response of RNA polymerase to ppGpp: requirement for the omega subunit and relief of this requirement by DksA. *Genes Dev* **19**, 2378-87.

Vrentas, C.E., Gaal, T., Berkmen, M.B., Rutherford, S.T., Haugen, S.P., Vassylyev, D. G., Ross, W. & Gourse, R.L. (2008): Still looking for the magic spot: the crystallographically defined binding site for ppGpp on RNA polymerase is unlikely to be responsible for rRNA transcription. *J Mol Biol* **377**, 551-564.

Wagner, E.G., Ehrenberg, M. & Kurland, C. G. (1982): Kinetic suppression of translational errors by (p)ppGpp. *Mol Gen Genet* **185**, 269-274.

Wallace, A.C., Laskowski, R.A. & Thornton, J.M. (1995): LIGPLOT: a program to generate schematic diagrams of protein-ligand interactions. *Protein Eng* **8**, 127-134.

Walsh, C. (2003): Where will new antibiotics come from? *Nat Rev Microbiol* **1**, 65-70.

Wang, J., Sanders, G. & Grossman, A. (2007): Nutritional control of elongation of DNA replication by (p)ppGpp. *Cell* **128**, 865-875.

Washio, K., Lim, P.L., Roongsawang, N. & Morikawa, M. (2011): A truncated form of SpoT, including the ACT domain, inhibits the production of cyclic lipopeptide arthrofactin, and is associated with moderate elevation of guanosine 3',5'-bispyrophosphate level in *Pseudomonas sp.* MIS38. *Biosci Biotechnol Biochem* **75**, 1880-1888.

Wegrzyn, G. (1999): Replication of plasmids during bacterial response to amino-acid starvation. *Plasmid* **1**, 1-16.

Wegrzyn, G. & Wegrzyn, A. (2002): Stress responses and replication of plasmids in bacterial cells. *Microb Cell Fact* **1**, 2.

Weiss, M. S. & Hilgenfeld, R. (1997): On the use of the merging R-factor as a quality indicator for X-ray data. *J Appl Cryst* **30**, 203-205.

Wendrich, T. M., Blaha, G., Wilson, D.N., Marahiel, M.A. & Nierhaus, K.H. (2002): Dissection of the mechanism for the stringent factor RelA. *Mol Cell*, **10**, 779-788.

Wexselblatt, E., Katzhendler, J., Saleem-Batcha, R., Hansen, G., Hilgenfeld, R., Glaser, G. & Vidavski R.R. (2010): ppGpp analogues inhibit synthetase activity of Rel proteins from Gram-negative and Gram-positive bacteria. *Bioorg Med Chem* **18**, 4485-4497.

Wexselblatt, E., Oppenheimer-Shaanan, Y., Kaspy, I., London, N., Schueler-Furman, O., Yavin, E., Glaser, G., Katzhendler, J. & Ben-Yehuda, S. (2012): Relacin, a novel antibacterial agent targeting the stringent response. *Plos Pathogens* **8**, e1002925.

Weyer, W.J., de Boer, H.A., de Boer, J.G. & Gruber, M. (1976): The sequence of ppGpp and pppGpp in the reaction scheme for magic spot synthesis. *Biochim Biophys Acta* **442**, 123-127.

Williams, R.J.P. (1987): The biochemistry of zinc. *Chem Rev* **6**, 61-69.

Wilson, D.N. & Nierhaus, K.H. (2005): RelBE or not to be. *Nat Struct Mol Biol* **12**, 282-284.

Wolf, Y.I, Aravind, L., Grishin, N.V., & Koonin, E.V. (1999): Evolution of aminoacyl-tRNA synthetases - analysis of unique domain architectures and phylogenetic trees reveals a complex history of horizontal gene transfer events. *Genome Res* **9**, 689-710.

Wolz, C., Geiger, T. & Goerke, C. (2010): The synthesis and function of the alarmone (p)ppGpp in firmicutes. *Int J Med Microbiol* **300**, 142-147.

Xu, R.X., Hassell, A.M., Vanderwall, D., Lambert, M.H., Holmes, W.D., Luther, M.A., Rocque, W.J., Milburn, M.V., Zhao, Y., Ke, H. & Nolte, R.T. (2000): Atomic structure of PDE4: insights into phosphodiesterase mechanism and specificity. *Science* **288**, 1822–1825.

Yakunin, A.F., Proudfoot, M., Kuznetsova, E., Savchenko, A., Brown, G., Arrowsmith, C.H. & Edwards, A.M. (2004): The HD domain of the *Escherichia coli* tRNA nucleotidyltransferase has 2', 3'-cyclic phosphodiesterase, 2'-nucleotidase, and phosphatase activities. *J Biol Chem* **279**, 36819-36827.

Yang, X. & Ishiguro, E.E. (2001a): Dimerization of the RelA protein of *Escherichia coli*. *Biochem Cell Biol* **79**, 729-736.

Yang, X. & Ishiguro, E.E. (2001b): Involvement of the N terminus of ribosomal protein L11 in regulation of the RelA protein of *Escherichia coli*. *J Bacteriol* **183**, 6532-6537.

Yoshida, M., Travers, A. & Clark B, F. (1972): Inhibition of translation initiation complex formation by MS1. *FEBS Lett* **15**,163-166.

Zhang, Y., Zhang, J., Hoeflich, K.P., Ikura, M., Qing, G. & Inouye M. (2003): MazF cleaves cellular mRNAs specifically at ACA to block protein synthesis in *Escherichia coli*. *Mol Cell* **12**, 913-923.

Zyskind, J.W. & Smith, D.W. (1992): DNA replication, the bacterial cell cycle, and cell growth. *Cell* **69**, 5-8.

153